

A NEW APPROACH TO SENSITIZED LUMINESCENCE IN TRIVALENT
LANTHANIDE COORDINATION POLYMERS: FROM FUNDAMENTAL
LUMINESCENCE AND CRYSTAL ENGINEERING TOWARD SENSING
APPLICATIONS

by

Jeffrey D. Einkauf

A Dissertation Submitted to the Faculty of
The Charles E. Schmidt College of Science
In Partial Fulfillment of the Requirements for the Degree of
Doctor of Philosophy

Florida Atlantic University

Boca Raton, FL

August 2017

Copyright 2017 by Jeffrey D. Einkauf

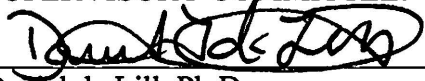
A NEW APPROACH TO SENSITIZED LUMINESCENCE IN TRIVALENT
LANTHANIDE COORDINATION POLYMERS: FROM FUNDAMENTAL
LUMINESCENCE AND CRYSTAL ENGINEERING TOWARD SENSING
APPLICATIONS

by

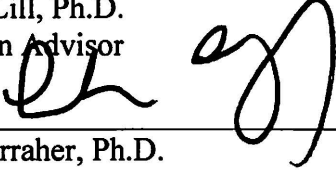
Jeffrey D. Einkauf

This dissertation was prepared under the direction of the candidate's dissertation advisor, Dr. Daniel de Lill, Department of Chemistry and Biochemistry, and has been approved by the members of his supervisory committee. It was submitted to the faculty of the Charles E. Schmidt College of Science and was accepted in partial fulfillment of the requirements for the degree of Doctor of Philosophy.

SUPERVISORY COMMITTEE:



Daniel de Lill, Ph.D.
Dissertation Advisor



Charles Carraher, Ph.D.



Evonne Rezler, Ph.D.



Fernando Uribe-Romo, Ph.D.



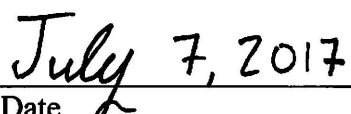
Gregg Fields, Ph.D.
Chair, Department of Chemistry and
Biochemistry



Ata Sarajedini, Ph.D.
Dean, Charles E. Schmidt College of
Science



Deborah L. Floyd, Ph.D.
Dean, Graduate College



Date

ACKNOWLEDGEMENTS

I would like to thank the members of my research committee, Drs. Charles Carraher, Evonne Rezler, and Fernando Uribe-Romo, for their time and advice.

I would like to thank the current and former members of my research lab for their advice, support, kindness, and friendship. Special thanks to Ryan Crichton, Kelly Rue, Heather Ten Hoeve, and Raul Ortega, who all played a role in this work.

I greatly appreciate all of the faculty and staff of the Department of Chemistry & Biochemistry at Florida Atlantic University for the help and support they provided to me. I would also like to thank Cynthia Marks, who always had time to listen.

Lastly, I would like to express my utmost appreciation for my fellow graduate students that made my time here memorable.

ABSTRACT

Author: Jeffrey D. Einkauf

Title: A New Approach to Sensitized Luminescence in Trivalent Lanthanide Coordination Polymers: From Fundamental Luminescence and Crystal Engineering Toward Sensing Applications

Institution: Florida Atlantic University

Dissertation Advisor: Dr. Daniel T. de Lill

Degree: Doctor of Philosophy

Year: 2017

Luminescent lanthanide containing coordination polymers and metal-organic frameworks hold great potential in many applications due to their distinctive spectroscopic properties. While the ability to design coordination polymers for specific functions is often mentioned as a major benefit bestowed upon these compounds, the lack of a meaningful understanding of the crystal engineering and luminescence in lanthanide coordination polymers remains a significant challenge toward functional design. Currently, the study of luminescence attributed to these compounds is based on the antenna effect as derived from molecular systems, where organic antennae are used to facilitate lanthanide-centered luminescence. This molecular based approach does not take into account the unique features of extended network solids, particularly the formation of band structure. By comparing molecular and band-based approaches, it was determined that the band structure of the organic sensitizing linker needs to be considered when

evaluating the luminescence of lanthanide coordination polymers. This new model, as well as work on the crystal engineering and sensor applications of these materials will be presented.

DEDICATION

First, I would like to thank my parents, Donald and Sandra Einkauf, for the patience and support throughout my career. Without you, this never could have been possible. I would also like to thank the members of my family have supported me in their own way (Bret, Brian, Heather, Tori, Matthew, Maya, and Murphy).

A special thank you to Alyssa Cordani, who gave unrelenting moral and emotional support throughout this endeavor. She became pillar of strength in my life throughout the entire doctoral process.

I dedicate this work and give special thanks to Dr. de Lill, who has been an incredible mentor and taught me to not only be a scientist, but taught me to be a better person. His support and guidance helped me through adversity during my graduate career and instilled in me a tireless work ethic and persistent determination.

A NEW APPROACH TO SENSITIZED LUMINESCENCE IN TRIVALENT
LANTHANIDE COORDINATION POLYMERS: FROM FUNDAMENTAL
LUMINESCENCE AND CRYSTAL ENGINEERING TOWARD SENSING
APPLICATIONS

List of Tables	xii
List of Figures	xv
Chapter 1: Introduction	1
1.1 Framework Materials	1
1.1.1 Development.....	1
1.1.2 Syntheses	3
1.1.3 Band Formation in Solids	3
1.2 The Lanthanide Series	5
1.2.1 General Overview of the Lanthanide Elements.....	5
1.2.2 Lanthanide Coordination Polymers	7
1.3 Luminescence in Metal-Organic Frameworks	10
1.3.1 Spectroscopy of Lanthanide Ions	10
1.3.2 Obtaining Luminescence in Metal-organic Frameworks	11
1.3.3 The Antenna Effect.....	12
1.4 Applying a Band-based Approach to Sensitized Luminescence in MOFs	14
Chapter 2: Synthesis and characterization	15

2.1 Materials and Methods	15
2.1.1 Hydrothermal Synthesis	15
2.1.2 X-ray Diffraction	16
2.1.3 Luminescence Spectroscopy.....	20
2.1.4 Photophysical Measurements	21
Chapter 3: Luminescence lanthanide coordination polymers constructed from heterocyclic linkers	25
3.1 3,4-Furandicarboxylic Acid	25
3.1.1 Synthesis.....	25
3.1.2 Structural Description.....	26
3.1.3 Photophysical Results and Analysis	34
3.2 2,3-Pyridinedicarboxylic Acid	37
3.2.1 Synthesis.....	38
3.2.2 Structural Description.....	39
3.2.3 Photophysical Results and Analysis	45
3.3 Furan and Pyridine Systems within the Antenna Effect	47
3.4 Conclusion.....	48
Chapter 4: 4,4'-benzophenonedicarboxylic acid system	
4.1 Benzophenone-4,4'- dicarboxylic Acid.....	49
4.1.1 Synthesis.....	49
4.1.2 Structural Description.....	50
4.2 Photophysical Results	56
4.2.1 Excitation and Emission Spectra	56

4.2.2 Analysis of Photophysical Data.....	58
4.3 Deuterated and Dehydrated Analogs.....	58
4.3.1 Syntheses	59
4.3.2 Excitation and Emission Spectra	59
4.3.3 Results and Discussion	61
4.4 Conclusion.....	69
Chapter 5: The band model of sensitized luminescence in trivalent lanthanide	
coordination polymer systems	71
5.1 Synthesis.....	72
5.2 Results and Discussion.....	75
5.2.1 Evaluation of Molecular-Based Approach	81
5.2.2 Evaluation of Band-Based Approach.	85
5.2.3 Further Considerations of the Band Nature of Organic Solids.....	89
5.2.4 Triplet versus Spectral Overlap Approaches	90
5.2.5 Influence of High-Energy Vibrational Quanta	91
5.2.6 Topological Impact on Sensitized Luminescence	92
5.2.7 Quantitative Assessment of Eu Emission.....	94
5.3 An alternative to the antenna model for molecular complexes.....	95
5.4 Conclusion.....	98
Chapter 6: Effects of lanthanide doping in $[\text{Ln}(\text{C}_6\text{H}_8\text{O}_4)_3(\text{H}_2\text{O})_2] \cdot (\text{C}_{10}\text{H}_8\text{N}_2)$,	
GWMOF-6.....	99
6.1 Synthesis.....	100
6.2 Doping and Powder X-ray Diffraction.....	100

6.3 Photophysical Results	103
6.3.1 Eu:Gd and Tb:Gd GWMOF-6 systems	103
6.3.2 Eu:Tb GWMOF-6 System.....	107
6.4 Conclusion.....	109
Chapter 7: A lanthanide coordination polymer based on 2,2'-bithiophene-5,5'- dicarboxylate for nitroaromatic detection.....	111
7.1 Synthesis.....	112
7.1.1 Synthesis of 2,2'-bithiophene-5,5'-dicarboxylic acid	112
7.1.2 Synthesis of $[\text{Er}_2(\text{C}_{10}\text{H}_4\text{O}_4\text{S}_2)_3(\text{H}_2\text{O})_6]_n$	113
7.1.3 Single crystal X-ray Diffraction	114
7.1.4 Luminescence	114
7.2 Structural Description	115
7.3 Luminescence and Sensing Properties	120
7.4 Conclusion.....	128
Chapter 8: Reticular chemistry and secondary building unit formation in trivalent lanthanide systems under hydrothermal conditions	129
8.1 Synthesis and Characterization	131
8.2 Investigation into Hydrothermal Conditions.....	131
8.2.1 Contour Plots	131
8.2.2 Matched Crystal Structures	139
8.3 Conclusion.....	142
References.....	144

LIST OF TABLES

Table 1. <i>Comparison of 4f and 3d metal ions. [35]</i>	10
Table 2. <i>Crystallographic information for Eu and Tb FDC-CPs.</i>	27
Table 3. <i>Selected bond lengths for Eu and Tb FDC CPs.</i>	31
Table 4. <i>Hydrogen bonding geometric parameters (Å, °).</i>	32
Table 5. <i>Quantum yields and lifetimes of the Eu and Tb analogs of Ln-FDC.</i>	35
Table 6. <i>Luminescence parameters of the Eu FDC system.</i>	37
Table 7. <i>Crystallographic details for the Ln-PYDC compounds,</i> <i>[Ln(C₇H₃NO₄)(C₇H₄NO₄)(H₂O)]_n (Ln = Pr, Nd, Sm, Eu, Tb).</i>	39
Table 8. <i>Selected bond lengths (Å) and angles (°) for the Eu-PYDC compound.</i>	44
Table 9. <i>Hydrogen bond parameters for Eu-PYDC system.</i>	45
Table 10. <i>Quantum yields and lifetimes of the Eu and Tb analogs of Ln-PYDC.</i>	47
Table 11. <i>Luminescence parameters of the Eu PYDC system.</i>	47
Table 12. <i>Crystallographic information for the Eu-BPDC CP.</i>	53
Table 13. <i>Selected bond lengths (Å) for the Eu-BPDC CP.</i>	54
Table 14. <i>Hydrogen bonding interactions and distances (Å) within the Eu-BPDC CP</i> <i>system.</i>	55
Table 15. <i>π-π stacking interactions in the Eu-BPDC system.</i>	55
Table 16. <i>Photophysical measurements of Eu and Tb BPDC systems.</i>	67
Table 17. <i>Bound water determination results for Eu- and Tb-BPDC.</i>	68

Table 18. <i>Luminescence parameters of the hydrated, deuterated, and dehydrated Eu BPDC systems.</i>	69
Table 19. <i>Quantum yield (%), lifetime (ms), number of OH quanta, secondary building unit, and overall dimensionality of Eu and Tb analogs of 1 – 9.</i>	84
Table 20. <i>Photophysical measurements of each system in the molecular and CP states with Gd(III).</i>	84
Table 21. <i>Difference from energy levels of linker to energy states of Ln(III) ions.</i>	89
Table 22. <i>Luminescence parameters for compounds 1 – 9.</i>	95
Table 23. <i>Elemental analyses of the doped systems of [Eu_xGd_y(C₆H₈O₄)₃(H₂O)₂].4,4'-dipy.</i>	102
Table 24. <i>Elemental analyses of the doped systems of [Tb_xGd_y(C₆H₈O₄)₃(H₂O)₂].4,4'-dipy.</i>	102
Table 25. <i>Elemental analyses of the doped systems of [Eu_xTb_y(C₆H₈O₄)₃(H₂O)₂].4,4'-dipy.</i>	102
Table 26. <i>Quantum yield and lifetime values for [Ln_xLn_{1-x}(C₆H₈O₄)₃(H₂O)₂].4,4'-dipy (where Ln_x = Eu or Tb, and Ln_{1-x} = Gd).</i>	106
Table 27. <i>Luminescence parameters for Eu:Gd systems (100:0, 75:25, 50:50, and 25:75 ratios)</i>	107
Table 28. <i>Quantum yield and lifetime values for Eu:Tb 50:50 system at the maximum emission of Eu (545 nm) and Tb (617 nm).</i>	109
Table 29. <i>Crystallographic information for the Er-DTDC CP.</i>	117
Table 30. <i>Selected bond lengths for Er-DTDC.</i>	119

Table 31. <i>Intermolecular interactions between neighboring centroids where Cg(1) is S(1), C(2), C(3), C(4), C(5), Cg(2) is S(2), C(6), C(7), C(8), C(9), and Cg(3) is S(3), C(12), C(13), C(14), C(15).....</i>	120
Table 32. <i>Quenching rates and efficiencies of nitroaromatic analytes with Er-DTDC in ethanol.</i>	124
Table 33. <i>HOMO and LUMO energies calculated for DTDC linker and analytes.</i>	126
Table 34. <i>Crystal data of compounds 1 – 3.....</i>	142

LIST OF FIGURES

Figure 1. <i>Examples of various secondary building units in lanthanide coordination polymers. Here, zero-dimensional monomers (pink), dimers (blue), trimers (grey), and tetramers (beige) are shown on the left. Higher-dimensional SBUs such as one-dimensional chains (green, top right) and two-dimensional sheets (orange, bottom right) are also shown.</i>	2
Figure 2. <i>Orbital energies for an increasing number of N atoms in a solid.</i>	5
Figure 3. <i>Radial distribution plot of the s, p, d, and f valence orbitals in Ln ions. [37].</i>	7
Figure 4. <i>Molecular orbital diagram for metal (A) and ligand (B) interactions using Pearson's Hard/Soft Acid/Base Theory.</i>	9
Figure 5. <i>A modified Jablonski diagram depicting the antenna effect. A=absorption, F=fluorescence, P=phosphorescence, L=Luminescence, NRD=non-radiative decay, ¹S=singlet state, ³T=triplet state, ISC=intersystem crossing, ET=energy transfer, BT=back transfer.</i>	13
Figure 6. <i>Simplified scheme for hydrothermal synthesis.</i>	16
Figure 7. <i>A simplified schematic of a typical X-ray tube. A high voltage across a (tungsten) filament ejects electrons through a vacuum to the (water cooled) metal anode, generating X-rays that may pass through beryllium windows.</i>	17
Figure 8. <i>Simplified schematic of X-ray generation from an electron beam source.</i>	18
Figure 9. <i>Schematic derivation of Bragg's Law. Where an X-ray strikes an atom on a crystallographic plane and is diffracted off at the same angle, θ.</i>	19
Figure 10. <i>Simplified representation of Förster and Dexter energy transfer mechanisms.</i>	21

Figure 11. Thermal ellipsoid plots (50% level) of all crystallographically unique atoms in Eu-FDC CP (where <i>i</i> indicates the symmetry operator $-x, -y, -z$). Hydrogen atoms have been omitted.....	28
Figure 12. View of $[Eu(C_6H_2O_5)(C_6H_3O_5)(H_2O)]_n$ down $[010]$, showing the stacking of the layers. Note the uncoordinated FDC ion between the layers. Orange polyhedra represent EuO_8 units, black lines are carbon, and red spheres are oxygen atoms. Hydrogens have been omitted for clarity.....	29
Figure 13. The structure of an individual layer in the title compound, highlighting the dimer SBU structure. See Figure 12 for color scheme.	30
Figure 14. Ball and stick representation of the lanthanide dimer. Carbon atoms are black, oxygen is red, hydrogen atoms are white, and the purple spheres are the lanthanide centers.....	33
Figure 15. Eu-FDC compound excitation (dashed) and emission (solid).....	35
Figure 16. Tb-FDC compound excitation (dashed) and emission (solid).....	36
Figure 17. A thermal ellipsoid plot for the title compound shown at the 50% probability level. Hydrogen atoms are omitted.	41
Figure 18. Polyhedral representation of the sheets in the Ln-PYDC compound, highlighting the dimers.	42
Figure 19. View of the Ln-PYDC compound down $[001]$ where the hydrogen bonding (dashed lines) that connect the 2-D sheets down the $[100]$ direction is shown.	43
Figure 20. Excitation (left) and emission (right) spectra of Eu-PYDC.....	46
Figure 21. Excitation (left) and emission (right) spectra of Tb-PYDC.....	46

Figure 22. <i>Crystal structure of the Eu-BPDC compound down the [010] direction. Orange polyhedra represent Eu monomers, red spheres are oxygen atoms, and black lines are carbon atoms. Hydrogen atoms have been removed for clarity.</i>	51
Figure 23. <i>Crystal structure of the Eu-BPDC compound down the [100] direction, showing the monomer SBU. For color scheme, see Figure 22.</i>	52
Figure 24. <i>Thermal ellipsoid plot (50% probability level) of [Eu(C₁₅H₉O₅)₃(H₂O)₃]_n (symmetry equivalent atoms are denoted by superscripts: <i>i</i> = <i>x</i>, 1-<i>y</i>, 1/2+<i>z</i>). Hydrogen atoms have been omitted.</i>	52
Figure 25. <i>Excitation (black) and emission (red) spectrum of Eu-BPDC.</i>	57
Figure 26. <i>Excitation (black) and emission (green) spectrum of Tb-BPDC.</i>	57
Figure 27. <i>Emission spectra of Eu-BPDC. Black spectra are for the unmodified, as-synthesized hydrated samples; blue spectra represent the emission for the deuterated analogues; red spectra represent the emission for the dehydrated analogs.</i>	60
Figure 28. <i>Emission spectra of Tb-BPDC. Black spectra are for the unmodified, as-synthesized hydrated samples; blue spectra represent the emission for the deuterated analogues; red spectra represent the emission for the dehydrated analogues.</i>	61
Figure 29. <i>Analysis of the energy transfer mechanisms based on lowest lying singlet and triplet state values (left; molecular BPDC triplet state shown for reference as a dashed line) and that of donor/acceptor spectral overlap</i>	

<p>(right; emission spectra at 0.0, 0.3, and 0.5 ms delay with decreasing singlet state energy; singlet and triplet band levels noted * for reference on 0.3 ms delay spectrum.</p>	64
Figure 30. Linkers used in compounds 1 – 9	76
Figure 31. Structure (1) previously obtained by MacNeill et. al. with two dimensional sheets made of dimers.	77
Figure 32. Structure (2) reported by Reineke et. al. comprised of Ln(III) monomers into a prototypical MOF motif.....	78
Figure 33. Structure (3) synthesized by Serre et. al. comprised of two dimensional sheets made of lanthanide hydroxide sheets.	79
Figure 34. Structure (5) synthesized by Fan et. al. comprised of helical Ln(III) chains (blue) tethered together by 1,3-BDC linkers.	80
Figure 35. Structure (6) synthesized by Luo et. al. comprised of Ln(III) monomers (green) bridged by 4,4'-oxybis(benzoic acid).	80
Figure 36. Modified Dieke diagrams of Eu, Gd, and Tb ions with experimentally obtained energy levels of the molecular triplet states (left, red) and triplet bands (right, blue) of the linkers and CPs used. Since 1,3-BDC and 1,4-BDC have the same triplet band energies, they have been combined in the band figure for clarity.	88
Figure 37. Proposed band model diagram where an electron is promoted from the valence band to conduction band, charge carrier recombination occurs and the energy is then transferred to the manifold of the Ln ion. The emissive	

	<i>state of the Ln ion is occupied through internal conversion, followed by luminescence. Here, ET=energy transfer, IC=internal conversion.</i>	97
Figure 38.	<i>Powder X-ray diffraction pattern of Eu:Gd-GWMOF-6 analogs at 100:0, 75:25, 50:50, and 25:75 doping ratios.</i>	101
Figure 39.	<i>Powder X-ray diffraction pattern of Eu:Gd-GWMOF-6 analogs at 100:0, 75:25, 50:50, and 25:75 doing ratios.</i>	101
Figure 40.	<i>Modified Dieke diagram of Eu, Gd, and Tb ions.</i>	104
Figure 41.	<i>Emission spectra of the Eu:Gd analog of GWMOF-6 at 100:0, 75:25, 50:50, and 25:75 concentration ratios.</i>	105
Figure 42.	<i>Emission spectra of the Tb:Gd analog of GWMOF-6 at 100:0, 75:25, 50:50, and 25:75 concentration ratios.</i>	105
Figure 43.	<i>Emission spectrum of the Eu:Tb analog of GWMOF-6 at a 50:50 concentration ratio.</i>	109
Figure 44.	<i>Synthesis of DTDC linker.</i>	113
Figure 45.	<i>DTDC product ¹H NMR (400 MHz, DMSO, ppm) δ7.70 (d, 2H), 7.54 (d, 2H).</i>	113
Figure 46.	<i>DTDC product ¹³C NMR (101 MHz, DMSO, ppm) δ175.84, 163.14, 142.06, 134.95, 127.08.</i>	113
Figure 47.	<i>View of Er-DTDC down the [100] direction. Magenta polyhedra represent Er monomers, yellow spheres are sulfur atoms, red spheres are oxygen atoms, and black lines are carbon atoms. Hydrogen atoms have been omitted for clarity.</i>	116

Figure 48. <i>Thermal ellipsoid plot (50% level) of Er-DTDC (where superscripts indicate symmetrically generated atoms, I = 1 - x, 2 - y, -z; ii = 1 - x, 1 - y, 2 - z; and iii = 2 - z, 1 - y, 1 - z). Hydrogen atoms have been omitted.....</i>	118
Figure 49. <i>View of Er-CP down [100] illustrating the bridging of the carboxylate groups connecting ErO₈ polyhedra, illustrating the monomer SBU structures.</i>	118
Figure 50. <i>Emission spectra of Er-DTDC and the DTDC linker in ethanol ($\lambda_{exc} = 371$ nm).</i>	121
Figure 51. <i>Emission spectrum of Er-DTDC and additions of analytes at 1 mM concentration, excited at 371 nm.</i>	122
Figure 52. <i>Percentage of photoluminescence quenching of Er-DTDC upon addition of analytes.</i>	122
Figure 53. <i>Spectral overlap between the absorption of aromatic analytes and the emission of Er-DTDC in ethanol.</i>	125
Figure 54. <i>HOMO and LUMO energy levels of the DTDC linker and nitroaromatic analytes, as well as representations of these molecular orbitals. These compounds are ordered in decreasing quenching ability.....</i>	126
Figure 55. <i>Stern-Volmer plot of Er-DTDC in ethanol with 1 mM 4-nitrophenol 5 μL increments at an excitation wavelength of 371 nm.</i>	127
Figure 56. <i>Linker versus lanthanide concentration contour plot obtained from hydrothermal methods. Here, light blue is no reaction and green is recrystallized linker (terephthalic acid).</i>	132

Figure 57. <i>Lanthanide concentration versus temperature contour plot using hydrothermal methods. Here, light blue is no reaction and green is recrystallized linker (terephthalic acid).</i>	134
Figure 58. <i>Linker concentration versus temperature contour plot using hydrothermal methods. Here, light blue is no reaction and green is recrystallized linker (terephthalic acid).</i>	135
Figure 59. <i>Lanthanide concentration versus time contour plot from hydrothermal methods. Here, light blue is no reaction, green is recrystallized linker (terephthalic acid), and orange is compound 1.</i>	136
Figure 60. <i>Linker concentration versus time contour plot from hydrothermal methods. Here, light blue is no reaction, green is recrystallized linker (terephthalic acid), and orange is compound 1.</i>	137
Figure 61. <i>Lanthanide to linker concentration ratio versus temperature contour plot from hydrothermal methods. Here, light blue is no reaction, green is recrystallized linker (terephthalic acid), and orange is compound 1.</i>	138
Figure 62. <i>Lanthanide to linker concentration ratio versus time contour plot from hydrothermal methods. Here, light and dark blue are no reaction, green is recrystallized linker (terephthalic acid), orange is compound 1, and red is a mixture of compounds 2 and 3.</i>	139
Figure 63. <i>View of the AMIXIE (1) structure down the [100] direction. Here, pink polyhedra are Er atoms, red spheres are oxygen atoms, and black lines are carbon atoms.</i>	140

Figure 64. View of *NELRAY (2)* structure down the $[100]$ direction. Here, blue polyhedra are Er atoms, red spheres are oxygen atoms, and black lines are carbon atoms. 140

Figure 65. View of *NERMON (3)* structure down the $[001]$ direction. Here orange polyhedra are Er atoms, red spheres are oxygen atoms, and black lines are carbon atoms. 141

CHAPTER 1: INTRODUCTION

1.1 Framework Materials

1.1.1 Development

Coordination polymers (CPs) and metal-organic frameworks (MOFs) have had an incredible rise in applications over the past twenty years, owing to their porosity, large surface areas, and relative chemical and thermal stabilities. [1-6] The ability to target topologies for applications have made them particularly attractive in catalysis, gas storage and separations, ion exchange, magnetism, sensing, and luminescence. [7-13]

A coordination polymer or metal-organic framework is a coordination compound with repeating coordination entities extending in 1, 2, or 3 dimensions. [14] This definition can be further refined to a subset known as coordination networks. This is when a coordination compound can be extended through repeating coordination entities in one dimension with cross linkers between two or more chains, or more simply, a coordination compound extended through repeating coordination entities in two or three dimensions. Therefore, a metal-organic framework is a coordination network with organic linkers containing permanent porosity. As some of the materials studied within this dissertation are dense, high dimensional solid structures, the compounds found herein will collectively be referred to as coordination polymers.

Coordination polymers contain two key components, metals and linkers. In CPs, the primary building unit (PBU) is the metal ion (here, lanthanide ions) and the primary

coordination sphere surrounding the metal center. The LnO_x polyhedra can be connected through the organic linker to form the framework. Alternatively, the metal may edge or face share with an adjacent metal polyhedron to form a secondary building unit (SBU) that may propagate into zero dimensional dimers, trimers, tetramers, etc., one dimensional chains, or two dimensional sheets (Figure 1).

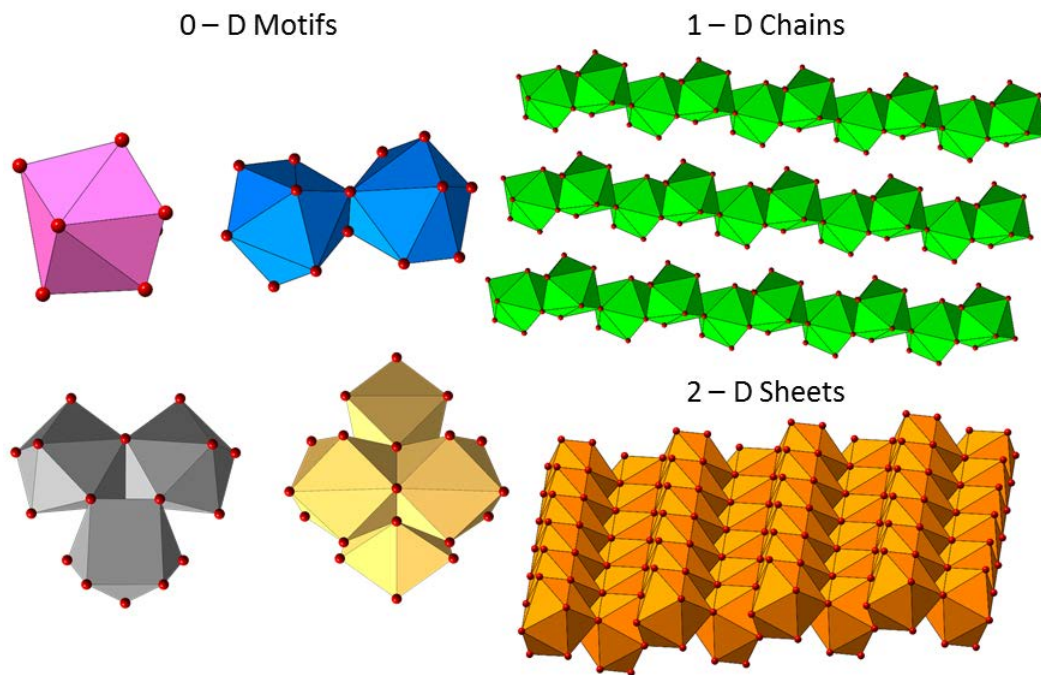


Figure 1. Examples of various secondary building units in lanthanide coordination polymers. Here, zero-dimensional monomers (pink), dimers (blue), trimers (grey), and tetramers (beige) are shown on the left. Higher-dimensional SBUs such as one-dimensional chains (green, top right) and two-dimensional sheets (orange, bottom right) are also shown.

One of the more important properties of MOFs is their high porosity. The porosity, which can have large pore apertures ranging as large as 98 Å, has allowed for loading of small molecules for gas storage to large biomolecules such as green

fluorescent proteins. [1, 15] Along with high porosity, high internal surface areas (up to 6,000 m² [16]) has led to numerous studies directed toward gas storage, separations, and catalysis. [17-20]

The permanent porosity of MOFs has led to the development of these materials as small-molecule sensors. Luminescent CPs have had an increase in development from the early stages of presentation of luminescence spectra, with no targeted applications, to sensing of toxic metals and explosive compounds. [21-26] Detailed spectroscopic analyses such as excitation spectra, lifetimes, quantum yields, energy transfer efficiency, and quenching constants are being provided more consistently as the field matures.

1.1.2 Syntheses

Coordination polymers and metal-organic frameworks can be synthesized under relatively mild reaction conditions. The most common method and the one used herein is hydro- or solvothermal synthesis. Reagents are dissolved upon heating in a sealed container under autogenous pressure. Within the sealed container, the increased pressure upon heating allows the water in the chamber to be heated above the normal boiling temperature. The objective of these methods is that the reactants such as the organic linker, which is generally not soluble in aqueous media, will dissolve at elevated temperatures and pressures. The presence of hydroxide ions from the addition of small amounts of base may also be added to form insoluble lanthanide-hydroxide species, which may initiate growth processes. [27]

1.1.3 Band Formation in Solids

The nature of bonding in solids is quite different than what is observed in small molecules. There are two general models for bonding in solids: the sea of electrons and

molecular orbital theory. In the sea of electrons model, the electrons from the valence orbitals of the metal delocalize, allowing for electrons to move freely throughout the space around the metal nuclei. In molecular orbital theory, molecular orbitals form when atomic orbitals overlap between two or more atoms. This concept can be extended from simple diatomic molecules to extended network solids with over 10^6 atoms.

For solids with N number of atoms, there will be N molecular orbitals. The lowest energy orbital will be that in which all the $1s$ orbitals combine in phase, and the highest energy orbitals will be that in which the orbitals all combine out of phase. This bonding allows for $N-2$ molecular orbitals in which there is some interaction between in-phase and out-of-phase combinations, the greater the overlap of orbitals, the greater the bandwidth. Figure 2 is a plot of the energy levels as the number of atoms gradually increases. When the atoms increase to such a large number, the separation between energy levels becomes infinitesimally small (e.g. on the order of 10^{-35} J). This separation is so small, the set of levels form a continuous range of energies, where the highest occupied molecular orbital (HOMO) can be reassigned as the valence band (VB) and the lowest unoccupied molecular orbital (LUMO) is renamed the conduction band (CB).

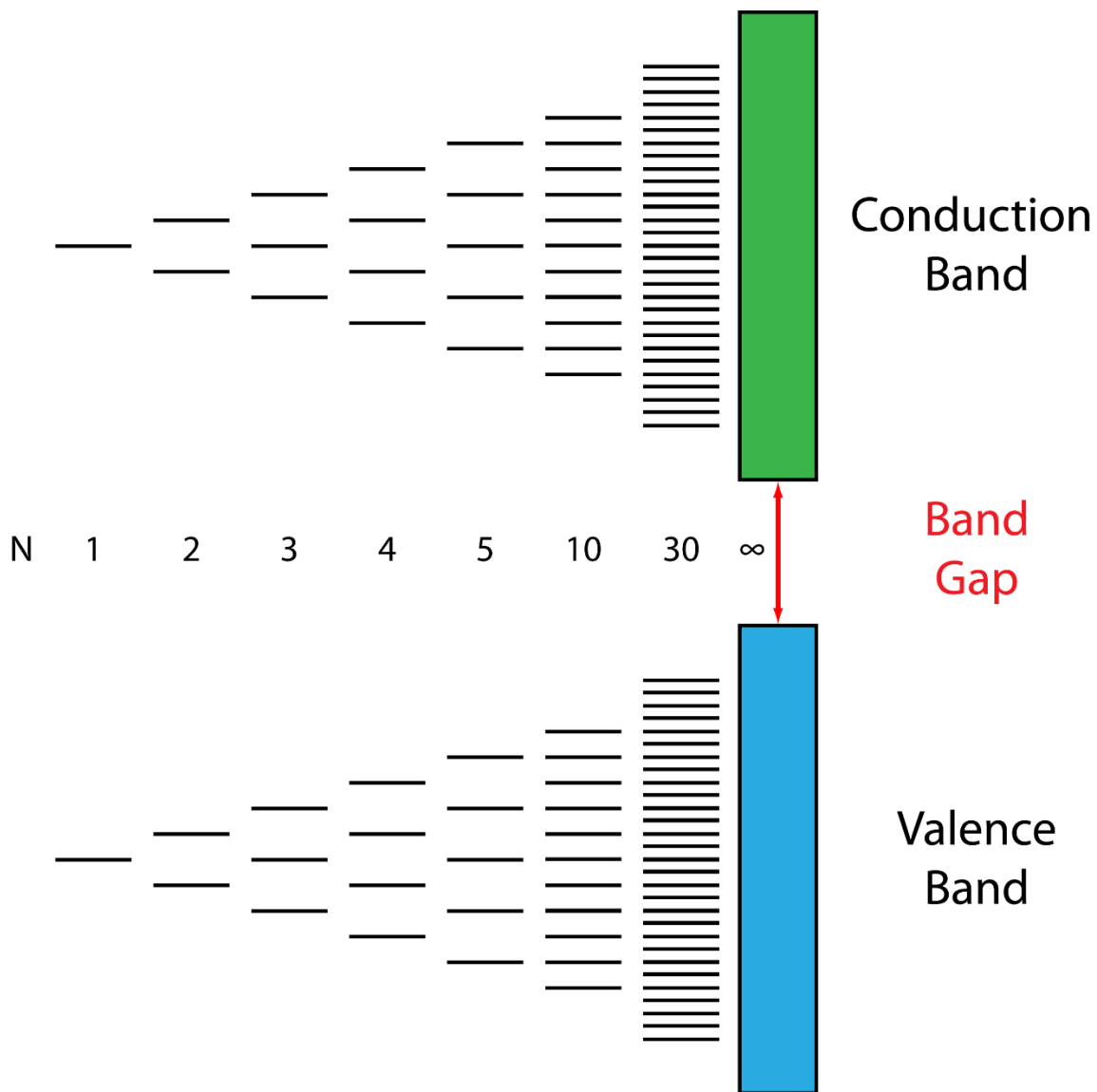


Figure 2. *Orbital energies for an increasing number of N atoms in a solid.*

1.2 The Lanthanide Series

1.2.1 General Overview of the Lanthanide Elements

“Lanthanum has only one important oxidation state in aqueous solution, the +3 state. With few exceptions, this tells the whole boring story about the other lanthanides.”

[28]

This quote is from Pimentel in 1971 and illustrates how under-appreciated the lanthanide series has been in the past. The chemistry and applications of lanthanide ions has made tremendous strides within the last 20+ years, with numerous applications of +2 oxidation states (mostly Eu and Yb) and increasing use in catalysis and lighting and display technologies. The lanthanide with any extensive chemistry in the +4 oxidation state is cerium and is primarily used as an oxidizing agent. [29-34]

The location of the lanthanides on the periodic table indicates that the filling of the 4f valence orbitals begins with these elements. The electronic configuration of the lanthanides is $[\text{Xe}]4f^n6s^2$, with notable exceptions for lanthanum, cerium, gadolinium, and lutetium, which have a $[\text{Xe}]4f^{n-1}5d^16s^2$ configuration. The most common oxidation state is +3, with a configuration of $[\text{Xe}]4f^{n-1}$. The 4f orbitals are considered valence orbitals; however, they are shielded from the coordination environment by the filled 5s and 5p orbitals, which are radially extended past the f orbitals (Figure 3). As a result, lanthanides bind mostly through, non-directional, ionic interactions. [35, 36] Lanthanide ions have a wide range of coordination numbers, typically ranging from 6 to 12 with coordination geometries being determined by ligand steric considerations rather than crystal field effects.

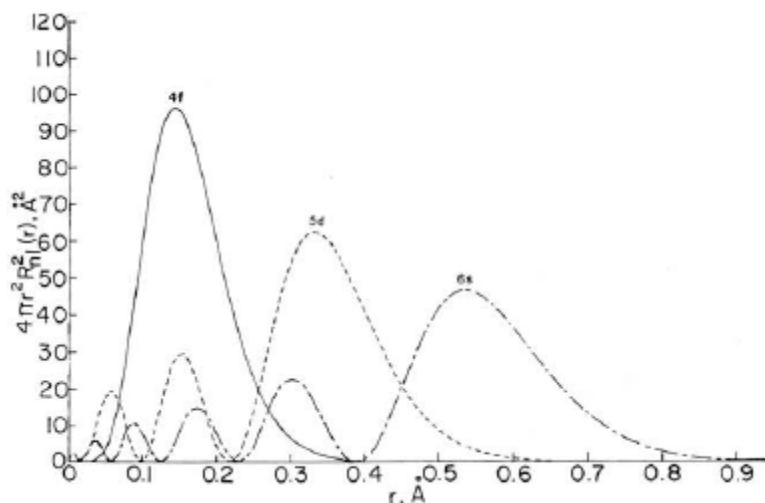


Figure 3. Radial distribution plot of the *s*, *p*, *d*, and *f* valence orbitals in *Ln* ions. [37]

1.2.2 Lanthanide Coordination Polymers

Lanthanide ions have not been used in coordination polymers as extensively as their transition metal counterparts. [4, 13, 17, 38-42] This is in part attributed to the predictable coordination geometries of transition metals, which in turn leads to predictable framework topologies in coordination polymer and metal-organic framework materials. This predictable formation in topologies is not largely present in lanthanide systems due to the mainly ionic, nondirectional bonding nature of these ions. This coupled with their large ionic radii presents another problem, fully saturating the coordination sphere of the lanthanide with desired ligands. Smaller molecules with less steric bulk will attempt to coordinate to open sites on the lanthanide center. This is seen often with solvent molecules, which will coordinate to lanthanide ions. This may seem like an additional challenge in lanthanide framework materials, but the large diversity and coordination geometries available opens up a wide array of possible topologies for these materials; possibilities far more extensive than the transition metal counterparts alone. A

comparison of some of the properties between transition and lanthanide metal behavior can be seen in Table 1. [35]

The primary method to control topologies in lanthanide coordination polymers; however, they are not quite the same as in transition metal systems. Selection of linkers and/or ligands that have the ability to complete the coordination sphere, attempting to exclude or crowd out any solvent molecules is the most elegant solution to attempt to avoid unwanted coordinating solvent molecules.

Another consideration when selecting a proper organic species for coordination to the lanthanide ion is based on Pearson's Hard/Soft Acid/Base Theory (HSAB, Figure 4). [43, 44] Charge density is the main focus of this concept. Transition metal species can be both hard and soft acids, where lanthanide ions, with an oxidation state of +3 and sizes ranging from 86.1 to 103.2 pm [35, 45], are all inherently hard acids. Hard bases typically employed contain oxygen atoms from carboxylic acid functional groups. This functional group is ideal as it readily chelates to the lanthanide ion.

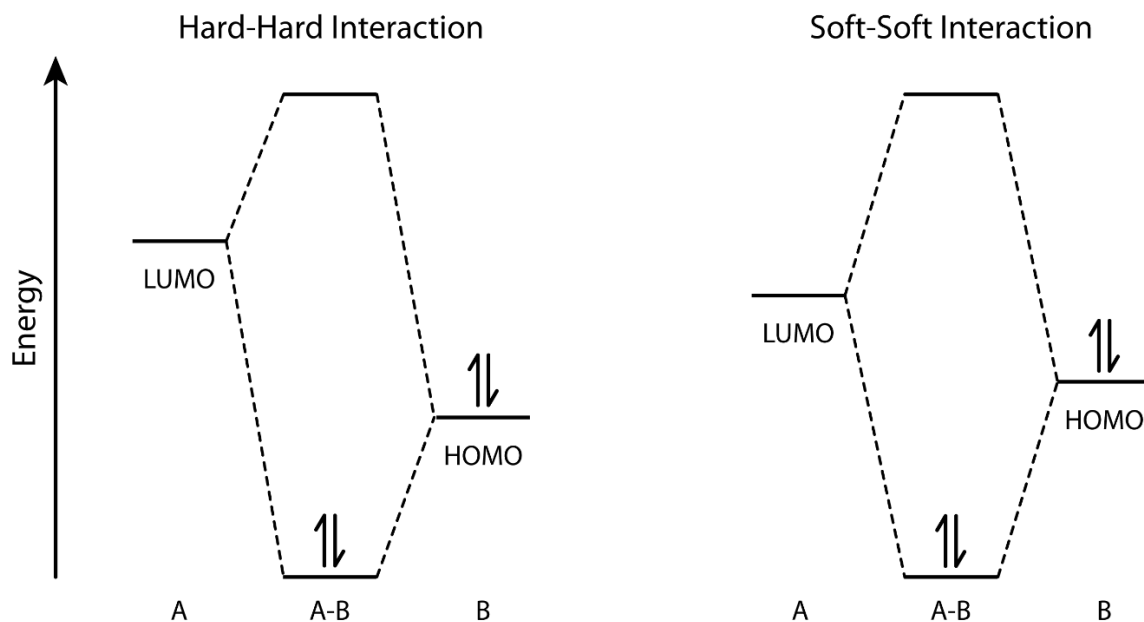


Figure 4. *Molecular orbital diagram for metal (A) and ligand (B) interactions using Pearson's Hard/Soft Acid/Base Theory.*

The reasons stated above substantiate that the field of lanthanide and lanthanide related materials such as metal-organic frameworks have the potential to offer substantial benefits to society, from hydrogen gas storage in cars [46] to better LED lighting [47], and medicine. [48-50]

Table 1. Comparison of 4f and 3d metal ions. [35]

	4f	3d
Electron configurations of ions	Variable	Variable
Stable oxidation states	Usually +3	Variable
Coordination numbers in complexes	Commonly 8 - 10	Usually 6
Coordination polyhedra in complexes	Minimize repulsion	Directional
Trends in coordination numbers	Often constant in block	Often constant in block
Donor atoms in complexes	'Hard' preferred	'Hard' and 'soft'
Hydration energy	High	Usually moderate
Ligand exchange reactions	Usually fast	Fast and slow
Magnetic properties of ions	Independent of environment	Depends on environment and ligand field
Electronic spectra of ions	Sharp lines	Broad Lines
Crystal field effects in complexes	Weak	Strong

1.3 Luminescence in Metal-Organic Frameworks

1.3.1 Spectroscopy of Lanthanide Ions

The unique spectroscopy that arises from lanthanide ions is attributed to the 4f valence orbitals, which are buried within the core of the ions, shielded from the coordination environment by the filled 5s and 5p orbitals. As a consequence, they do not experience significant coupling with ligands. The transitions from the excited to ground states are forbidden by the Laporte selection rule since there is no change in the angular momentum quantum number between the excited and ground state. Judd and Ofelt explained the relaxation of the parity rule can be accomplished through the effect of vibronic coupling and hybridization. [51-53]

Due to the shielding of the 4f orbitals by the s and p orbitals, the spectral properties of lanthanide ions are minimally perturbed by the external field generated by

ligands or counterions. This results in the sharp f-f absorption bands compared to the broader d-d absorption bands of the d-block transition metals. The transitions observed in the lanthanide ions are Laporte forbidden, meaning there is no change of parity from the ground state to the excited state. Due to this, these transitions are weak in both absorptions and emission intensities, having molar absorptivities generally less than $10^4 \text{ M}^{-1}\text{cm}^{-1}$ and radiative lifetimes in the range of 0.1 to 1.0 ms. This is in drastic comparison to organic chromophores, with molar absorptivities greater than $10^4 \text{ M}^{-1}\text{cm}^{-1}$ and radiative lifetimes in the nanosecond time scale.

1.3.2 Obtaining Luminescence in Metal-organic Frameworks

In general, there are four methods for generating luminescence in MOFs. Lanthanide ions can be used in all four scenarios, where transition metal ions are primarily used for the first three scenarios. These methods are:

The first scenario is through (typically) conjugated organic compounds, which can absorb light in the UV and visible region. Emission can be directly from the linker, or can involve charge transfer between the metal ions and the organic moiety.

The second source of luminescence can come from adsorbed emitting species. The large porous voids in MOFs provide an ideal way to occlude luminescent molecules within its framework, making luminescence arise in an otherwise non-emissive material.

Next, π - π stacking interactions between adjacent linkers or between guest species and linkers can produce an excited complex (excimers/exciplexes) that can, in some scenarios, emit or quench luminescence.

Finally, metals within the framework may produce luminescence in certain circumstances. Lanthanide or transition metal ions incorporated into the MOF or CP as metal clusters can emit luminescence if within proximity of an organic molecule. This concept will be explored further and is the primary focus of this dissertation.

1.3.3 The Antenna Effect

Eu(III) and Tb(III) ions, are attractive visible light emitters because of their narrow emission profiles. These ions are often used in emissive materials, however, lanthanide electronic transitions are forbidden by parity (Laporte) selection rules, leading to weak absorbance and low efficiencies. The most commonly used method to circumvent this issue is through complexing the lanthanide with a strongly absorbing linker. In this process, commonly referred to as the antenna effect (Figure 5), an organic linker absorbs incident radiation and transfers the energy to the lanthanide's excited state, often resulting in radiative decay as luminescence. [54-56]

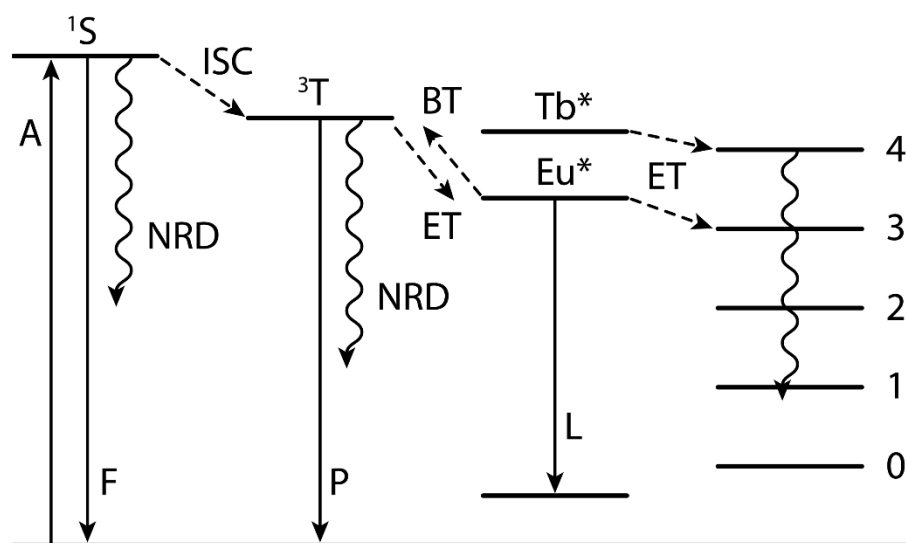


Figure 5. A modified Jablonski diagram depicting the antenna effect. *A*=absorption, *F*=fluorescence, *P*=phosphorescence, *L*=Luminescence, *NRD*=non-radiative decay, 1S =singlet state, 3T =triplet state, *ISC*=intersystem crossing, *ET*=energy transfer, *BT*=back transfer.

The antenna effect has long been used to justify luminescence in lanthanide coordination polymers, but treats coordination polymers like discrete molecular moieties rather than periodic network solids with band features. While well studied and developed in solution with discrete molecular entities, data herein indicates that coordination polymers do not behave in a similar fashion. [57, 58] Lack of dynamic ligand exchange, strong static hydrogen bonding networks, aggregation effects, and formation of band-like energy levels occur in CPs and may play roles that are not consistent with that of molecular complexes. Understanding the parameters by which sensitization occurs within trivalent Ln coordination polymers and metal-organic frameworks is the focus of this dissertation.

1.4 Applying a Band-based Approach to Sensitized Luminescence in MOFs

Since Ln CPs are not molecular entities, but rather network solids, [59, 60] a new ideology built upon the foundation of the antenna effect to explain Ln luminescence in CPs has been developed. The periodic arrangement of the metal centers with organic linkers results in the formation of band features similar to insulators and semiconductors. [61-63] When Ln ions are incorporated into inorganic semiconducting materials, their luminescence is often sensitized by charger carrier (exciton) recombination since there exists no organic antennae within these systems. Studies herein will demonstrate that a similar mechanism occurs in Ln CP systems, and that modifying the antenna effect guidelines for these systems is necessary. [60] This new approach applies known characteristics of aggregated organic solids with band structure to the antenna effect as derived from molecular systems.

CHAPTER 2: SYNTHESIS AND CHARACTERIZATION

2.1 Materials and Methods

To understand the luminescence of trivalent lanthanide ions in coordination polymers, these materials are prepared through hydrothermal synthesis and characterized using techniques including X-ray diffraction and luminescence spectroscopy. X-ray diffraction will determine the structure of the synthesized coordination polymer while luminescence spectroscopy gives insight into the light harvesting ability and photophysical processes occurring within these materials.

2.1.1 Hydrothermal Synthesis

The primary method of preparation discussed herein is hydrothermal synthesis (Figure 6). [64] The advantage of this technique is it allows an aqueous medium to be heated to a temperature greater than that of the normal boiling point of water under autogenous pressure. Solvothermal synthesis occurs when the reaction occurs in a solvent other than water. In a typical hydrothermal reaction, the reagents are weighed on a balance and placed into a 23 mL Teflon-lined steel autoclave. This vessel is then sealed and heated between 75 and 200 °C for varying hours to days. Once synthesized, the materials are analyzed with a variety of X-ray diffraction and spectroscopic techniques.

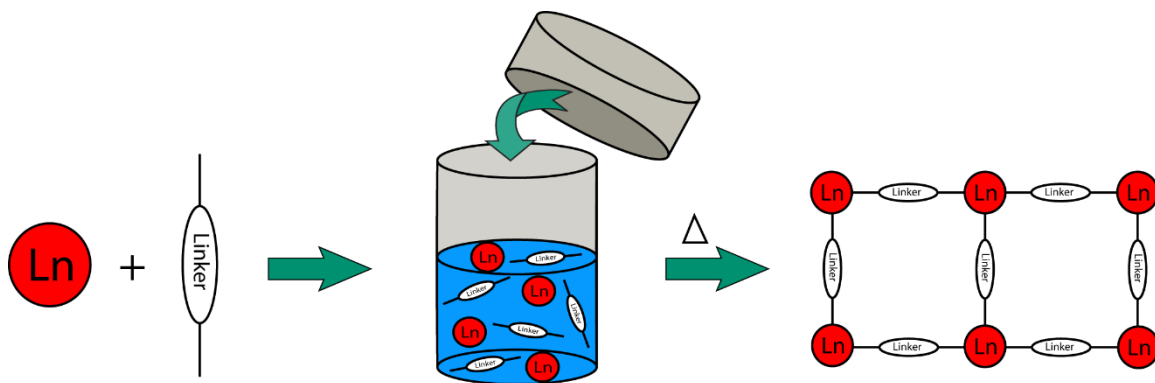


Figure 6. *Simplified scheme for hydrothermal synthesis.*

2.1.2 X-ray Diffraction

Once the coordination polymer has been synthesized through hydrothermal methods, X-ray diffraction techniques are used to determine the bond lengths and angles of a system through the use of X-rays.

X-rays are short-wavelength radiation on the order of 10^{-5} Å to 100 Å. Conventional X-ray diffraction is, however, typically used in the region of about 0.1 Å to 25 Å. [65, 66]

X-rays are generated in four main ways. The first method is by use of a radioactive source that decays resulting in X-ray emission. Another method is by exposing a substance to a primary beam of X-rays to generate a secondary beam of X-ray fluorescence. [67] Next, X-rays can be generated from a synchrotron radiation source. [68] Finally, the method that will be used for the generation of X-rays for the purpose of this dissertation is by bombardment of a metal target with a beam of high energy electrons (Figure 7).

In an X-ray tube, electrons produced at a cathode (typically tungsten wire) are accelerated toward a metal anode by a potential difference of about 100 kV. The

subsequent collision of the electrons with the anode creates mostly heat. But part of the energy of the beam (~1%) is converted to X-rays.

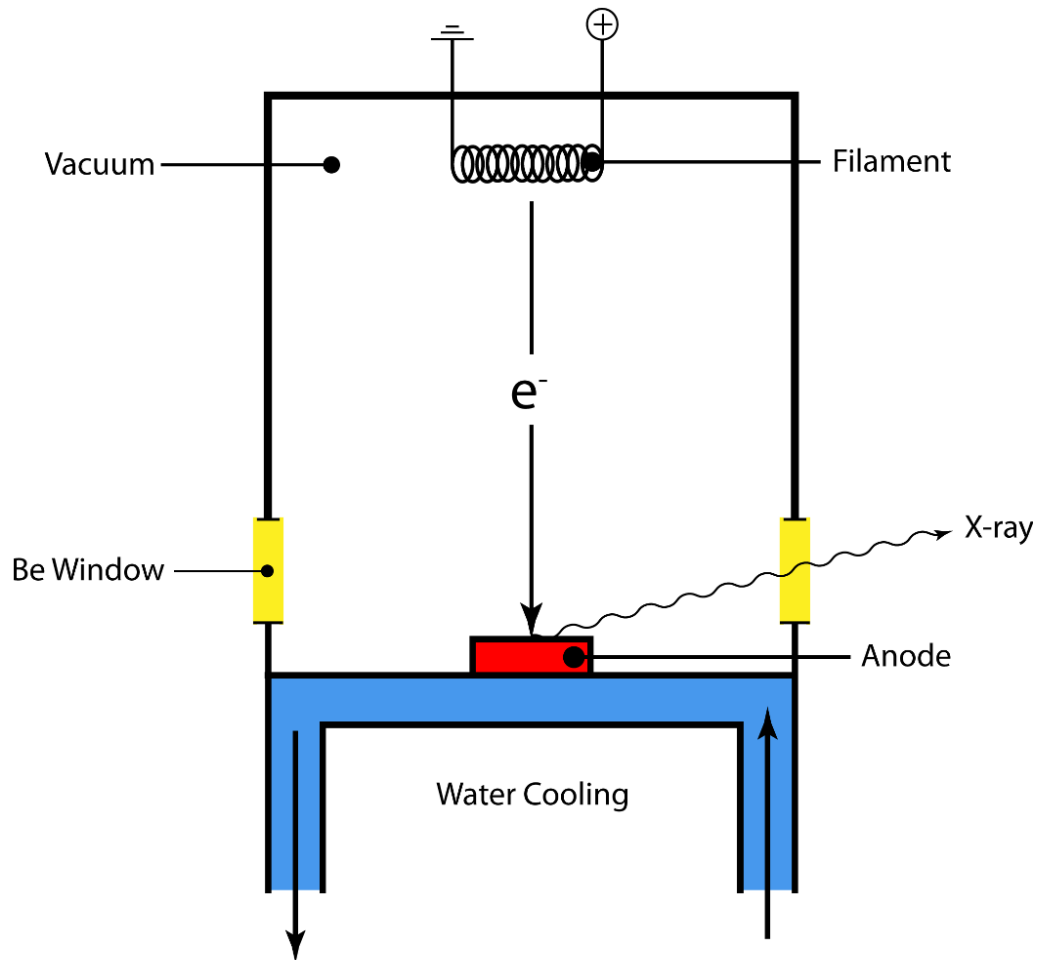


Figure 7. A simplified schematic of a typical X-ray tube. A high voltage across a (tungsten) filament ejects electrons through a vacuum to the (water cooled) metal anode, generating X-rays that may pass through beryllium windows.

X-rays result from the electronic transitions that involve innermost atomic orbitals of the anode material (typically molybdenum or copper). The high-energy electrons from the cathode ejects core electrons of the metal anode. The collision results in the formation of excited ions, which then emit quanta of radiation as electrons from outer

orbitals undergo transitions to occupy the inner, vacant orbital ($L \rightarrow K$ in Figure 8). An electron is lost from the second principal quantum level (L), as a result of ejection by a high energy electron from the cathode. The energy difference between the L and K levels is significantly larger than that between orbitals extended further out, closer to valence orbitals (M and L levels). Therefore, the radiation for the K series appears at shorter wavelengths for the heavier elements.

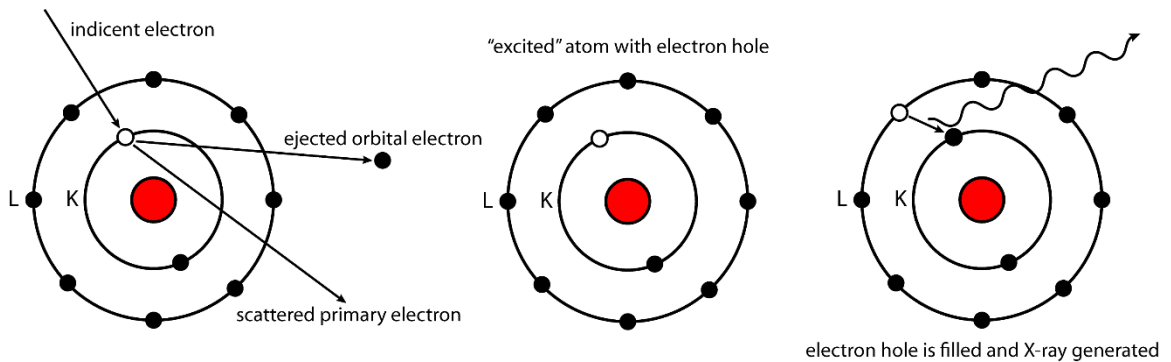


Figure 8. *Simplified schematic of X-ray generation from an electron beam source.*

When the generated X-ray beam strikes a crystalline material, part of the beam is scattered by the layer of atoms at the surface. The unscattered part of the beam penetrates to the second layer of atoms where again another fraction is scattered, while some penetrate further on to the third layer, so on and so forth. The cumulative effect of this scattering from the regularly spaced centers of the crystal is diffraction of the beam in a similar manner as visible radiation is diffracted by a reflection grating. The requirements for X-ray diffraction are that the spacing between layers of atoms must be roughly the same as the wavelength of the radiation and the scattering centers must be spatially distributed in a periodic arrangement.

W. L. Bragg treated diffraction of X-rays by crystals with trigonometric considerations (Figure 9). When a narrow beam of radiation strikes the crystal surface at

angle θ , scattering occurs as a result of the interaction of the radiation with atoms located directly above and below point y . The distance is thus defined as

$$xy + yz = n\lambda$$

where n is an integer (on the order of diffraction), the scattered radiation will be in phase at z , and the crystal will diffract the X-rays. If we look at this relation further,

$$xy = yz = d \sin \theta$$

where d is the interplanar distance of the crystal. The conditions for interference to be constructive for the X-ray beam are therefore,

$$n\lambda = 2d \sin \theta$$

which is known as Bragg's equation.

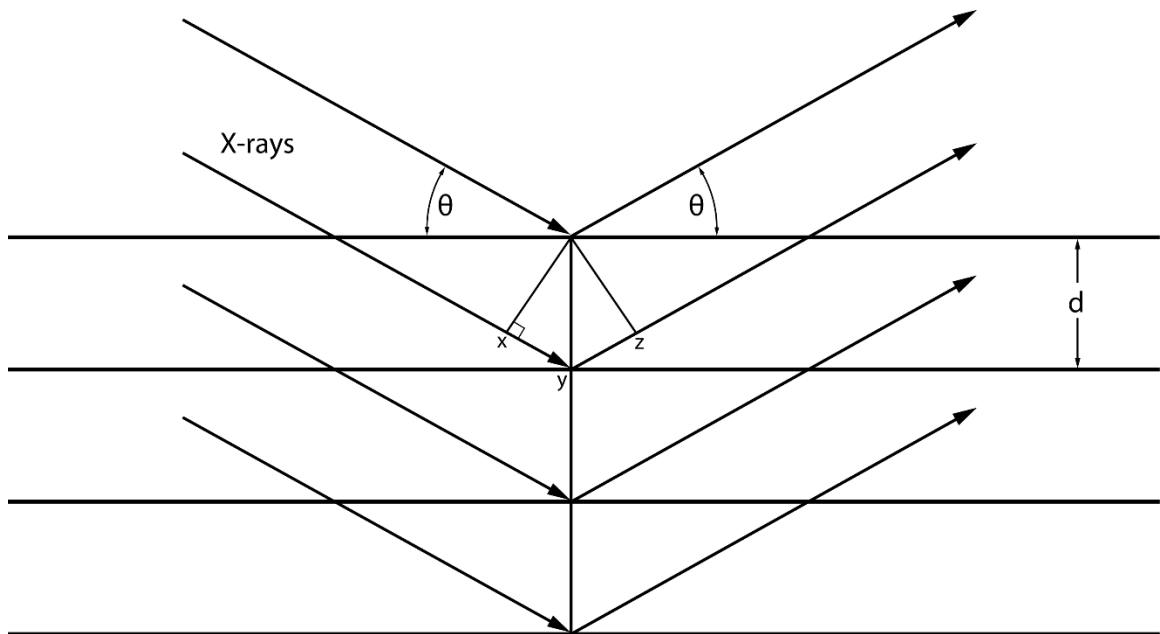


Figure 9. Schematic derivation of Bragg's Law. Where an X-ray strikes an atom on a crystallographic plane and is diffracted off at the same angle, θ .

The result of X-ray diffraction studies will provide diffraction patterns, which can be solved and refined to elucidate absolute bond lengths and angles of the crystalline material.

2.1.3 Luminescence Spectroscopy

Spectroscopic measurements are performed on the coordination polymers, which have been confirmed through X-ray diffraction methods, to investigate the photophysical processes that are occurring within these systems.

Luminescence occurs from the radiative emission of a photon from electronically excited states within compounds. Depending on the nature of the transition, fluorescence and/or phosphorescence may be the resulting process. Spin allowed fluorescence, a singlet to ground transition occurs rapidly, on the order of 10^8 s^{-1} , where spin forbidden phosphorescence is a relatively slower process on the order of 10^3 to 10^0 s^{-1} . Metal complexes and CPs can display mixed singlet and triplet state emission, which can last nanoseconds to several microseconds.

Luminescence in the systems described herein is achieved via an energy transfer mechanism. The donor and acceptor species are coupled by a dipole-dipole interaction, called Förster energy transfer, or by electron exchange through the Dexter energy transfer mechanism (Figure 10). This process of energy transfer is based on the concept of a fluorophore as an oscillating dipole. This dipole can exchange energy with another dipole with slightly small energy frequencies. This is the basis of the antenna effect, which will be discussed later.

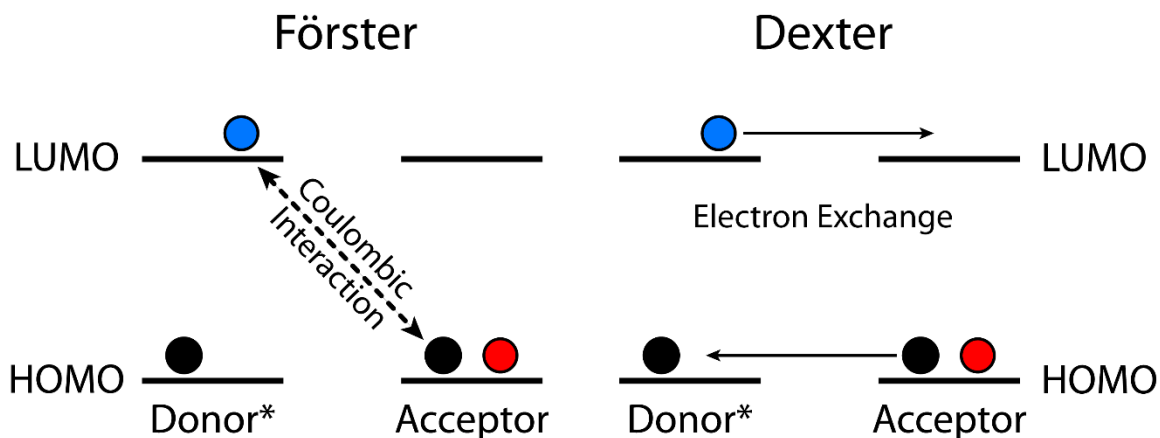


Figure 10. Simplified representation of Förster and Dexter energy transfer mechanisms.

2.1.4 Photophysical Measurements

Compounds synthesized will have their quantum yield determined to quantify the efficiency of the material. Quantum yield is a measurement of the ratio of photons emitted to the photons absorbed, allowing one to determine the efficiency of energy transfer processes in luminescent Ln systems. The method used to determine quantum yields in this dissertation is a relative technique, comparing light harvesting efficiency to known standards.

To reduce concentration quenching for the emitting materials, both samples and standards should be dissolved in a non-emissive matrix such as PMMA or KBr with enough thickness to avoid signal from the solid state holder (approximately 2 - 3 mm). [69, 70]

Diffuse reflectance (R) and the integrated emission spectrum (I) for both sample and standard can be used to calculate the emission efficiency of the solid state sample using the equation below.

$$\Phi_x = \frac{1 - R_{ST}}{1 - R_x} \times \frac{I_x}{I_{ST}} \times \Phi_{ST}$$

Reflectance can be determined from the UV-Vis spectrometer with solid state attachments with the value of reflected light of the sample and standards at designated wavelengths (313 nm for pyrene and 366 nm for anthracene). The emission spectrum of the sample and standards on the fluorimeter is scanned from the emissive ranges of the sample and integrated to obtain the I values from the equation. These values are then corrected by the absolute quantum yield of the standards (61% for pyrene and 22% for anthracene, both diluted in PMMA matrix).

The determination of excited state lifetimes are used to obtain information about the coordination environment of the lanthanide ion and the nature of the f-excited state. The lifetime is a measure of the average time the lanthanide remains in the excited state before decaying to the ground state. The lifetime of the excited state is strongly affected by non-radiative quenching pathways (OH, OD, CH quanta), the number of oscillators lead to non-radiative quenching in the coordination sphere of the lanthanide ion, which will be investigated extensively within the scope of this dissertation.

Emission lifetimes of Eu(III) and Tb(III) lanthanides with varying numbers of aqua ligands in aqueous solutions (τ_{H_2O}) were measured by Horrocks and compared to the lifetimes measured in D₂O (τ_{D_2O}). [56, 71] The number of bound water molecules, q , can be obtained from the equation,

$$q = A(\tau_{H_2O}^{-1} - \tau_{D_2O}^{-1})$$

where A was empirically determined (Eu is 1.05 and Tb is 4.2). This equation has been extended into the solid state, which will be applied to coordination polymers studies herein. Chopin also created another equation, which can determine lifetimes without deuterated solvent, however, this equation only works in Eu(III) systems. [72]

$$q = 1.05 \times \tau_{H_2O}^{-1} - 0.70$$

Together both quantum yield and lifetime measurements will allow for the quantification of the efficiency of these systems and allow for more insight into the energy transfer processes occurring within these systems.

The emission spectra of the europium compounds can also provide important information regarding radiative (κ_{rad}) and non-radiative (κ_{nonrad}) rates within Ln-organic systems, which offers insights into the luminescence of the Ln ion. These values can quantify how efficient the energy transfer process from the organic antenna to emitting Ln ion is as well as determine the negative contribution from nonradiative decay pathways, which will be covered in this dissertation. The intrinsic quantum yield of Eu(III) (Φ_{Eu}) can be determined, as well as the efficiency of the organic to sensitize Ln emission (η_{sens}), using the following equations. [73-75]

$$\Phi_{TOT} = \Phi_{Eu} \cdot \eta_{sens}$$

$$\Phi_{Eu} = \frac{\tau_{obs}}{\tau_{rad}}$$

$$\frac{1}{\tau_{rad}} = An^3 \left(\frac{I_{TOT}}{I_{MD}} \right)$$

$$\kappa_{nonrad} = \kappa_{obs} - \kappa_{rad} = \frac{1}{\tau_{obs}} - \frac{1}{\tau_{rad}}$$

Where Φ_{TOT} is the quantum yield of the system, τ_{obs} and τ_{rad} are the experimental and radiative lifetimes, respectively, A is the spontaneous emission probability of the 5D_0 to 7F_1 transition (14.65 s^{-1}), n is the refractive index (~ 1.5 for these solids), and $I_{TOT/MD}$ are the entire integrated Eu emission spectrum from 5D_0 to 7F_4 and the integrated magnetic-dipole emission band, $^5D_0 \rightarrow ^7F_1$, respectively.

Singlet and triplet states of the organic linkers are were performed as described by Crosby. [76] Phosphorescence spectra are collected with the linker with optically dead Gd(III) ions in a 3:1 ratio in acetonitrile solution, when appropriate. Spectra are collected with increasing delay times (0.00 to 0.05 ms) to resolve the long lived triplet state. Spectra are then deconvoluted with OriginPro 8.1 to determine singlet and triplet state energy levels.

CHAPTER 3: LUMINESCENCE LANTHANIDE COORDINATION POLYMERS
CONSTRUCTED FROM HETEROCYCLIC LINKERS

3.1 3,4-Furandicarboxylic Acid

The linker for the first project, 3,4-furandicarboxylic acid (FDC) [77], was chosen because this linker has not been studied with either transition metal or lanthanide metals without the presence of a second coordinating organic ligand. However, the linker 2,3,4,5-furantetracarboxylic acid has been used extensively in transition metal [78-81], lanthanide and actinide [82], and even alkali metal systems. [83] The absence of MOFs and CPs with this linker as well as the delocalized, rigid aromatic ring system of the furan moiety was motivation for the synthesis of Ln-FDC (Ln = Eu and Tb) systems to the study the fundamental luminescent properties these materials have to offer.

3.1.1 Synthesis

The coordination polymer $[\text{Ln}(\text{C}_6\text{H}_2\text{O}_5)(\text{C}_6\text{H}_3\text{O}_5)(\text{H}_2\text{O})]_n$ (Ln = Sm - Lu) [84] was synthesized hydrothermally from a solution of europium nitrate ($\text{Eu}(\text{NO}_3)_3 \cdot 6\text{H}_2\text{O}$, 122.6 mg, 0.275 mmol) and dimethyl-3,4-furandicarboxylate ($\text{C}_8\text{H}_8\text{O}_5$, 50 mg, 0.275 mmol) in 3 mL H_2O , which were placed into a 23 mL Teflon lined autoclave. Aqueous potassium hydroxide (5 M KOH) was added to adjust the pH from 2-3 to 7-9. The autoclave was placed in an oven at 120 °C for 3 days (72 h), after which the autoclave was removed from heat and left to naturally cool to room temperature. The cloudy, white

solution was decanted from the clear, colorless crystals, and washed twice with water and ethanol, after which they were allowed to air dry at room temperature. Yield 26%.

Elemental analyses were conducted on Eu and Tb samples by Galbraith Laboratories, Inc., Knoxville, TN, USA. Eu: calcd. C 30.08, H 1.47; found C 30.06, H 1.50. Tb: calcd. C 29.65, H 1.45; found C 28.82, H 1.40.

3.1.2 Structural Description

The following structural description will focus specifically on that of the Eu analog. The Tb CP was found to be isostructural, as confirmed with single and powder X-ray diffraction studies.

Table 2. Crystallographic information for *Eu* and *Tb* FDC-CPs.

Formula	[Eu(C ₆ H ₂ O ₅)(C ₆ H ₃ O ₅)(H ₂ O)] _n	[Tb(C ₆ H ₂ O ₅)(C ₆ H ₃ O ₅)(H ₂ O)] _n
Formula weight (g/mol)	479.15	486.11
Crystal class	Orthorhombic	Orthorhombic
Space group	<i>Pbca</i>	<i>Pbca</i>
a (Å)	15.122(2)	15.0789(15)
b (Å)	9.3656(14)	9.2997(9)
c (Å)	20.290(3)	20.287(2)
α (°)	90	90
β (°)	90	90
γ (°)	90	90
Z	8	8
Cell volume (Å ³)	2873.7(8)	2844.8(5)
Density (mg m ⁻³)	1.933	2.270
μ (mm ⁻¹)	4.354	7.452
R_{int}	0.0518	0.0601
R₁	0.0237	0.0298
wR₂	0.0608	0.0577
GOF	0.715	1.028
Total Reflections	30,125	31,725

$$R_1 = \sum \frac{||F_o| - |F_c||}{|F_o|}; wR_2 = \left(\frac{\sum [w(F_o^2 - F_c^2)^2]}{\sum [w(F_o^2)^2]} \right)^{\frac{1}{2}}$$

The material is a two-dimensional compound constructed from EuO₈ polyhedra that form a distorted square antiprism coordination geometry, which edge share to form a dimeric secondary building unit (Figure 11, Figure 12, and Figure 13). Surrounding each Eu, there are five monodentate oxygen atoms, which belong to carboxylate moieties (O1, O3, O4, O7, O8), two symmetry equivalent oxygen atoms (O2, O2') bridging the Eu ions to form the dimer, and one bound aqua ligand (O9). Selected bond lengths and angles can be found in Table 3.

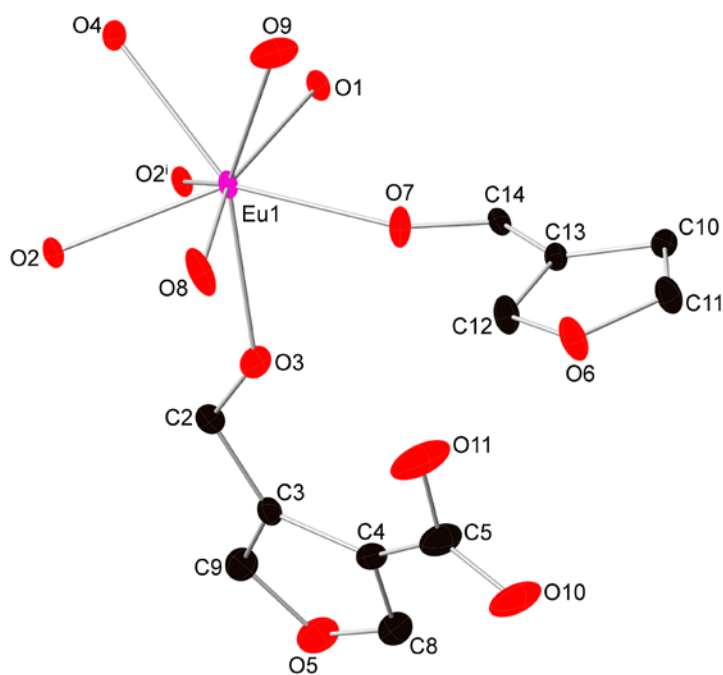


Figure 11. *Thermal ellipsoid plots (50% level) of all crystallographically unique atoms in Eu-FDC CP (where i indicates the symmetry operator $-x, -y, -z$). Hydrogen atoms have been omitted.*

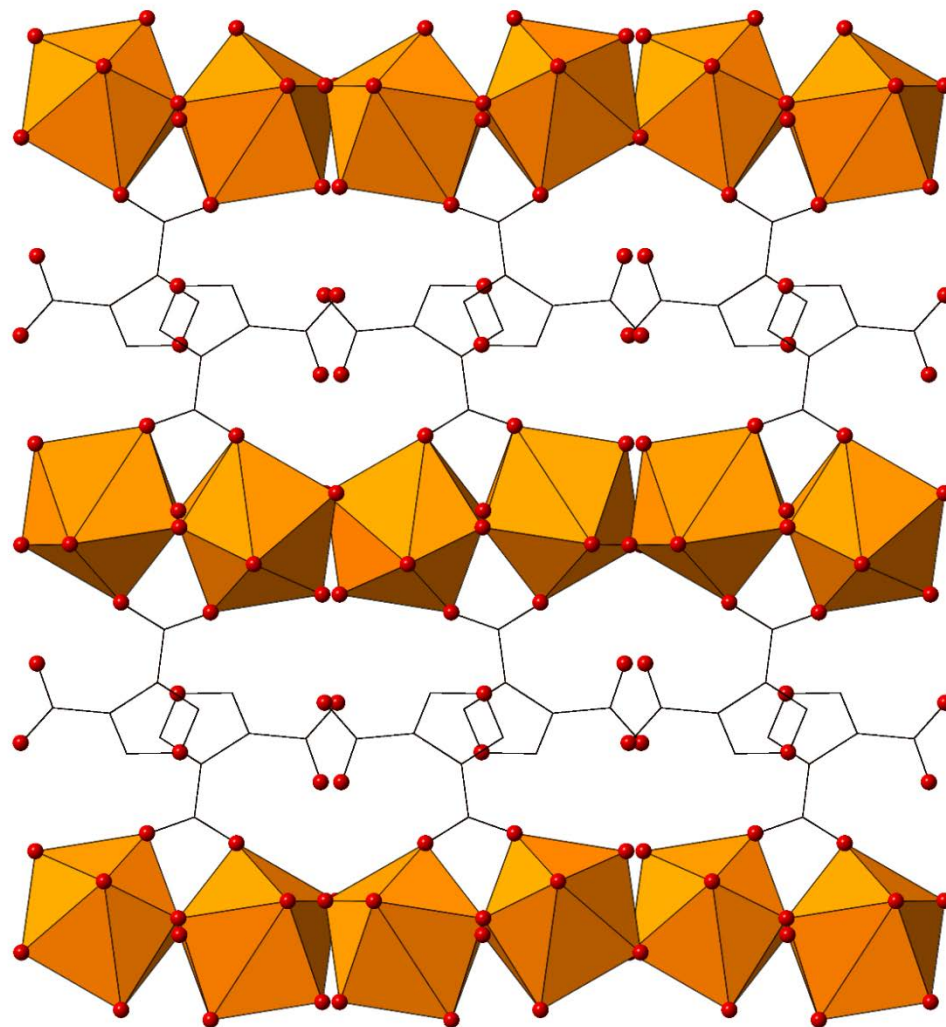


Figure 12. View of $[Eu(C_6H_2O_5)(C_6H_3O_5)(H_2O)]_n$ down $[010]$, showing the stacking of the layers. Note the uncoordinated FDC ion between the layers. Orange polyhedra represent EuO_8 units, black lines are carbon, and red spheres are oxygen atoms. Hydrogens have been omitted for clarity.

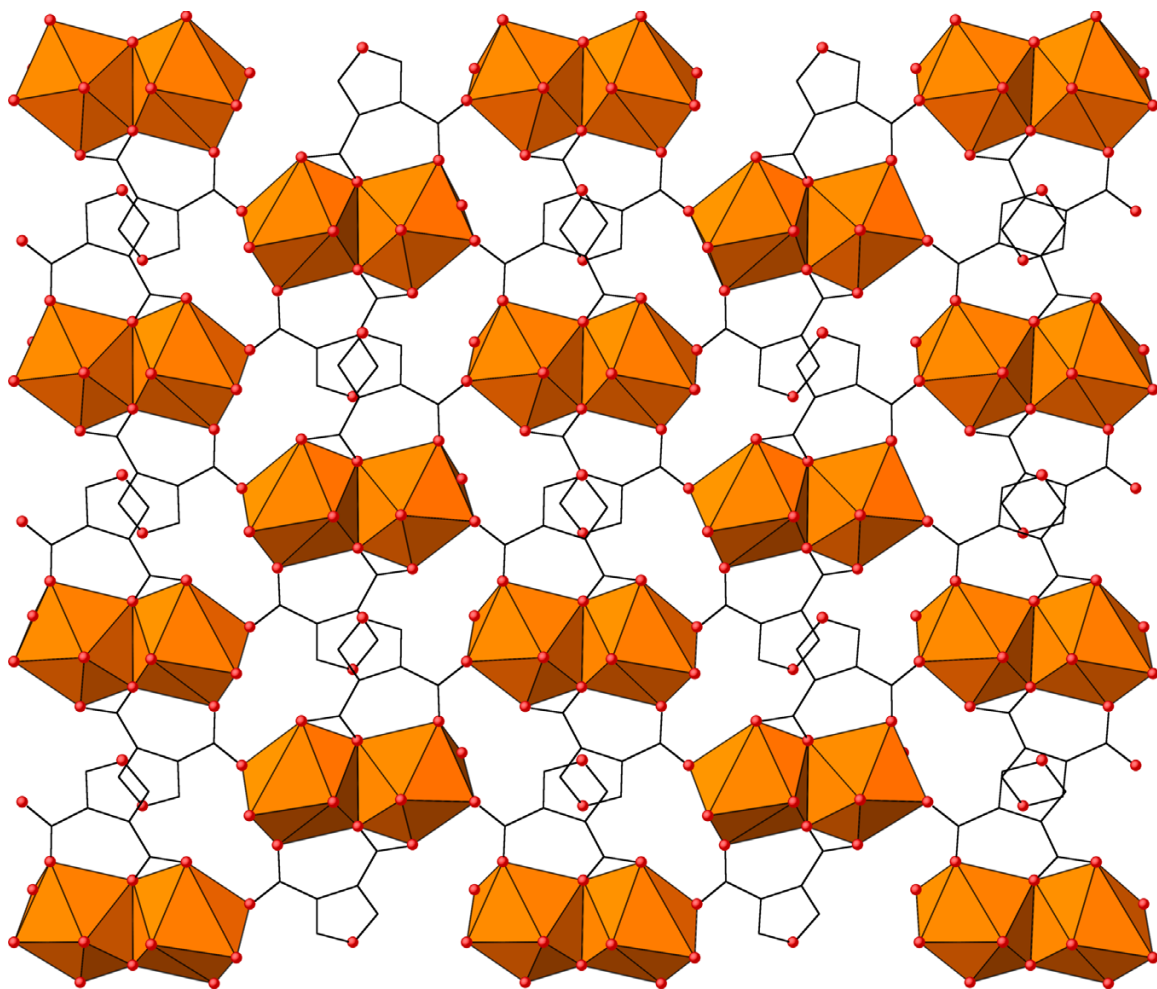


Figure 13. *The structure of an individual layer in the title compound, highlighting the dimer SBU structure. See Figure 12 for color scheme.*

Table 3. Selected bond lengths for Eu and Tb FDC CPs.

Eu-FDC		Tb-FDC	
Eu1-Ox		Tb1-Ox	
X	Å	X	Å
8	2.276(2)	8	2.249(3)
7	2.292(2)	7	2.261(3)
2	2.369(2)	2	2.349(3)
4	2.387(2)	4	2.356(3)
9	2.415(2)	9	2.391(3)
3	2.431(2)	3	2.405(3)
1	2.500(2)	1	2.482(3)
2 ⁱ	2.521(2)	2 ⁱ	2.486(3)
C5-O10	1.223(4)	C5-O10	1.225(6)
C5-O11	1.312(5)	C5-O11	1.324(6)

Superscript i=symmetry operator -x, -y, -z.

The Eu dimers form two-dimensional sheets that expand along the [100] and [010] directions (Figure 12), propagated by the organic linker. These sheets stack along [001] (Figure 13). Fully protonated carboxylic acid groups are found dangling between the sheets, with carbon oxygen bond distances of 1.223 Å (C=O) and 1.312 Å (C-OH) for O10 and O11, respectively. Hydrogen bonding and π - π interactions aid in the stacking of the sheets (Table 4).

Table 4. *Hydrogen bonding geometric parameters (Å, °).*

Interaction	D····A	D-H	H····A	Angle
O(9)-Hw(1)····O(1)	2.785(3)	0.96(5)	1.82(5)	178(4)
O(9)-Hw(2)····O(10)	2.748(4)	0.88(4)	1.88(4)	173(4)
O(11)-H(10)····O(3)	2.596(4)	0.82	1.78	176
C(8)-H(8)····O(1)	3.241(4)	0.93	2.56	131
C(9)-H(9)····O(10)	3.158(4)	0.93	2.26	162
C(11)-H(11)····O(9)	3.442(4)	0.93	2.57	157

Two crystallographically unique FDC linkers are present in this coordination polymer. The first FDC coordinates to both lanthanides of the dimer and provides one oxygen to each lanthanide center in a monodentate fashion from only one of its carboxylate moieties, O3 and O4. This coordination is paralleled by a symmetrically equivalent FDC ligand at an angle of 134.04°. The remaining carboxylate moiety of this FDC remains uncoordinated and protonated, and lies in between and nearly orthogonal to the sheets. The second FDC linker acts to propagate the sheets and is entirely chelated to the lanthanides through carboxylate oxygen atoms. Bridging the two lanthanide ions of the dimer is a bidentate oxygen atom, O2, of a carboxylate group. The remaining oxygen of this carboxylate group, O1, is coordinated to one Eu, while the other dimer receives coordination through O1' with a symmetrically equivalent linker on the opposite side of the dimer, along with a bridging oxygen atom, O2', repeated on the other side from another FDC. The second carboxylate group of this linker connects two neighboring dimer groups, with O8 bonding to a Eu of one dimer, and O7 coordinated to a Eu of the next nearest dimer. The last coordinated oxygen atom from the bound water, O9, is in

roughly the same plane as O2 and O3. Figure 14 shows a ball-and-stick representation highlighting the bonding around the lanthanide dimer.

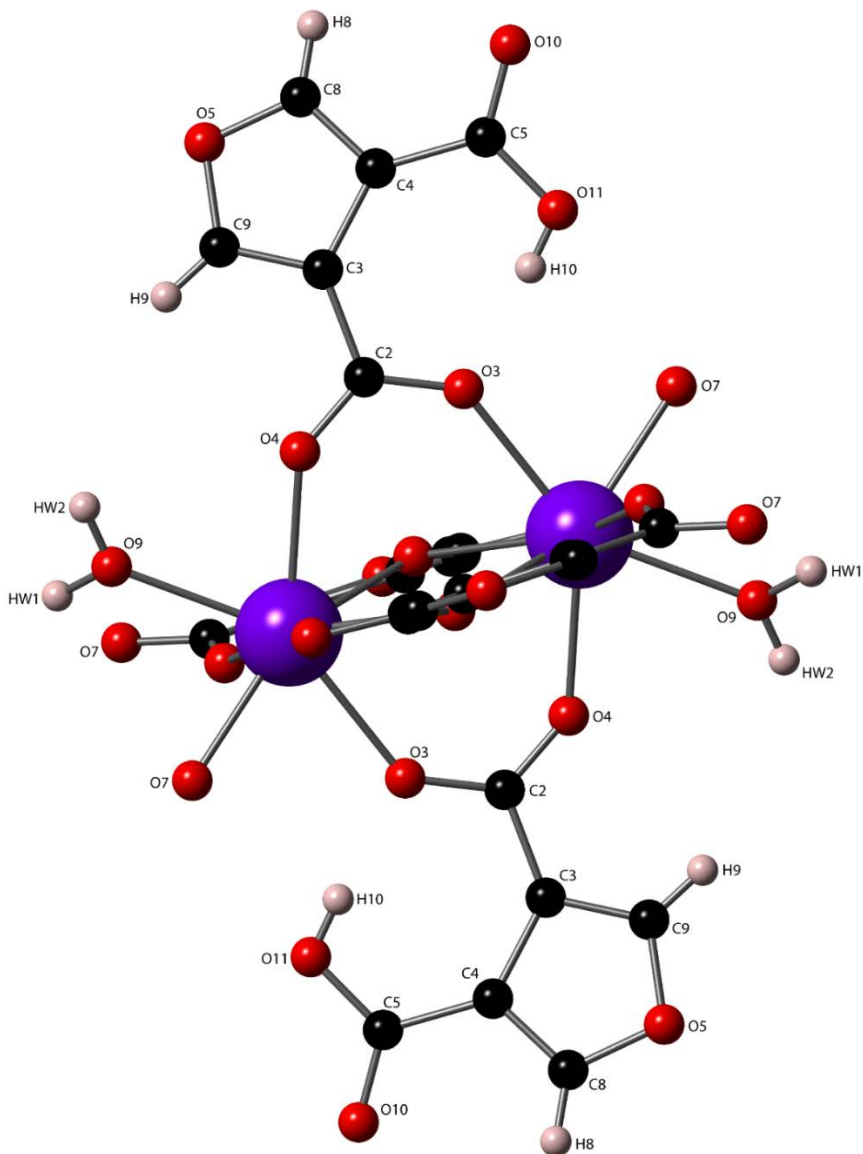


Figure 14. *Ball and stick representation of the lanthanide dimer. Carbon atoms are black, oxygen is red, hydrogen atoms are white, and the purple spheres are the lanthanide centers.*

Hydrogen bonding in the Eu-CP is shown (Table 4) and these interactions assist in the stacking of the sheets. First, there is a hydrogen bond between the bound water

ligand O(9) and O(1) of the fully deprotonated FDC ion that forms the dimer. The second interaction in the table is between O(10), which is a carboxylic acid moiety of one sheet dangling in the channel, and O(9), which is a bound aqua ligand of a dimer on a neighboring sheet. This interaction aids in stacking the sheets. The next interactions involve weaker C--Acceptor hydrogen bonds. There is a weak intersheet interaction between C(8)-H(8) of the dangling furan moiety of one sheet to a coordinated oxygen atom of a dimer in a neighboring sheet, O(1). There is another weak H-bond between C(9) and O(10), occurring in the channels and is between two furan moieties of different sheets, further aiding in the stacking of the sheets. Lastly, there is a weak intrasheet hydrogen bond between C(11)-H(11) and the coordinated aqua ligand, O(9).

There is a π - π interaction between two neighboring furan rings, centroid Cg(2)-Cg(2) (calculated using PLATON [85] where Cg = ring center of gravity values provide center to center distances) rings in which O6, C11, C10, C12, and C13 make up Cg(2). This interaction occurs at a distance of 3.560 Å, and is between two neighboring dimers within the sheet. A weak interaction between centroids Cg(1) and Cg(2), where Cg(1) is formed from the ring made up from atoms O5, C3, C4, C8, and C9. This intersheet interaction occurs at a distance of 4.014 Å and aids in the stacking of the sheets.

3.1.3 Photophysical Results and Analysis

Excitation and emission spectra were collected for both europium and terbium coordination polymers, and are seen in Figure 15 and Figure 16. The maximum excitation wavelength for both CPs is seen at 272 nm, attributed to FDC excitation.

Direct excitation of the Eu(III) ion can be observed from 340 to 500 nm with the 5L_6 level being the most intense. [86] Quantum yields, lifetimes were experimentally determined and molecular singlet and triplet energies were calculated from molecular modelling of FDC (Table 5).

Table 5. *Quantum yields and lifetimes of the Eu and Tb analogs of Ln-FDC.*

	Φ (%)	τ (ms)	1S (cm^{-1})	3T (cm^{-1})
Eu	1.1 ± 0.3	0.387 ± 0.0001	31,620	23,190
Tb	3.3 ± 0.8	0.769 ± 0.006		

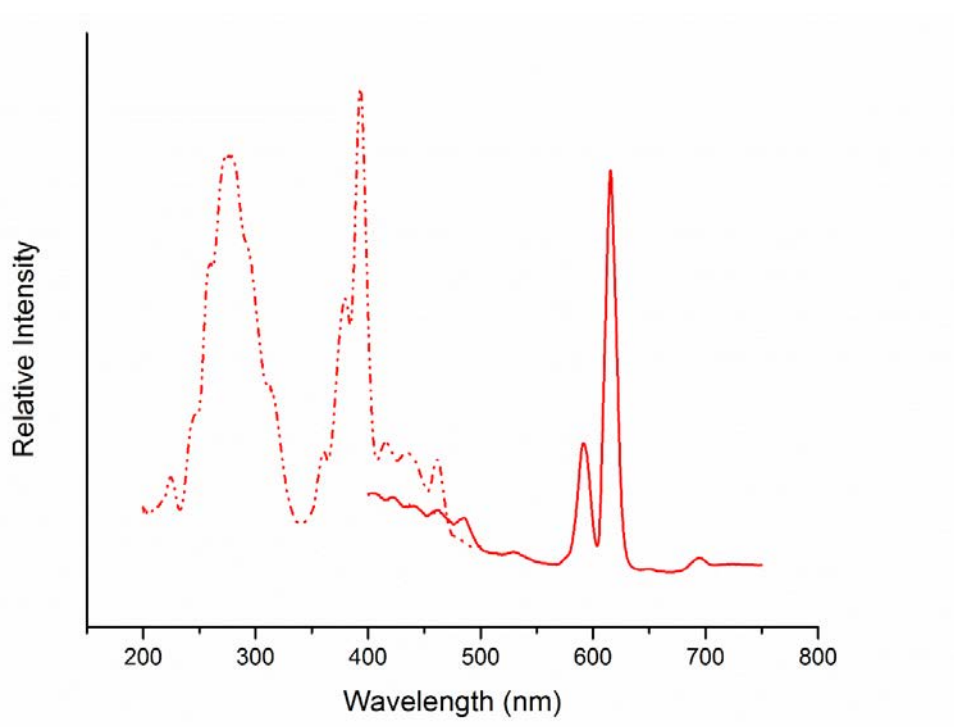


Figure 15. *Eu-FDC compound excitation (dashed) and emission (solid).*

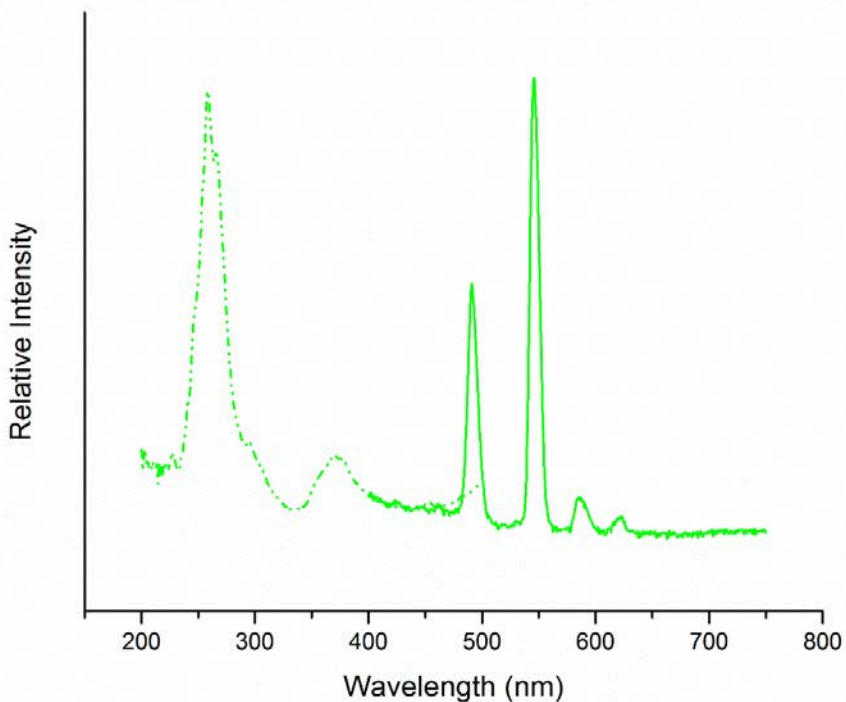


Figure 16. *Tb-FDC compound excitation (dashed) and emission (solid).*

The FDC linker's molecular triplet state of $23,190\text{ cm}^{-1}$ is most likely too high to promote efficient energy transfer to the $^5\text{D}_1$ level of the Eu(III) ion with an energy difference of $4,170\text{ cm}^{-1}$, just outside the optimum energy transfer range and too close to $^5\text{D}_2$ ($\Delta E = \sim 1,700\text{ cm}^{-1}$), resulting in a quantum yield of 1.1%. In the Tb system, the only energy level that could be occupied is the $^5\text{D}_4$ emissive level with an energy difference of $2,760\text{ cm}^{-1}$, which is within the range of optimum energy transfer and should promote decent quantum yields, but an efficiency of 3.3% was instead observed.

After integration of the emission spectrum for the Eu CP, sensitization efficiencies were obtained using the equations presented in a previous section (2.1.4). The results are shown in Table 6. These data indicate that aside from the poor quantum yield observed, the efficiency of the energy transfer from the FDC linker to the Eu(III) ion is poor, with an efficiency of only 14.6%, where some systems can have efficiencies

as high as 100%. [25, 87] The radiative decay values obtained from lifetime measurements and integrated emission spectra indicate that nonradiative processes ($2,395 \text{ s}^{-1}$) play a significantly large role in deactivating luminescence, with a value over 10 times higher than the radiative rate (188.67 s^{-1}), which may further explain the poor quantum yields seen in this system. These kinetic results, the poorly aligned triplet state of the linker, and presence of coordinated aqua ligands indicate that the FDC system has a myriad of shortcomings to be considered for further investigation as an efficient light harvesting material.

Table 6. *Luminescence parameters of the Eu FDC system.*

η_{sens}	Φ_{Eu}	τ_{rad}	k_{rad}	k_{nonrad}
14.6%	7.5%	0.0053 s	188.67 s^{-1}	$2,395 \text{ s}^{-1}$

3.2 2,3-Pyridinedicarboxylic Acid

The pyridine dicarboxylic acid family of linkers have been used previously in the construction of lanthanide-organic materials [88-105] due to the strong lanthanide coordination offered through oxygen and nitrogen donor atoms, and the delocalized aromatic system, which allowed the molecule to absorb energy to be transferred to the lanthanide ion. The most widely used pyridine dicarboxylic acid derivative is 2,6-pyridinedicarboxylic acid, and is used in coordination complexes as well as one-, two-, and three-dimensional coordination polymers with both transition metal and lanthanide ions. [96, 97, 106-111] The versatility of this linker arises from the tridentate nature of the molecule and the many coordination modes that it can adopt. [106, 112] There has been work on other pyridinedicarboxylic acid isomers including the 2,3-, 2,4-, 2,5-, 3,4-,

and 3,5- derivatives but the majority of this work has focused on transition metal coordination polymers. [113-122]

The 2,3-pyridinedicarboxylic acid is the least studied of these isomers and there is little work done utilizing this molecule and lanthanide ions. [101, 123-130] This could be due in part to the tendency of this linker to decarboxylate at the 2-position to become nicotinic acid under hydrothermal conditions. [131]

3.2.1 Synthesis

The coordination polymer $[\text{Ln}(\text{C}_7\text{H}_3\text{NO}_4)(\text{C}_7\text{H}_4\text{NO}_4)(\text{H}_2\text{O})]_n$ (Ln = Pr, Nd, Sm, Eu, and Tb) [132] was synthesized hydrothermally from a solution of europium chloride (EuCl_3 , 267 mg, 0.73 mmol) and 2,3-pyridinedicarboxylic acid ($\text{C}_7\text{H}_5\text{NO}_4$, 100 mg, 0.60 mmol) in 7 mL H_2O . The solution was placed in a 23 mL Teflon lined Parr bomb and heated under autogenous pressure for one day (24 h) at 120 °C. After cooling to room temperature, clear, colorless crystals were isolated from the supernatant liquid, washed twice with water and ethanol, and left to air dry at room temperature. Yield: 5 – 11%.

Elemental analyses were conducted on all samples by Galbraith Laboratories, Inc., Knoxville, TN, USA. Eu: calcd. C 33.53, H 1.81 N 5.59; found C 33.43, H 1.76, N 5.53. Pr: calcd. C 34.31, H 1.85, 5.72; found C 34.21, H 1.93, N 5.73. Nd: calcd. C 34.06, H 1.84, N 5.68; found C 33.97, H 1.81, N 5.61. Sm: calcd. C 33.64, H 1.82, N 5.61; found C 33.38, H 1.79, 5.64. Tb: calcd. C 30.07, H 1.79, N 5.51; found C 32.93, H 1.86, N 5.49.

3.2.2 Structural Description

Table 7. Crystallographic details for the Ln-PYDC compounds, $[Ln(C_7H_3NO_4)(C_7H_4NO_4)(H_2O)]_n$ (Ln = Pr, Nd, Sm, Eu, Tb).

Formula	Pr	Nd	Sm	Eu	Tb
Formula weight (g/mol)	490.14	493.47	499.59	501.19	508.15
Crystal class	Monoclinic	Monoclinic	Monoclinic	Monoclinic	Monoclinic
Space group	$P2_1/c$	$P2_1/c$	$P2_1/c$	$P2_1/c$	$P2_1/c$
a (Å)	12.8364(16)	12.8537(18)	12.8559(18)	12.8700(18)	12.856(8)
b (Å)	16.747(2)	16.731(2)	16.655(2)	16.645(2)	16.588(10)
c (Å)	7.0868(9)	7.0837(10)	7.0465(10)	7.0312(10)	6.988(4)
α (°)	90	90	90	90	90
β (°)	97.073(2)	97.170(2)	97.533(2)	97.687(2)	98.018(7)
γ (°)	90	90	90	90	90
Z	4	4	4	4	4
Cell volume (Å³)	1511.8(3)	1511.5(4)	1495.8(4)	1492.7(4)	1475.8(15)
Density (mg m⁻³)	2.154	2.170	2.219	2.231	2.288
μ (mm⁻¹)	3.272	3.493	3.984	4.270	4.851
R_{int}	0.0379	0.0409	0.0472	0.0862	0.1738
R₁	0.0434	0.0258	0.0262	0.0353	0.0718
wR₂	0.0955	0.0600	0.0583	0.0709	0.1720
GOF	0.953	1.058	1.030	1.012	0.975
Total Reflections	5683	22663	22092	16679	16278

$$R_1 = \sum \frac{||F_o| - |F_c||}{|F_o|}; wR_2 = \left(\frac{\sum [w(F_o^2 - F_c^2)^2]}{\sum [w(F_o^2)^2]} \right)^{\frac{1}{2}}$$

The coordination polymer $[Ln(C_7H_3NO_4)(C_7H_4NO_4)(H_2O)]_n$ (Ln = Pr, Nd, Sm, Eu, and Tb) was isostructural for all lanthanides, and only the Eu structure will be discussed in detail. The structure is comprised of EuO_7N_2 polyhedra that edge-share to form a zero-dimensional dimer. Each metal center is coordinated to four monodentate oxygen atoms (O1, O2, O5, O6), two symmetry equivalent oxygen atoms (O4) bridging the Eu ions (Eu1) and forming the dimer unit through carboxylate (O4) coordination.

Completing the coordination sphere are one coordinated aqua ligand (O3) and two bound nitrogen atoms (N1, N2). The Eu dimers extend in the [010] and [001] directions to form sheets (Figure 18) through coordination with the organic linker. The sheets stack along the [100] direction through hydrogen bonding (Table 9) between the carboxylic acid moieties of neighboring sheets (Figure 19). Within this carboxylic acid group, determination of the protonated oxygen atom (O8) was made based on bond lengths supported by bond valence calculations. [133-135] Here, oxygen atom O8 has a bond distance of 1.304 Å with the carbon atom C14, and a bond valence of 1.26 (approximately equal to the formal charge of a hydroxyl oxygen atom), but O9 has the shortest C-O distance (1.193 Å) of all carboxylate groups present, indicating the presence of a double bond with a bond valence of 1.70 for O9 (approaching the formal -2 charge of a carbonyl oxygen atom). This indicates that the O8-C14-O9 fragment is protonated as a carboxylic acid. The other carboxylate (containing O6 and O7) has bond lengths slightly longer than O9 (1.226 and 1.256 Å), caused by delocalization of the -1 charge of the deprotonated acid between the two atoms. The bound water ligand, O3 (2.355 Å) assists in the construction of the compound through hydrogen bonding. Within the dimer itself, O3 bridges the two metal centers through hydrogen bonding with O4 on the companion lanthanide (D-A distance 2.677 Å). There is also hydrogen bonding between neighboring dimer units between O3 on one dimer and O6 on a neighboring dimer (D-A distance 2.683 Å). Additionally, there is π stacking present between the PYDC linkers containing N1 at a distance of 3.554 Å. The PYDC linkers containing N2 are greater than 5 Å apart and consequently do not interact through π stacking.

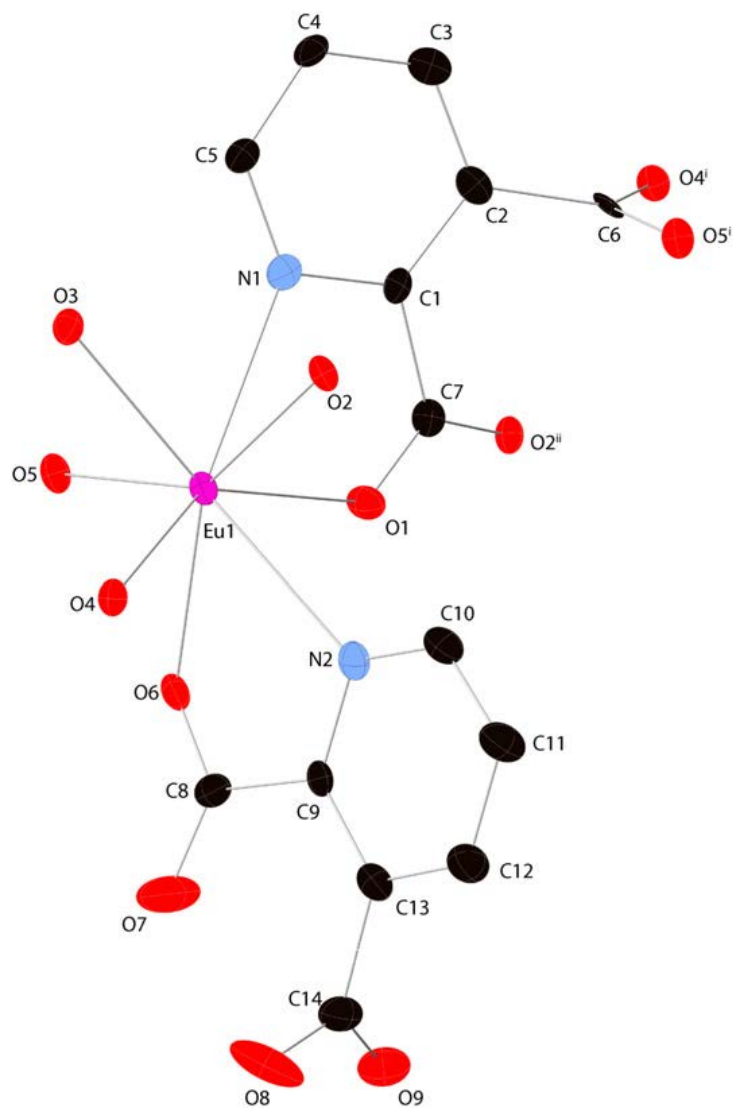


Figure 17. A thermal ellipsoid plot for the title compound shown at the 50% probability level. Hydrogen atoms are omitted.

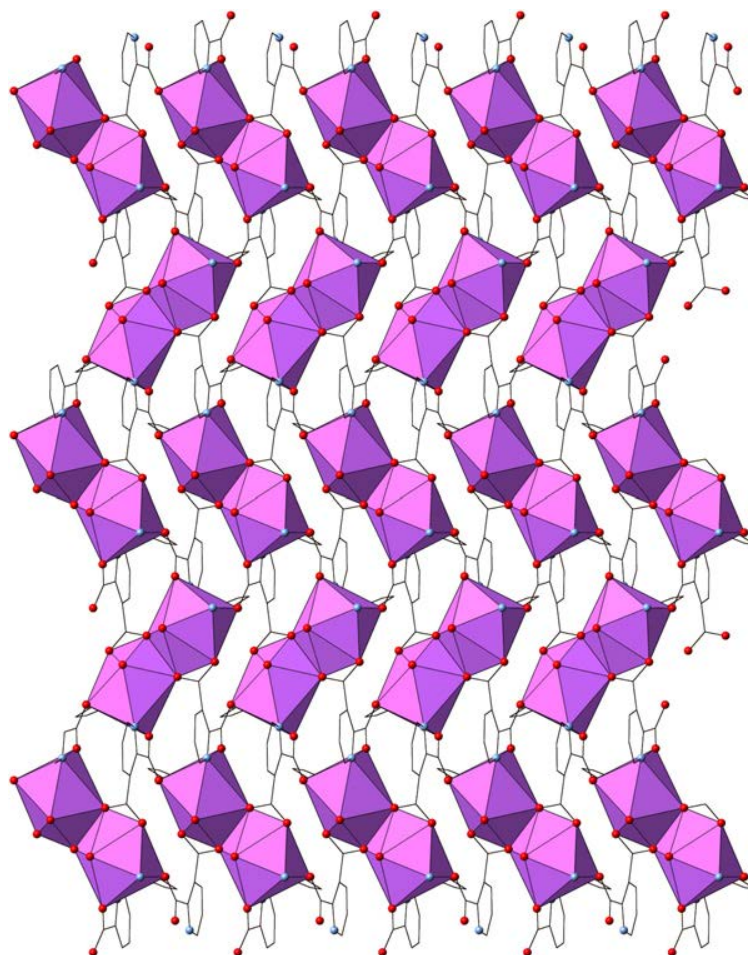


Figure 18. *Polyhedral representation of the sheets in the Ln-PYDC compound, highlighting the dimers.*

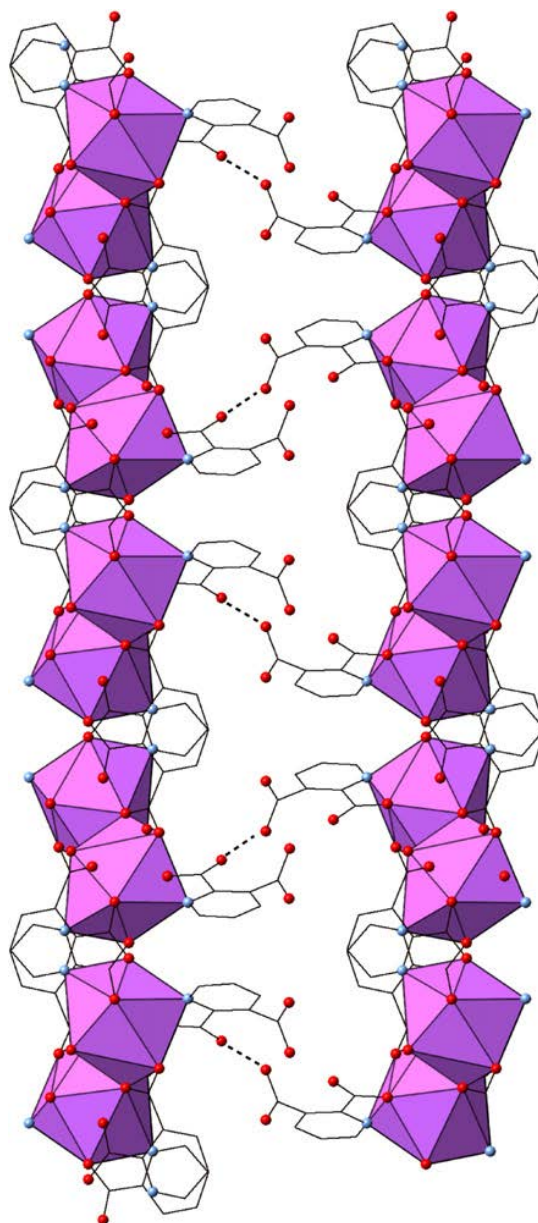


Figure 19. View of the Ln-PYDC compound down [001] where the hydrogen bonding (dashed lines) that connect the 2-D sheets down the [100] direction is shown.

Table 8. Selected bond lengths (Å) and angles (°) for the Eu-PYDC compound.

Eu-N1	2.746(3)
Eu-N2	2.654(5)
Eu-O4	2.379(3)
Eu-O4 ⁱ	2.809(3)
Eu-O3	2.355(4)
O1-C7	1.265(7)
O2-C7	1.248(7)
O4-C6	1.259(6)
O5-C6	1.270(6)
O6-C8	1.256(7)
O7-C8	1.226(7)
O8-C14	1.304(6)
O9-C14	1.193(9)
O1-C7-O2	125.48
O4-C6-O5	120.78
O6-C8-O7	124.87
O8-C14-O9	125.33

Superscript i=symmetry operator 1 - x, -1/2 + y, 1/2 - z.

There are two crystallographically distinct PYDC ions in this compound. The first, containing N1, serves to link the Eu dimers into a two-dimensional sheet. In order to do so, the carboxylate groups contort themselves about the pyridine ring (Figure 17). One carboxylate lies just outside the ring plane with torsion angles of 17.34° (C2-C1-C7-O2) and 17.21° (N1-C1-C7-O1). The second carboxylate orients itself in a fashion roughly perpendicular to the pyridine rings and serves in part to connect the dimers. Here, the torsion angles are 74.54 and 70.43° (C3-C2-C6-O5 and C1-C2-C6-O4, respectively). The second PYDC tethers the sheets together through hydrogen bonding to bridge Eu centers into dimers, as well as connect the dimers into a two-dimensional sheet.

Here, the two carboxylic acid groups are similar to the first linker, but now nearly orthogonal to one another. One carboxylate group is in plane with the pyridine ring (N2-C9-C8-O6, 6.62° and C13-C9-C8O7, 5.34°) and the protonated carboxylic acid group is nearly at a right angle to the ring (C9-C-13-C14-O9, 84.15° and C9-C13-C14-O8, 100.82°). Upon examination of the PYDC linker, it would seem plausible to form a one-dimensional material through the carboxylic acids, but upon coordination of the nitrogen of the pyridine coupled with the free rotation of the carboxylic acid groups has prompted the formation of a two-dimensional compound.

Table 9. *Hydrogen bond parameters for Eu-PYDC system.*

Interaction	D····A	D-H	H····A	Angle
O(8)····O(7)	2.626(2)	0.82	1.82	169
O(3)····O(4)	2.683(4)	0.81	1.89	165
O(3)····O(6)	2.677(1)	0.81	1.88	168

3.2.3 Photophysical Results and Analysis

Europium and terbium samples were excited between 200 to 400 nm to determine maximum excitation wavelengths while monitoring their emission. The Tb system exhibited a maximum emission wavelength at 546 nm and Eu at 620 nm under an excitation wavelength of 291 and 289 nm, respectively. The excitation spectra for each lanthanide correspond to absorption by the linker, after which energy is transferred to the lanthanide ion. These compounds both show emission attributed to the linker below 450 nm, indicating an inefficient sensitization pathway as supported by quantum yields, lifetimes, and decay rates data.

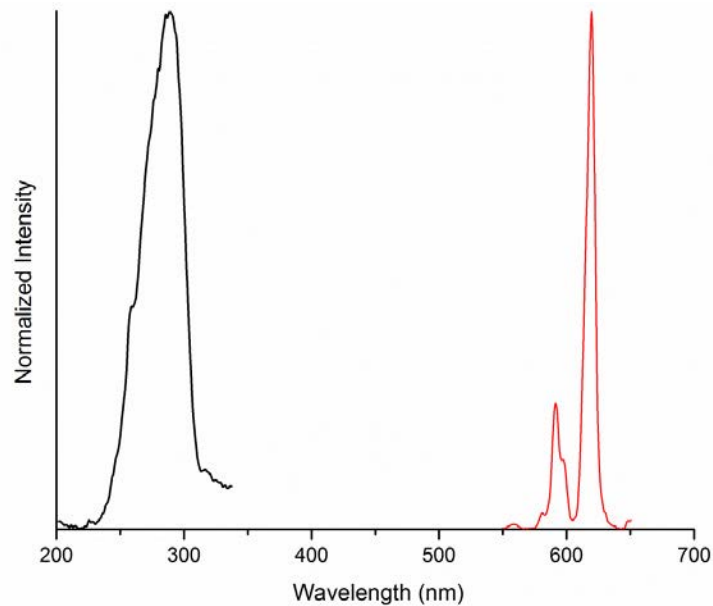


Figure 20. *Excitation (left) and emission (right) spectra of Eu-PYDC.*

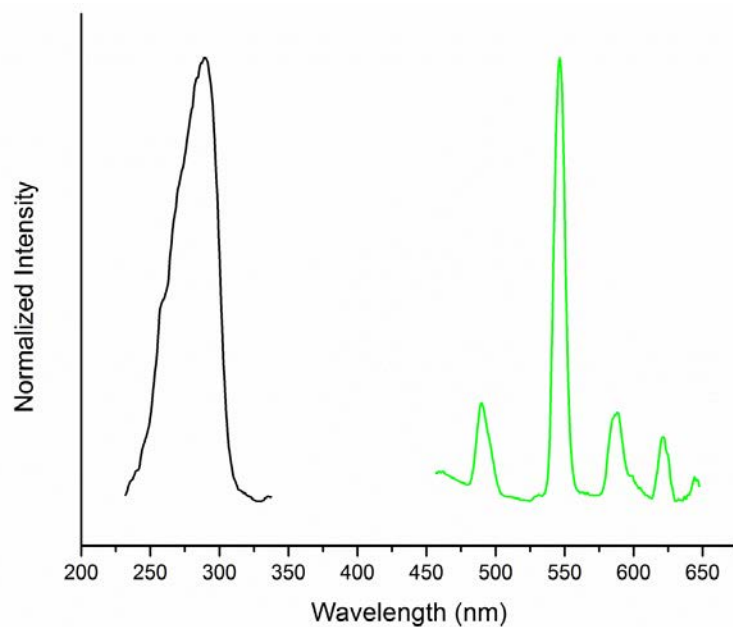


Figure 21. *Excitation (left) and emission (right) spectra of Tb-PYDC.*

Table 10. *Quantum yields and lifetimes of the Eu and Tb analogs of Ln-PYDC.*

	Φ (%)	τ (ms)	1S (cm^{-1})	3T (cm^{-1})
Eu	2.6 ± 0.28	0.53 ± 0.01	32,790	25,970
Tb	4.6 ± 0.18	1.21 ± 0.10		

From the quantum yield, lifetime, and integrated emission spectrum of the europium system, luminescence parameters for the PYDC system are underwhelming (Table 11). The efficiency of energy transfer from the PYDC linker to Eu(III) ion is 25.2%, indicating that this linker is not well suited for the emissive manifold of the Eu(III) ion. Furthermore, the nonradiative processes ($1,708 \text{ s}^{-1}$) are close to ten times higher than radiative processes in this system (178.57 s^{-1}), suggesting the coordinated aqua ligands and other nonradiative processes dominate energy deactivation processes.

Table 11. *Luminescence parameters of the Eu PYDC system.*

η_{sens}	Φ_{Eu}	τ_{rad}	K_{rad}	K_{nonrad}
25.2%	10.3%	0.0056 s	178.57 s^{-1}	$1,708 \text{ s}^{-1}$

3.3 Furan and Pyridine Systems within the Antenna Effect

The triplet state of the PYDC linker at $25,970 \text{ cm}^{-1}$ is close in energy with higher excited state levels (5D_3 , 5L_6) of the Eu(III) ion, yet too far from 5D_2 to resonate with this level. This would result in no appropriately suited energy manifolds in Eu for efficient energy transfer, explaining the low quantum yield. In the Tb system, the energy gap between 5D_4 and the linker's triplet state is greater than $5,000 \text{ cm}^{-1}$, which can also effectively explain the poor QY of 4.6%. Both systems have poor energy transfer from the absorbing organic species to the lanthanide ion (14.6% in FDC and 25.2% in PYDC), and the nonradiative processes dominate over radiative modes, suggesting the

coordinated aqua ligand in each system (two OH oscillations) and other nonradiative processes effectively deactivates a large portion of the energy in the system.

3.4 Conclusion

In conclusion, these two systems are quite unremarkable in their luminescence; however, they lay the groundwork for studying the antenna effect with model systems that follow the established guidelines.

CHAPTER 4: 4,4'-BENZOPHENONEDICARBOXYLIC ACID SYSTEM 4.1

BENZOPHENONE-4,4'-DICARBOXYLIC ACID

The linker chosen for the next study, benzophenone-4,4'-dicarboxylic acid (BPDC), was selected because it meets criteria that would make it a suitable candidate to be an efficient organic antenna. This molecule has a large, delocalized π system, and chelating carboxylic acid functional groups. Other groups have used this linker in transition metal systems [136-142], lanthanide systems with coligands such as phenanthroline [143, 144], and even in actinide systems. [145] TD-DFT modeling data suggested that the triplet state of BPDC should be well suited for energy transfer to the Tb(III) ion's 5D_4 emissive state. Finally, this linker was used in previous contributions [145] as well as a structurally similar linker, 4,4'-oxybis(benzoic acid) (OBA), [146] which contains two benzoic acid groups bridged together at the para positions by an sp^3 ether oxygen rather than a carbonyl group as in BPDC. [147, 148] These above reasons led to the assumption that the BPDC linker should be a suitable candidate for sensitized emission in visible emitting Ln CP systems.

4.1.1 Synthesis

The title compound was synthesized by hydrothermal means. A mixture of $\text{Eu}(\text{NO}_3)_3 \cdot 5\text{H}_2\text{O}$ (115 mg, 0.27 mmol) and BPDC (100 mg, 0.37 mmol) were added to deionized water (5 mL) and placed in a 23 mL Teflon-lined stainless steel vessel. The vessel was heated at 200 °C for 24 h, 175 °C for 24 h, and then 150 °C for 24 h. The

vessel was then removed from heat and left to cool to room temperature where yellow crystals were collected and washed twice with water and ethanol. The terbium compound was synthesized and treated in an identical manner.

Elemental analyses were conducted on Eu and Tb samples by Galbraith Laboratories, Inc., Knoxville, TN, USA. Eu: calcd. C 53.32, H 3.28; found C 52.73, H 3.18. Tb: calcd. C 52.95, H 3.26; found C 52.66, H 3.02.

4.1.2 Structural Description

The Ln-CP (Ln = Eu(III), Gd(III), Tb(III)) was synthesized and its structure determined (Figure 22, Figure 23, Figure 24, Table 12). The Eu analog is described here as the Tb and Gd compounds did not produce crystals suitable for single XRD, but found to be isostructural based on powder XRD and elemental analysis. The structure is a two-dimensional compound comprised of EuO_8 monomers exhibiting square antiprismatic coordination geometry. Surrounding each Eu atom are three monodentate attachments from the BPDC linker's carboxylate oxygen atoms (O2, O3, O7), a bidentate attachment (O12, O13) from a carboxylate group, and three coordinated water molecules (O16, O17, O18).

The CP contains three crystallographically unique BPDC linkers. Each linker has one carboxylate group interacting with the Eu center. Only one BPDC linker bridges Eu monomers together (O2, O3) down the [001] direction. The second unique BPDC ion has a carboxylate group attached in a bidentate fashion to the Eu center (O12, O13), while the third unique linker attaches in a monodentate fashion to the Eu center from the carboxylate group (O7), leaving carbonyl oxygen atom (O8) uncoordinated. The carboxylate groups not involved in coordination with Eu atoms form one-dimensional

channels with adjacent linkers through head-to-tail hydrogen bonding in the same geometric plane that propagates down the [010] direction.

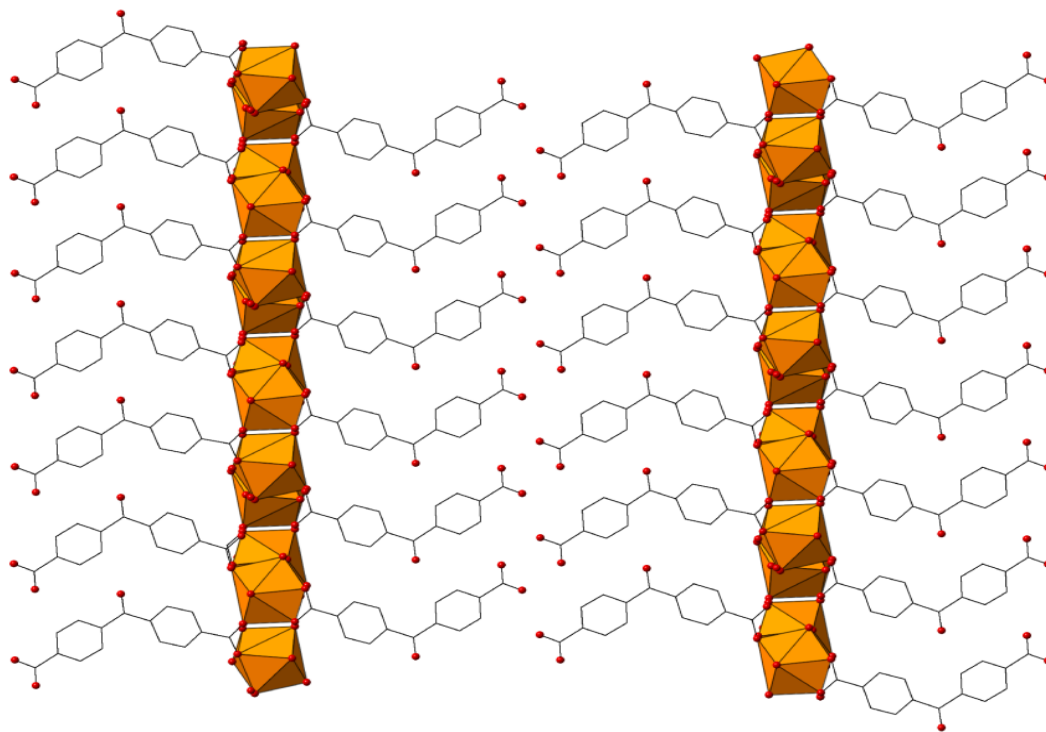


Figure 22. *Crystal structure of the Eu-BPDC compound down the [010] direction. Orange polyhedra represent Eu monomers, red spheres are oxygen atoms, and black lines are carbon atoms. Hydrogen atoms have been removed for clarity.*

Table 12. *Crystallographic information for the Eu-BPDC CP.*

Formula	[Eu(C₁₅H₉O₅)₃(H₂O)₃]_n
Formula weight (g/mol)	2009.20
Crystal class	Monoclinic
Space group	<i>P</i> 2 ₁ / <i>c</i>
a (Å)	27.981(2)
b (Å)	11.2983(8)
c (Å)	11.8755(9)
α (°)	90
β (°)	98.9390(10)
γ (°)	90
Z	4
Cell volume (Å³)	3708.7(5)
Density (mg m⁻³)	1.799
μ (mm⁻¹)	1.781
R_{int}	0.0916
R₁	0.0484
wR₂	0.1232
GOF	1.000
Total Reflections	8893

$$R_1 = \sum \frac{||F_0| - |F_c||}{|F_0|}; wR_2 = \left(\frac{\sum [w(F_0^2 - F_c^2)^2]}{\sum [w(F_0^2)^2]} \right)^{\frac{1}{2}}$$

Table 13. Selected bond lengths (Å) for the Eu-BPDC CP.

Eu-FDC	
Eu1-Ox	
X	Å
2	2.313(4)
7	2.378(4)
12	2.530(4)
13	2.508(3)
16	2.412(3)
17	2.371(4)
18	2.443(3)
38	2.897(5)
3 ⁱ	2.399(4)
C(8)-O(2)	1.267(6)
C(8)-O(3)	1.259(6)
C(15)-O(4)	1.294(6)
C(15)-O(5)	1.244(6)
C(23)-O(7)	1.268(6)
C(23)-O(8)	1.255(6)
C(30)-O(9)	1.242(7)
C(30)-O(10)	1.301(7)
C(38)-O(12)	1.266(6)
C(38)-O(13)	1.268(6)
C(45)-O(14)	1.241(7)
C(45)-O(15)	1.303(7)

Superscript i=symmetry operator 1-x, 1-y, -z.

Hydrogen bonding occurs within the compound between carboxylate groups from neighboring linkers lining the one-dimensional channel as well as from coordinated water ligands (Table 14). Carboxylate oxygen atoms (O4, O9, O10) interact with oxygen atoms on carboxylate moieties across the channel on neighboring linkers (O5, O15, O14) with

distances from 2.596 to 2.608 Å. The carbonyl oxygen atom (O8) interacts with a coordinated aqua ligand (O13) at a distance of 2.675 Å. One carboxylate oxygen atom (O13) forms a hydrogen bond with a coordinated water molecule at a distance of 2.708 Å. Several π - π interactions are also present within this compound with centroid distances ranging from 3.682 to 3.788 Å between neighboring linkers (Table 15).

Table 14. *Hydrogen bonding interactions and distances (Å) within the Eu-BPDC CP system.*

Interaction	D \cdots A
O(4) \cdots O(1)	2.608(5)
O(8) \cdots O(10)	2.675(5)
O(9) \cdots O(3)	2.596(5)
O(10) \cdots O(1)	2.598(5)
O(13) \cdots O(10)	2.708(5)

The twisting of the linkers allows for a closer packing distance between aromatic rings. The BPDC linkers are all slightly twisted with torsion angles between adjacent aromatic rings of 42.44°, 43.14°, and 46.70°. This allows for π - π interactions with adjacent linkers, which assist in facilitating the stacking of the Eu along the [001] direction. The aromatic rings have interaction distances from 3.682 to 3.788 Å with neighboring linkers.

Table 15. *π - π stacking interactions in the Eu-BPDC system.*

Interacting Carbons	Distance (Å)
O(4)····O(1)	3.682(3)
O(8)····O(10)	3.788(3)
O(9)····O(3)	3.778(3)
O(10)····O(1)	3.758(3)
O(13)····O(10)	3.764(3)

4.2 Photophysical Results

4.2.1 Excitation and Emission Spectra

Excitation and emission spectra were recorded at 298 K on a Jobin Yvon Fluorolog spectrometer. Emission spectra were collected with an excitation wavelength of 375 nm. The profile of the Eu system (Figure 25) is characteristic of the 5D_0 to 7F_J transitions (J=1-4) at 590, 616, 627, and 710 nm, respectively of Eu with no discernable organic emission. The excitation spectrum is largely linker based, but the sharp peak at 463 nm is from the direct excitation of the Eu(III) ion's $^5D_2 \leftarrow ^7F_0$ energy level. [86] Emission spectrum of the Tb system (Figure 26) is characteristic of Tb's 5D_4 to 7F_J transitions (J=6-3) at 491, 545, 587, and 623 nm.

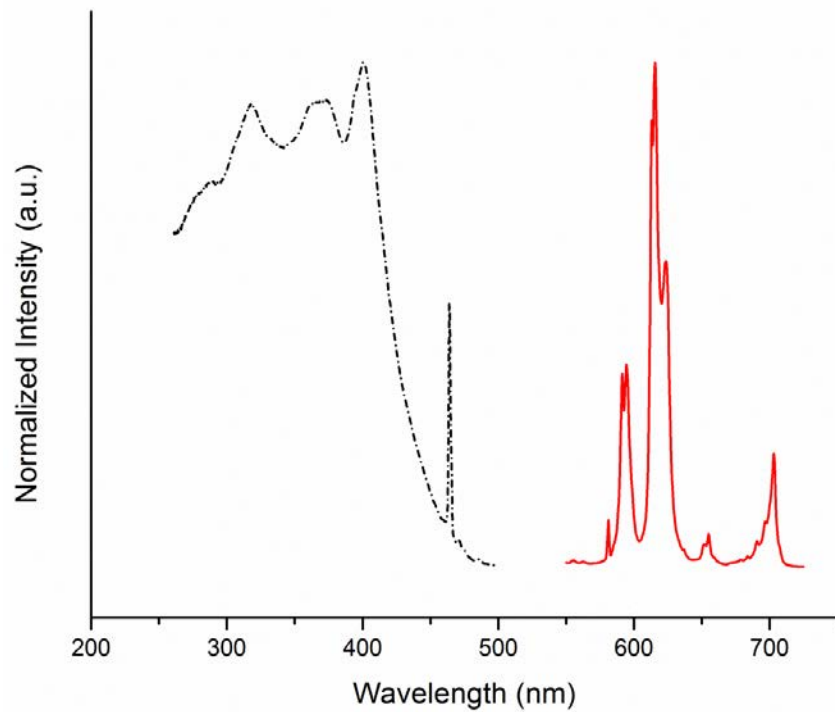


Figure 25. Excitation (black) and emission (red) spectrum of Eu-BPDC.

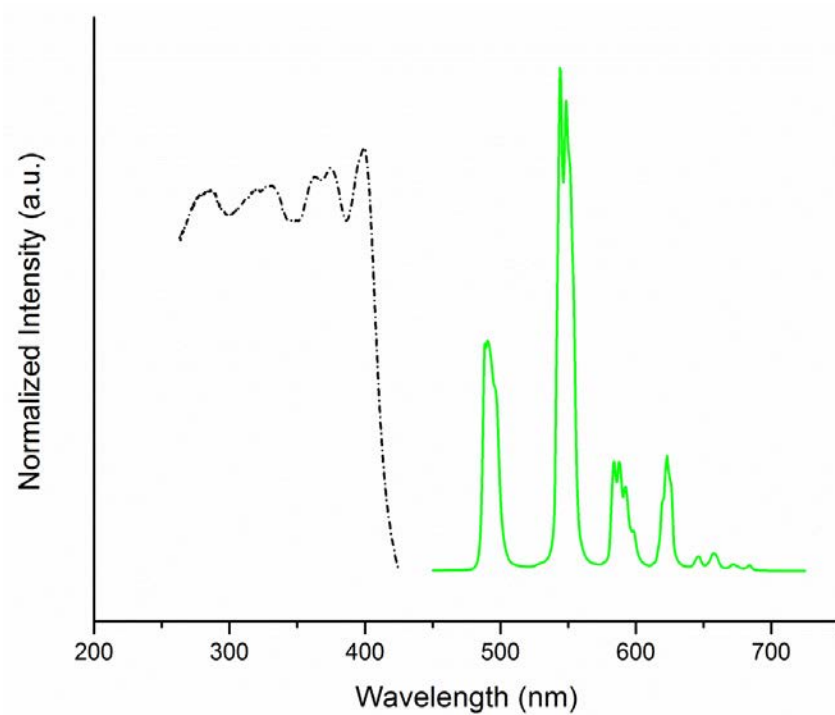


Figure 26. Excitation (black) and emission (green) spectrum of Tb-BPDC.

4.2.2 Analysis of Photophysical Data

Benzophenone-4,4'-dicarboxylic acid is responsible for sensitizing Ln emission in this system, and studying the molecular singlet and triplet states of this linker could provide insight into the efficiency or lack of efficiency within this system. Here, the triplet state of molecular BPDC ($23,420\text{ cm}^{-1}$) should be ideally suited for efficient energy transfer to Tb(III)'s 5D_4 manifold with an energy difference of $2,990\text{ cm}^{-1}$, yet ill-suited for Eu(III) ($\Delta E = 6,170\text{ cm}^{-1}$). This should result in a higher quantum yield for the Tb system than the Eu system. What is observed experimentally, however, is the opposite; BPDC is a good sensitizer for Eu(III) ($\Phi = 36\%$), but a poor sensitizer for Tb(III) ($\Phi = 6\%$). Additionally, the high Eu quantum yield was striking given the presence of these bound aqua ligands (six OH oscillators). To investigate these discrepancies, further studies were required.

4.3 Deuterated and Dehydrated Analogs

Investigations into the luminescence of lanthanide ions in complexes and CPs show that coordinated aqua ligands provide a route for quenching luminescence through a nonradiative decay pathway. Three to four OH quanta are sufficient to fill the energy gap between Eu and Tb's excited and ground states. [56, 71] By exchanging higher energy OH oscillators such as those found in water with weaker vibrational quanta from deuterium oxide, the amount of energy required to fill the energy gap increases to approximately six OD oscillators. Removing OH or OD oscillations altogether by dehydration of the compound can remove the NRD pathway attributed to these oscillators altogether to give further insight into the photophysical processes occurring within the system. To this end, deuterated and dehydrated analogs of the BPDC CP system were

synthesized to gain further insight into what energy transfer and photophysical processes are occurring.

4.3.1 Syntheses

Modified methods of the hydrated compound were employed to synthesize the deuterated and dehydrated materials. The starting Ln nitrate salt was dehydrated in a vacuum oven, water was substituted with deuterium oxide (5 mL), and the reaction vessel was flushed with and sealed under nitrogen for synthesis of the deuterated analogs. The yellow crystals were collected and washed with deuterium oxide and dried under a stream of nitrogen gas. The unmodified sample was placed in a vacuum oven at 250 °C under reduced pressure in 5 in. Hg to remove coordinated aqua ligands to produce the dehydrated sample. The Tb(III) and Gd(III) compounds were synthesized and treated in an identical manner. PXRD was used to confirm that no structural changes or loss of crystallinity occur during these treatments.

4.3.2 Excitation and Emission Spectra

Emission spectra for the Eu(III) and Tb(III) compounds were collected (Figure 27 and Figure 28) at 298 K on H₂O, D₂O, and dehydrated samples (equimolar concentrations collected during the same experiment after allowing the instrument to fully warm up) with an excitation wavelength of 375 nm. The profile of the Eu-BPDC compound is characteristic of ⁵D₀ to ⁷F_J transitions (J = 1 – 4) at 590, 616, 627, and 710 nm, respectively with no discernable organic emission. The dehydrated sample surprisingly displayed the lowest intensity emission and was further manifested in the quantum yields (Table 16). The emission spectra of the Tb-BPDC systems are characteristic of Tb's ⁵D₄ to ⁷F_J transitions at 291, 545, 587, and 623 nm, respectively, with the hydrated sample

displaying the lowest emission intensity as expected. The consequences of these observations will be addressed below in the discussion [86]

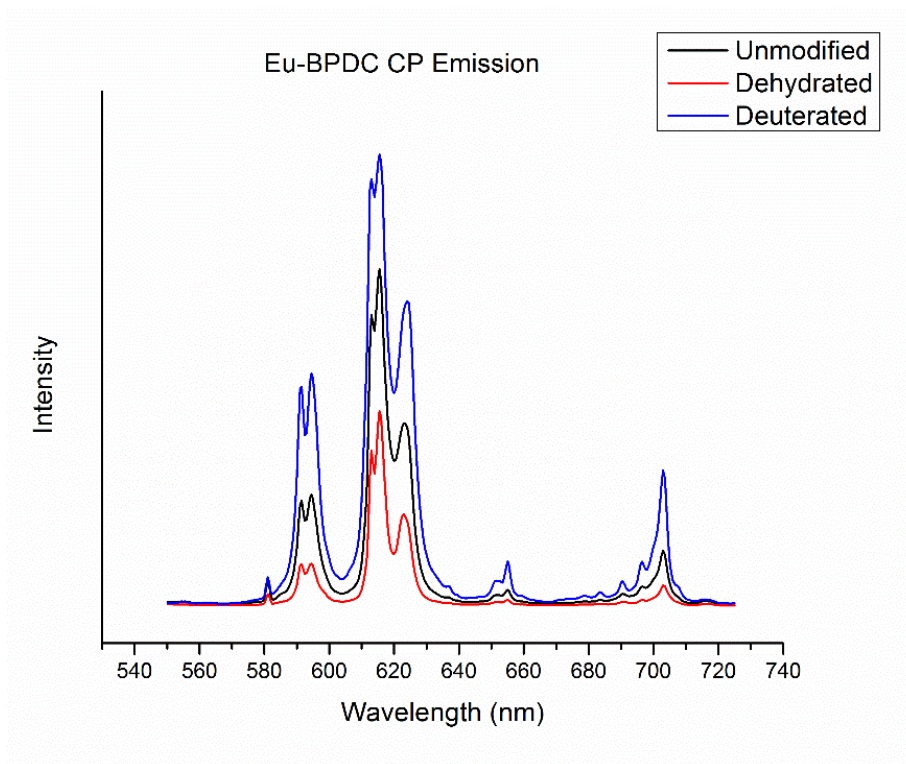


Figure 27. *Emission spectra of Eu-BPDC. Black spectra are for the unmodified, as-synthesized hydrated samples; blue spectra represent the emission for the deuterated analogues; red spectra represent the emission for the dehydrated analogs.*

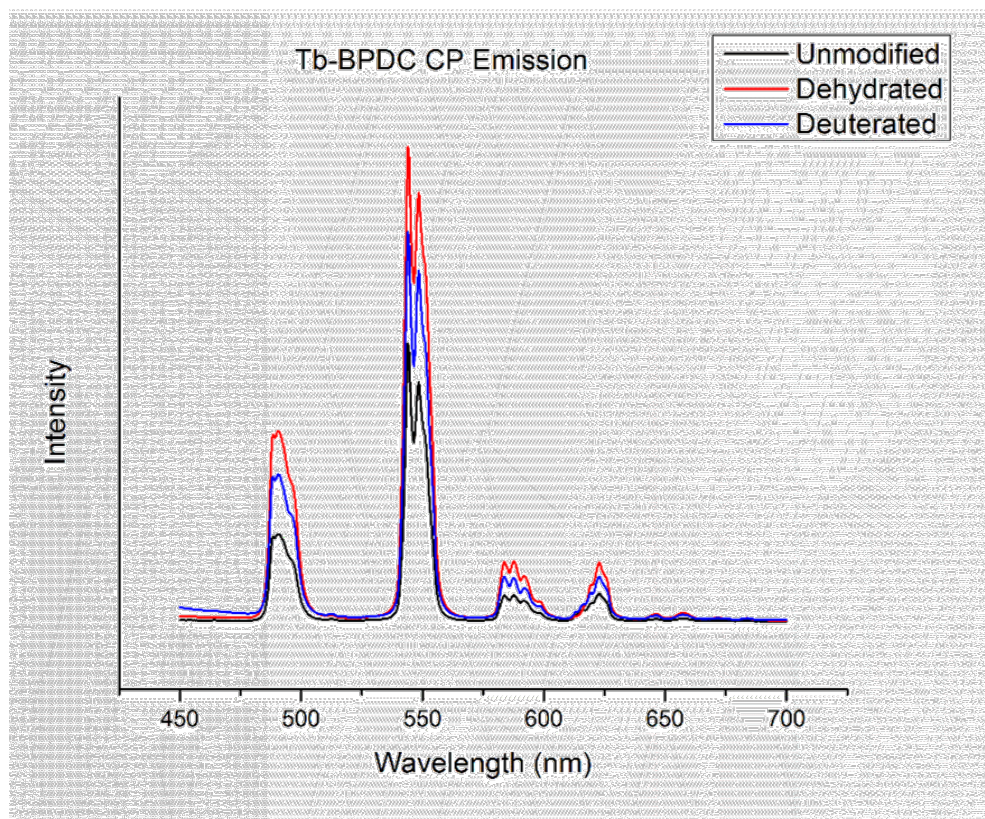


Figure 28. Emission spectra of Tb-BPDC. Black spectra are for the unmodified, as-synthesized hydrated samples; blue spectra represent the emission for the deuterated analogues; red spectra represent the emission for the dehydrated analogues.

4.3.3 Results and Discussion

While the triplet state of the molecular organic antenna has been widely used to describe lanthanide luminescence in coordination complexes, it may not be suitable for network solids such as MOFs and CPs. From inorganic network solids to amorphous organic semiconductors, the “infinite” nature of these structures results in band formation. It has been demonstrated that transition metal based MOFs and CPs produce bands, though the precise nature of these bands is an on-going area of research. [61-63] Regardless of their nature, the band structure of transition metal based CPs is likely a result of hybridization between inorganic and organic bands.

The situation is different in lanthanide CPs due to the unique character of the lanthanides, notably the valence f-orbitals being contracted toward the nucleus, with filled 5s/5p orbitals radially extended beyond the 4f orbitals. This would indicate that band formation in lanthanide CPs is likely to be predominately organic in nature. [149] As such, the linkers behave like organic semiconductors in which the spectroscopic properties of the lanthanide centers in CPs can be treated as dopants within this organic semiconducting matrix. [150] The current treatment of luminescence being described for CPs using the model based on molecular complexes is not suitable. Instead the band nature of the organic linker must be considered. It is proposed that charge recombination between singlet and triplet state bands of the conduction band and the valence band of the semiconducting organic results in an energy transfer to the lanthanide ion instead of radiative recombination, which will be discussed in Chapter 5.

To evaluate whether band or molecular sensitization is occurring, time-delayed emission studies of the Gd analog were conducted to determine the energy of the singlet and triplet bands within this system and compared to those obtained from molecular complexes. The singlet band lies at $23,040\text{ cm}^{-1}$ and the triplet band at $20,410\text{ cm}^{-1}$, significantly red-shifted from the singlet and triplet state energies of the BPDC molecular antenna (Table 16). If an energy difference greater than $5,000\text{ cm}^{-1}$ is needed for efficient ISC as is typically required in molecular systems, [151] then ISC is not likely efficient in this system. Emission studies support this since singlet band emission is observed even after long detector delays. This holds a specific consequence in that the sensitization from the singlet band will be proposed to partially explain the luminescence in this system. Do note that while singlet sensitization in complexes is not common, it may be

more common in lanthanide coordination polymers due to band structure, as will be discussed momentarily.

In resonant energy transfer, which occurs in sensitized Ln systems, there is a slight disparity between the energy of the donor and acceptor, where the acceptor is lower in energy. Assuming this energy difference is comparable to Ln complexes, [152] a difference of $\sim 2,500$ to $4,000\text{ cm}^{-1}$ should resonate well with this given f-excited state manifold.

In the europium system, the singlet band resides at $23,040\text{ cm}^{-1}$, which can allow BPDC to resonate with the 5D_1 of Eu(III) ($\Delta E = 4,020\text{ cm}^{-1}$), followed by internal conversion to 5D_0 before emitting to the ground state. The triplet band of the BPDC linker is able to resonate with the 5D_0 energy level ($\Delta E = 3,160\text{ cm}^{-1}$) with an overall quantum yield of 36% for Eu. This combination of singlet and triplet bands allows for energy transfer to both the 5D_1 and 5D_0 manifolds is believed to result in the quantum yield observed in the Eu system, and will be used to explain why luminescence is reduced in the dehydrated analog.

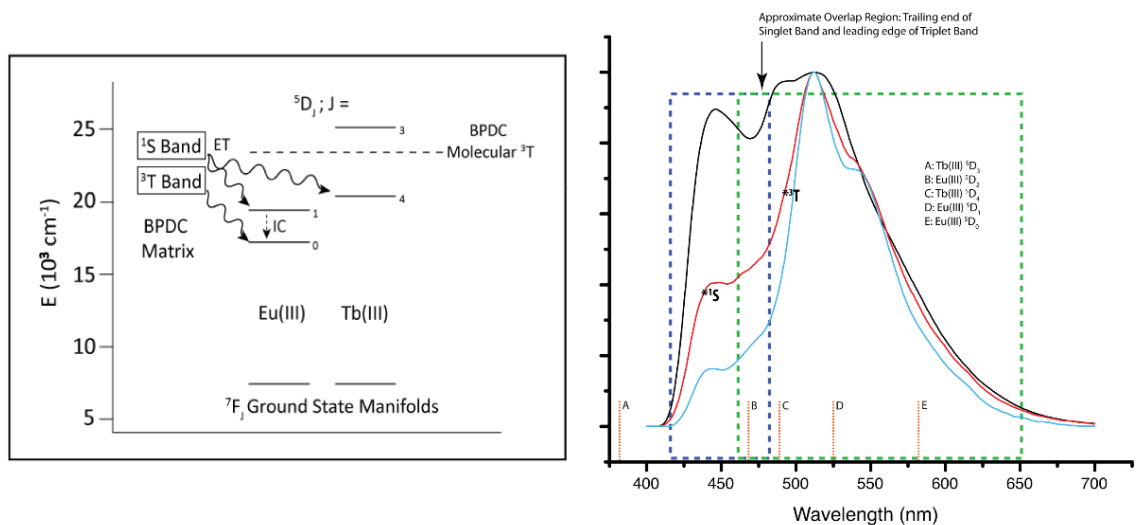


Figure 29. Analysis of the energy transfer mechanisms based on lowest lying singlet and triplet state values (left; molecular BPDC triplet state shown for reference as a dashed line) and that of donor/acceptor spectral overlap (right; emission spectra at 0.0, 0.3, and 0.5 ms delay with decreasing singlet state energy; singlet and triplet band levels noted * for reference on 0.3 ms delay spectrum).

For Tb, the triplet band lies too low in energy to transfer energy to Tb(III)'s emitting 5D_4 manifold. The singlet band, however, is ideally suited for energy transfer to this emitting level with an energy difference of $2,610 \text{ cm}^{-1}$. In molecular complexes, emission from the singlet to ground state is an allowed process, often happening faster than energy transfer can occur to the lanthanide ion. Due to the heavy atom effect from the lanthanide ion, intersystem crossing can compete with fluorescence to populate the triplet state, followed by energy transfer to the lanthanide ion. In networked solids and semiconductors, the situation increases in complexity with the inclusion of crystal momentum. For a more detailed explanation of this, see Section 5.2.3. The selection rule for crystal momentum states that a change in the momentum between two states is

forbidden. Even though fluorescence from the singlet state in a complex is allowed, emission from a singlet band in solids may not obey the momentum selection rule. This results in a longer lived singlet state, which may be long enough to transfer energy to the lanthanide. This pathway, although feasible in CPs may be less effective than sensitization by the triplet band. As such, singlet band sensitization of the emissive level of Tb(III) with nonradiative decay by the bound OH quanta is believed to result in the poor 6% quantum yield of Tb-BPDC.

These proposed energy transfer mechanisms in the Eu and Tb systems are based on a simplified qualitative assessment of the singlet/triplet band energies that is commonly used in lanthanide literature, which assumes that the lowest lying energy state is mostly involved in the ET process. Another analysis considers the entire spectral distribution of both the singlet and triplet bands where energy transfer occurs when there is overlap between the donor's (BPDC) emission spectrum and acceptor's (Ln ion) absorption spectrum. Using this, the singlet band covers $\sim 20,620$ to $23,810\text{ cm}^{-1}$ (420-485 nm) and the triplet band covers $\sim 15,380$ to $20,620\text{ cm}^{-1}$ (485-650 nm), though there is likely overlap of the two bands in the 475 to 490 nm region. Using these values, the 5D_2 manifold of Eu(III) lies within the singlet band, whereas 5D_1 and 5D_0 are too low in energy, but only the 5D_2 manifold could potentially be sensitized by the singlet band. The 5D_4 manifold of Tb(III) lies right at the interface between these two bands at $\sim 20,430\text{ cm}^{-1}$ (489 nm), but technically resides just inside the triplet band, though it is in the overlap region. Based on this, it could be argued that there is some triplet sensitization of Tb(III)'s 5D_4 manifold, though it would be difficult to conclusively distinguish since the singlet and triplet bands do overlap in this region.

Regardless of which method is used to deduce and describe the energy transfer mechanism that is occurring (the “classic” antenna description based on discrete singlet triplet values or that based on spectral overlap), it is clear that the sensitization by the band nature of the organic rather than its individual molecular structure is necessary when describing the luminescence of Ln CPs and MOFs. However, it should be stressed that the proposed “band model” is still considered to be the antenna effect, but sensitization occurs through a fundamentally different process involving the band nature of CPs and MOFs. This answers why Eu emission is higher than Tb, but does not address why Eu emission decreases in the dehydrated samples.

The presence of high-energy oscillators is commonly used to explain poor luminescence in Ln compounds, but their influence may not affect Ln CPs similarly due to structural attributes such as extensive hydrogen bonding networks and lack of dynamic ligand exchange. Luminescence in both the Eu and Tb systems improved in terms of emission quantum yields upon substituting H₂O with D₂O (Table 16). Upon replacement of the OH oscillators with OD, the excited state lifetimes of the Eu and Tb CPs increased as expected.

Additionally, using Horrock’s [153] and Choppin’s [154] equations (Table 17), the calculated number of bound aqua ligands matches within error those found in the crystal structure, indicating that these high-energy oscillators do indeed influence the f-excited state lifetimes within Ln-based CPs in a similar fashion to complexes. These equations were determined empirically from solution experiments, where in solid-state materials such as CPs the number of bound water molecules is precisely known from crystallographic data, thus providing empirical validation of these equations. This shows

that in these extended systems, while different, can still be assessed using these equations derived from solution studies.

In both complexes and CPs, such oscillators are detrimental to luminescence efficiency, as demonstrated by the increase of quantum yields upon OH to OD replacement. Yet, in the Eu system, the high-energy OH/OD oscillators appear to have an overall enhancement effect to the luminescence that exceeds their concurrent NR quenching effects since the OH/OD systems have higher quantum yields than the dehydrated (Table 16). It is postulated that the OH/OD oscillators assist with the IC from 5D_1 to 5D_0 since their energy difference is on the order of these oscillators. This has been observed in other systems upon dehydration, but were left unexplained by the authors. [26, 73] This could possibly explain these rare instances. It is uncertain if this phenomenon is (a) unique to singlet sensitization, (b) unique to energy transfer to 5D_1 only, (c) possible through triplet band sensitization also, or (d) possible with manifolds higher than 5D_1 .

Table 16. Photophysical measurements of Eu and Tb BPDC systems.

	Eu			Tb		
	H ₂ O	D ₂ O	Dehydrated	H ₂ O	D ₂ O	Dehydrated
Quantum Yield (%)	35.5 ± 4.9	58.8 ± 7.1	26.9 ± 3.1	6.0 ± 0.3	19.0 ± 1.5	26.1 ± 3.8
Lifetime (ms)	0.265 ± 0.016	0.906 ± 0.023	1.330 ± 0.039	0.280 ± 0.023	0.379 ± 0.030	0.613 ± 0.039
BPDC Linker		$^1S_{\text{molecule}} = 30,580 \text{ cm}^{-1}$ $^1S_{\text{band}} = 23,040 \text{ cm}^{-1}$			$^3T_{\text{molecule}} = 23,420 \text{ cm}^{-1}$ $^3T_{\text{band}} = 20,410 \text{ cm}^{-1}$	

Table 17. Bound water determination results for Eu- and Tb-BPDC.

	Eu	Tb
q	2.81 ^a	3.91 ^{a,c}
	3.26 ^b	

^aObtained using Horrock's equation, ^bObtained using Choppin's equation; there is currently no equivalent of Choppin's equation for Tb systems. ^cThe number of bound water molecules is within experimental error of the lifetime studies (approximately $\pm 1/2$ water molecule).

The emission spectra of the europium compounds can also provide important information regarding radiative (κ_{rad}) and non-radiative (κ_{nonrad}) rates within Ln-organic systems, which offers insights into the luminescence of the Ln ion. The intrinsic quantum yield of Eu(III) (Φ_{Eu}) can be determined, as well as the efficiency of the organic to sensitize Ln emission (η_{sens}), using the following equations. [73-75]

$$\Phi_{TOT} = \Phi_{Eu} \cdot \eta_{sens}$$

$$\Phi_{Eu} = \frac{\tau_{obs}}{\tau_{rad}}$$

$$\frac{1}{\tau_{rad}} = An^3 \left(\frac{I_{TOT}}{I_{MD}} \right)$$

$$\kappa_{nonrad} = \kappa_{obs} - \kappa_{rad} = \frac{1}{\tau_{obs}} - \frac{1}{\tau_{rad}}$$

Where Φ_{TOT} is the quantum yield of the system, τ_{obs} and τ_{rad} are the experimental and radiative lifetimes, respectively, A is the spontaneous emission probability of the 5D_0 to 7F_1 transition (14.65 s^{-1}), n is the refractive index (~ 1.5 for these solids), and $I_{TOT/MD}$ are the entire integrated Eu emission spectrum from 5D_0 to 7F_4 and the integrated magnetic-dipole emission band, $^5D_0 \rightarrow ^7F_1$.

Table 18. *Luminescence parameters of the hydrated, deuterated, and dehydrated Eu BPDC systems.*

Compound	η_{sens}	Φ_{Eu}	τ_{rad}	κ_{rad}	κ_{nonrad}
Hydrated	697%	5.1%	0.0052 s	193.67 s ⁻¹	3579.9 s ⁻¹
Deuterated	354%	16.6%	0.0055 s	183.13 s ⁻¹	920.6 s ⁻¹
Dehydrated	102%	26.4%	0.0050 s	198.60 s ⁻¹	553.5 s ⁻¹

From Table 18, it is seen that κ_{rad} values between the OH/OD/dehydrated compounds are all nearly identical, and that there is a steady decrease in κ_{nonrad} as the OH oscillator is replaced by OD and then removed altogether. This is expected as the NR decay mechanism becomes progressively less efficient, but when the η_{sens} is calculated, the values seem implausible for the OH and OD systems. When dehydrated, BPDC transfers its energy to the Eu center, causing what should be the maximum quantum yield feasible within this system. However equations calculating these values assume a correlation between κ_{nonrad} and η_{sens} . This neglects enhancement of the sensitization process by the very oscillators that simultaneously contribute to κ_{nonrad} . Thus, η_{sens} values in the OH and OD systems appear nonsensical at well above 100%. However, these values seem to be the combination of BPDC's intrinsic η_{sens} and the OH/OD oscillators' ability to enhance luminescence. Together, these data and experimental observations suggest that in certain situations, high energy oscillators like OH/OD may assist in the energy transfer processes, resulting in enhanced luminescence when compared to its dehydrated analog.

4.4 Conclusion

The Ln-BPDC system is a unique coordination polymer which led us to re-evaluate how we and others are studying lanthanide coordination polymer materials. The

photophysical results obtained were intriguing as both the misaligned triplet energy of the linker and number of coordinated aqua ligands should hinder sensitized luminescence. This study established the foundation for a new model on sensitized luminescence in these systems.

CHAPTER 5: THE BAND MODEL OF SENSITIZED LUMINESCENCE IN TRIVALENT LANTHANIDE COORDINATION POLYMER SYSTEMS

Since lanthanide coordination polymers are not molecular entities, but rather network solids, a new theory built upon the foundation of the antenna effect to explain Ln luminescence in CPs is needed. The periodic arrangement of the metal centers with organic linkers results in the formation of band features similar to insulators and semiconductors. [61-63] When Ln ions are incorporated into inorganic semiconducting materials, their luminescence is sensitized by charge carrier (exciton) recombination since there exists no organic antennae within these systems. Results from our BPDC studies (See Chapter 4) indicated that a similar mechanism occurs in Ln CP systems, and that modifying the antenna effect guidelines for these systems is necessary. [155] This new approach applies known characteristics of semiconducting organic solids to the antenna effect as derived from molecular systems, and represents an important advancement to the study of sensitized luminescence in Ln CP compounds.

Nine coordination polymers were synthesized from the literature with trivalent Eu, Gd, and Tb ions to test the validity of this modified approach to the antenna effect. Four CP systems were synthesized from the linker 1,4-benzenedicarboxylic acid, $[\text{Ln}_2(1,4\text{-BDC})_3(\text{DEF})_2(\text{EtOH})_2] \cdot 2(\text{DEF})$ (1) [156] (DEF=diethylformamide; EtOH=ethanol), $[\text{Ln}_2(1,4\text{-BDC})_3(\text{H}_2\text{O})_4]$ (2) [157], $[\text{Ln}_2(\text{OH})_4(1,4\text{-BDC})(\text{H}_2\text{O})_2]$ (3) [158],[158] and $[\text{Ln}_2(\text{OH})_4(1,4\text{-BDC})]$ (4). [158] Another CP systems was synthesized

with a 1,3-benzenedicarboxylic acid (1,3-BDC), ($[\text{Ln}_2(1,3\text{-BDC})_3(\text{H}_2\text{O})_2]$) (**5**). [159] A system with a highly efficient sensitizing linker with two aromatic rings bridged by an ether oxygen, 4,4'-oxybis(benzoic acid) (OBA), ($[\text{Ln}_2(\text{OBA})_3(\text{H}_2\text{O})_{5.5}\cdot 0.5\text{H}_2\text{O}]$) (**6**) [160] as well as three CPs previously reported by our group and $[\text{Ln}(\text{BPDC})_3(\text{H}_2\text{O})_3]$ (**7**) [155], $[\text{Ln}(\text{PYDC})(\text{HPYDC})(\text{H}_2\text{O})]$ (**8**) [132], and $[\text{Ln}(\text{FDC})(\text{HFDC})(\text{H}_2\text{O})]$ (**9**) [84], (BPDC=4,4'-benzophenonedicarboxylic acid, PYDC=2,3-pyridinedicarboxylic acid, and FDC=3,4-furandicarboxylic acid) were also chosen to test the validity of the band approach to the antenna effect within coordination polymers. The linkers for each CP studied had the energy of their singlet and triplet states determined from molecular complexes as well as the singlet and triplet bands of the CPs. Quantum yields and lifetimes were obtained for each CP (both Eu and Tb) and used to compare and contrast the two models. The luminescence of these compounds was easily rationalized using the proposed band model, whereas the molecular approach failed to adequately explain all systems.

5.1 Synthesis

*Synthesis of $[\text{Ln}_2(1,4\text{-BDC})_3(\text{DEF})_2(\text{EtOH})_2\cdot 2(\text{DEF})]$ (**1**)*

Compound **1** was synthesized through modified literature methods by combining $\text{Tb}(\text{NO}_3)_3\cdot 5\text{H}_2\text{O}$ (54 mg, 0.125 mmol) and H_2BDC (29 mg, 0.176 mmol) in a 23 mL vial with DEF (6 mL) and ethanol (1 mL). A small hole was made in the cap before covering the vial. The vial was placed inside a jar with ethanol (5 mL) and triethylamine (0.2 mL). The jar was sealed and vapor diffusion was allowed to occur for seven days (168 hours). The white crystalline solids were washed twice with water and ethanol and allowed to air dry.

Synthesis of [Ln₂(1,4-BDC)₃(H₂O)₄] (2)

Compound **2** was prepared by adding Tb(NO₃)₃·5H₂O (65 mg, 0.15 mmol) and H₂BDC (25 mg, 0.15 mmol) to water (9 mL) in a 23 mL Teflon-lined autoclave. Triethylamine (0.30 mL, 2.1 mmol) was added, turning the solution cloudy. The vessel was then sealed and heated at 140 °C for 12 hours. The autoclave was then removed and left to naturally cool down. The white crystalline solids were decanted from the white, cloudy supernatant and washed twice with water and ethanol, after which the crystals were allowed to dry.

Synthesis of [Ln₂(OH)₄(1,4-BDC)(H₂O)₂] (3)

An aqueous solution (8.7 mL) of Tb(NO₃)₃·5H₂O (545 mg, 1.20 mmol) and H₂BDC (100 mg, 0.60 mmol), NaOH (96 mg, 2.40 mmol) was added to a Teflon-lined autoclave. The vessel was sealed and placed in an oven at 180 °C for 4 days (96 hours). The white crystalline solids were decanted from the white, cloudy supernatant and washed twice with water and ethanol. The solids were left to air dry.

Synthesis of [Ln₂(OH)₄(1,4-BDC)] (4)

To an aqueous solution (8.7 mL) of Tb(NO₃)₃·5H₂O (545 mg, 1.20 mmol) and H₂BDC (100 mg, 0.60 mmol), NaOH (96 mg, 2.40 mmol) was added to a Teflon-lined autoclave. The vessel was sealed and placed in an oven at 250 °C for 4 days (96 hours). The white crystalline solids were decanted from the white, cloudy supernatant and washed twice with water and ethanol. The solids were left to air dry.

Synthesis of [Ln₂(1,3-BDC)₃(H₂O)₂] (5)

An aqueous mixture of Eu₂O₃ (176 mg, 0.5 mmol), 1,3-BDC (166 mg, 1 mmol), and water (10 mL) was placed in a 23 mL Teflon-lined autoclave and placed in an oven

at 170 °C for 7 days (168 hours). The colorless crystals were then decanted from the clear, colorless liquid and washed twice with water and ethanol. The solids were left to air dry.

Synthesis of [Ln₂(OBA)₃(H₂O)_{5.5}·0.5H₂O] (6)

To an aqueous solution of EuCl₃ (150 mg, 0.41 mmol), the disodium salt of 4,4'-oxybis(benzoic acid) (100 mg, 0.39 mmol) in water was added. Precipitation immediately occurred. The white solids were filtered and washed twice with ethanol and water and dried in air.

Synthesis of [Ln(BPDC)₃(H₂O)₃] (7)

A mixture of Eu(NO₃)₃·5H₂O (115 mg, 0.27 mmol) and BPDC (100 mg, 0.37 mmol) were dissolved in water (5 mL) and placed in a 23 mL Teflon-lined stainless steel autoclave. The vessel was heated at 200 °C for 24 h, 175 °C for 24 h, and then 150 °C for 24 h. The vessel was then removed from heat and left to cool to room temperature where the yellow crystals were collected and washed twice with water and ethanol.

Synthesis of [Ln(PYDC)(HPYDC)(H₂O)] (8)

The compound was synthesized through methods from the literature. [132] A mixture of EuCl₃ (92 mg, 0.73 mmol) and 2,3-pyridinedicarboxylic acid (100 mg, 0.60 mmol) were added to water (7 mL) in a 23 mL Teflon-lined autoclave. The vessel was then heated at 120 °C for one day (24 hours). After cooling to room temperature, clear, colorless crystals were isolated from the supernatant liquid, washed with water and ethanol three times and left to dry.

Synthesis of [Ln(FDC)(HFDC)(H₂O)] (9)

An aqueous mixture of Eu(NO₃)₃·6H₂O (122 mg, 0.275 mmol) and dimethyl-3,4-furandicarboxylate (50 mg, 0.275 mmol) in water (3 mL) was added to a 23 mL Teflon-lined autoclave. Aqueous potassium hydroxide (5 M KOH) was added to adjust the pH to 7-9. After 3 days (72 hours) of hydrothermal treatment at 120 °C, the solution was decanted from the clear, colorless crystals, and washed twice with water and ethanol, after which they were allowed to air dry.

5.2 Results and Discussion

Compounds **1** – **9** were chosen due to their varying topologies, number of coordinated OH oscillators, and linker composition (Figure 30). The target structures were synthesized with Eu, Gd, and Tb ions and structures were confirmed with powder X-ray diffraction. The first set of compounds, **1** – **4**, use the 1,4-BDC linker. Compound **1** is made of two-dimensional sheets, held together by extensive hydrogen bonding to form a 3D network (Figure 31). Compound **2** resembles the stereotypical 3D, porous metal-organic framework structure with two bound water molecules per Ln center, which are extended in three dimensions by the linker (Figure 32). Compounds **3** and **4** are similar in composition and consist of dense Ln-hydroxide sheets (Figure 33). These two-dimensional sheets are stacked by the organic linker into a three dimensional compound akin to a pillared clay, more resembling a traditional inorganic network solid than the other compounds, with two and one bound water molecule(s) per Ln ion, respectively. Compound **5** is comprised of 1,3-BDC and forms one-dimensional helical chains with two coordinated aqua ligands (Figure 34). Compound **6** is constructed with the OBA linker, which has an sp³ ether oxygen atom connecting two benzoate groups (Figure 35).

The CP is compact and three dimensional, with approximately three coordinated aqua ligands. Compound **7** is composed of a rigid, aromatic BPDC linker that forms a two dimensional compound with three aqua ligands coordinated to each Ln center (See Chapter 4). Similar to **1**, compounds **8** and **9** consist of two dimensional sheets composed of Ln dimers extended by the linker, which acts to hold the sheets together through hydrogen bonding (See Chapter 3). Each Ln has one bound aqua ligand. Instead of a central benzene core as in **1**, however, the linkers consist of a pyridine (**8**) ring and furan (**9**) ring.

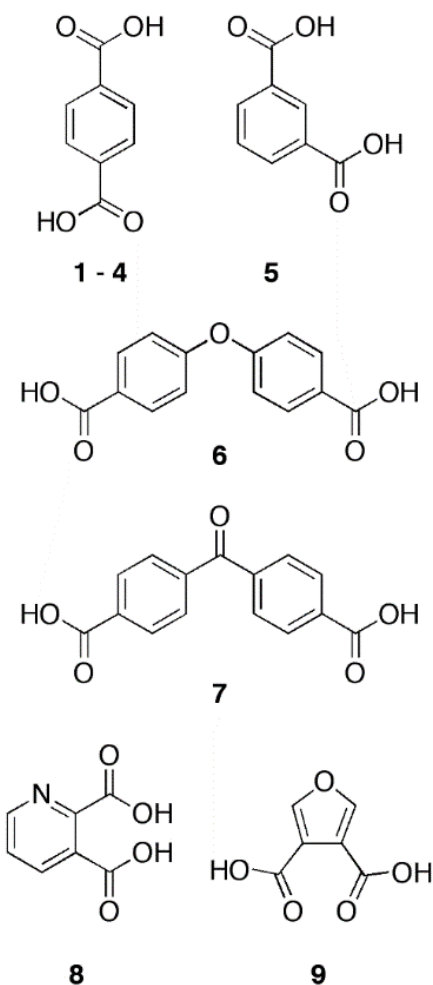


Figure 30. Linkers used in compounds **1** – **9**.

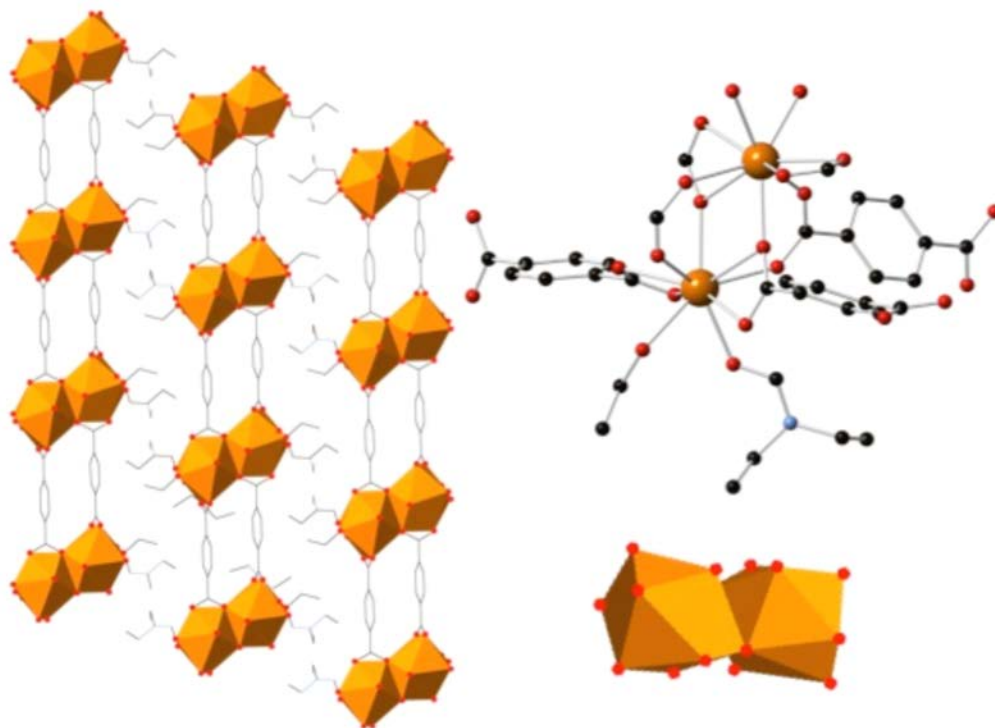


Figure 31. *Structure (1) previously obtained by MacNeill et. al. with two dimensional sheets made of dimers.*

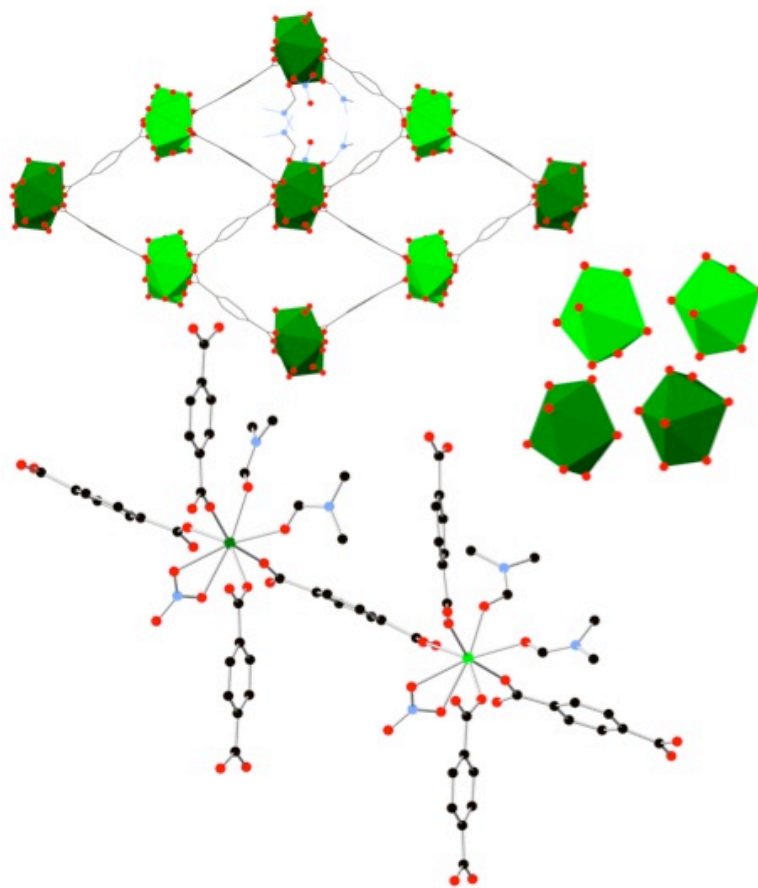


Figure 32. Structure (2) reported by Reineke *et. al.* comprised of Ln(III) monomers into a prototypical MOF motif.

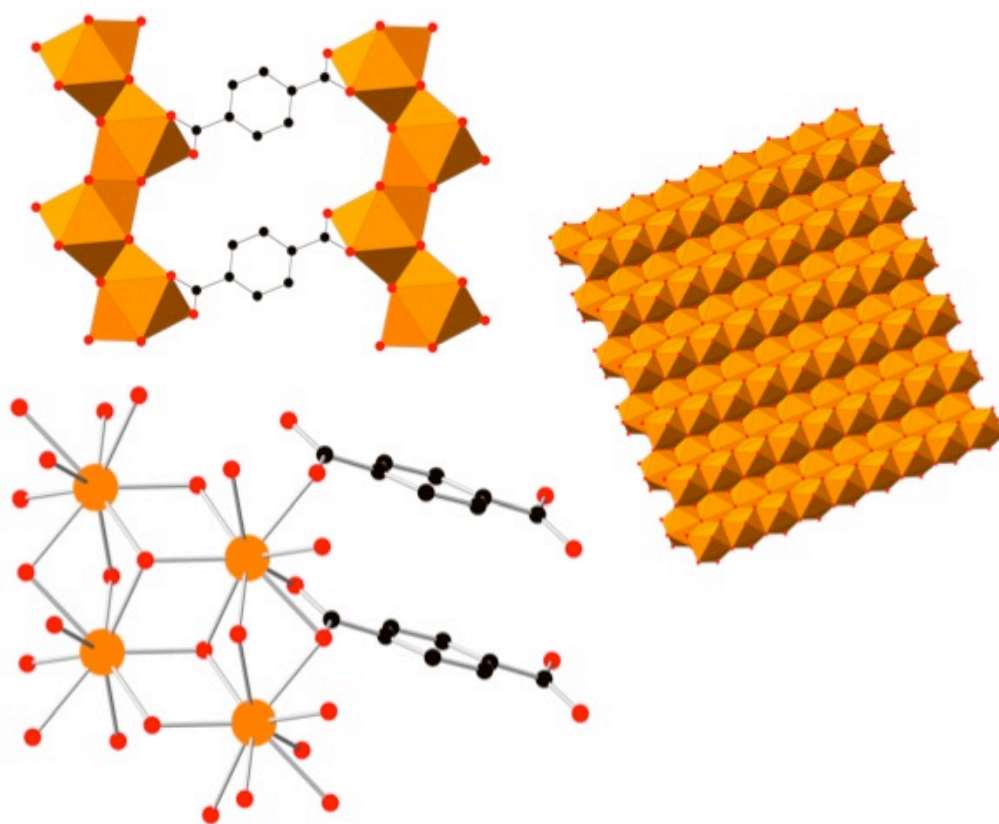


Figure 33. Structure (3) synthesized by Serre *et. al.* comprised of two dimensional sheets made of lanthanide hydroxide sheets.

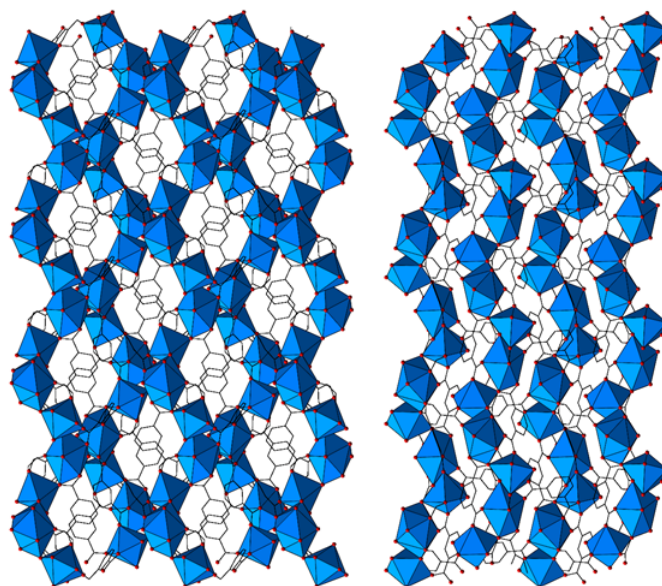


Figure 34. Structure (5) synthesized by Fan *et. al.* comprised of helical Ln(III) chains (blue) tethered together by 1,3-BDC linkers.

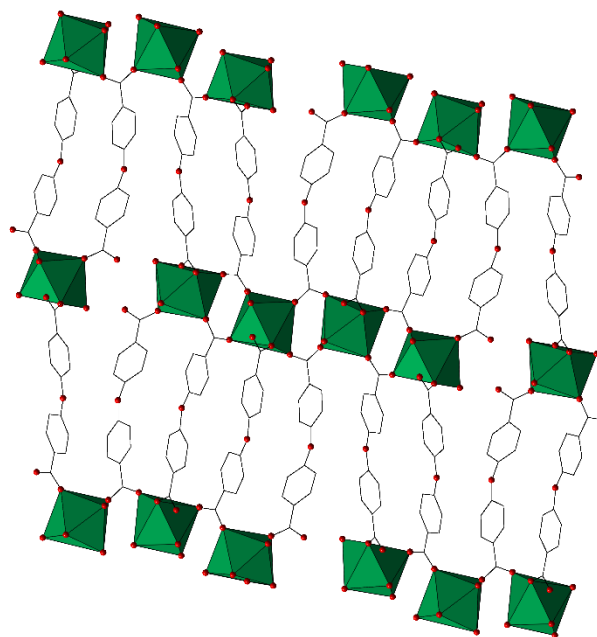


Figure 35. Structure (6) synthesized by Luo *et. al.* comprised of Ln(III) monomers (green) bridged by 4,4'-oxybis(benzoic acid).

The triplet state of the molecular organic antenna is commonly used as a major contributing factor in the efficiency of the antenna effect in molecular complexes, but it cannot be used to explain sensitized luminescence in Ln CP systems. Arguably the most followed tenet when designing a sensitizer states that the energy difference between the sensitizer's triplet state and that of Eu's 5D_0 state should be approximately 2,500 to 3,500 cm^{-1} and approximately 2,500 to 4,000 cm^{-1} for Tb's 5D_4 energy level for maximized sensitization efficiency, assuming efficient ISC from the singlet to triplet states. [161, 162] This is a very general rule, with exceptions and intricacies to it. Low temperature luminescence studies were performed on each linker in an acetonitrile solution with Gd(III) to obtain the organic sensitizer's triplet state value (Table 20). [76] When these values were used to find a similar correlation between the triplet state of the molecular and quantum, yield of the CPs, this general tenet began to fail as more systems were studied. It was thus hypothesized that treating CPs and MOFs in a manner akin to molecular complexes was an invalid approach. Instead, the nature of MOFs and CPs extended network structures needed to be considered.

5.2.1 Evaluation of Molecular-Based Approach

First, **1 – 9** were studied using triplet state values determined from molecular complexes. With an energy difference of more than 5,000 cm^{-1} to the emissive levels of Eu and Tb in the BDC systems (**1 – 4**), 1,4-BDC should display poor luminescence with a triplet state of 25,410 cm^{-1} . However, the energy difference between the 5D_1 manifold of Eu and the triplet state of 1,4-BDC does indeed fall within this ideal energy range at 3,200 cm^{-1} (Table 19, Table 21), which could potentially explain the ~10% quantum yield observed in these four systems. Here, energy transfer to the 5D_1 manifold in Eu occurs,

followed by internal conversion to the 5D_0 manifold to produce Eu emission. The higher quantum yield of Tb (26 – 35%), however, is not explicable by this triplet state value. The energy difference between the triplet state of 1,4-BDC and 5D_4 emitting manifold is too large at an energy difference of $\sim 4,980\text{ cm}^{-1}$, and is too low in energy to resonate with the 5D_3 level. This should result in a minimal quantum yield in the Tb system, opposite of what is seen. Since the singlet and triplet states of 1,3-BDC are effectively identical to 1,4-BDC, with similar quantum yields, the same analysis holds for **5**.

In the OBA system (**6**), the triplet state of $27,840\text{ cm}^{-1}$ allows or population of the excited state manifold of the Eu ion with an energy difference of $6,395\text{ cm}^{-1}$ from the 5D_2 level, though it can potentially resonate with 5D_3 ($\Delta E = \sim 3,470\text{ cm}^{-1}$) and/or 5L_6 ($\Delta E = \sim 2,660\text{ cm}^{-1}$). However, these manifolds are much higher than Eu's emissive level, which could adequately explain the reported QY of 3.9%. In the Tb system, the quantum yield of 66% is surprising, as the OBA's triplet state is nearly too close in energy to the 5D_3 level ($\Delta E = \sim 1,570\text{ cm}^{-1}$), facilitating potential back transfer. The ET range of $7,410\text{ cm}^{-1}$ from the triplet state to Tb's 5D_4 emissive level is too large to allow for efficient ET. Combined, these factors should result in minimal sensitization of Tb emission instead of the high quantum yield observed.

In the BPDC system (**7**), the triplet level of $23,420\text{ cm}^{-1}$ is too high to efficiently populate Eu's 5D_1 and 5D_0 energy manifold, however, the 5D_2 energy manifold is only $1,975\text{ cm}^{-1}$ from the triplet state of BPDC, which could reduce sensitization by a back transfer process. Despite this, a 35.5% quantum yield was instead recorded. For the Tb system, however, the energy difference of $2,990\text{ cm}^{-1}$ should be ideal for efficient energy transfer to Tb's 5D_4 emitting level, but the quantum of 6% does not reflect this.

The triplet state of the PYDC linker (**8**) at 25,970 cm⁻¹ follows the similar trend as OBA, such that it is close in energy with higher levels (⁵D₃, ⁵L₆) of the Eu(III) ion, yet too far from ⁵D₂ to resonate with this level. This would result in no appropriately suited energy manifolds in Eu for efficient energy transfer, explaining the low quantum yield. In the Tb system, the energy difference between ⁵D₄ and the linker's triplet state is greater than 5,000 cm⁻¹, which can also effectively explain the poor QY of 4.6%.

The FDC linker's (**9**) triplet state of 23,1980 cm⁻¹ is most likely too high to promote efficient energy transfer to the ⁵D₁ level of the Eu(III) ion with an energy difference of 4,170 cm⁻¹, just outside the optimum ET range and too close to ⁵D₂ ($\Delta E = \sim 1,700$ cm⁻¹), resulting in the observed QY of 1.1%. In the Tb system, the only energy level that could be occupied is the ⁵D₄ emissive level with an energy difference of 2,760 cm⁻¹, which is within the range of optimum energy transfer and should promote decent quantum yields, but an efficiency of 3.3% was instead observed. The low Tb quantum yield can be justified through nonradiative deactivation of the ⁵D₄ manifold by the bound aqua ligand (See Chapter 4).

Table 19. Quantum yield (%), lifetime (ms), number of OH quanta, secondary building unit, and overall dimensionality of Eu and Tb analogs of **1** – **9**.

Compound	Φ_{Eu} (%)	Eu τ (ms)	Φ_{Tb} (%)	Tb τ (ms)	# OH	SBU	Dim
1	12.6 \pm 2.1	0.560 \pm 0.012	26.1 \pm 3.8	1.260 \pm 0.173	1	Dimers	2
2	9.5 \pm 0.8	0.264 \pm 0.006	37.0 \pm 2.4	0.724 \pm 0.025	4	Monomers	3
3	10.3 \pm 1.6	0.240 \pm 0.017	36.3 \pm 3.5	0.700 \pm 0.045	4	Sheets	3
4	9.8 \pm 5.4	0.358 \pm 0.071	35.0 \pm 12.3	0.731 \pm 0.053	2	Sheets	3
5	10.4 \pm 0.8	0.476 \pm 0.005	31.9 \pm 3.0	1.020 \pm 0.040	4	Chains	1
6	3.9	0.28	66	0.79	~6	Monomers	1
7	35.5 \pm 4.9	0.265 \pm 0.016	6.0 \pm 0.3	0.280 \pm 0.023	6	Monomers	2
8	2.6 \pm 0.3	0.530 \pm 0.010	4.6 \pm 0.18	1.21 \pm 0.100	2	Dimers	2
9	1.1 \pm 0.3	0.387 \pm 0.0001	3.3 \pm 0.8	0.769 \pm 0.0006	2	Dimers	2

Table 20. Photophysical measurements of each system in the molecular and CP states with Gd(III).

Compound	Linker	Molecular States		CP States	
		^1S (cm $^{-1}$)	^3T (cm $^{-1}$)	^1S (cm $^{-1}$)	^3T (cm $^{-1}$)
1	1,4-BDC	29,850	25,410	30,960	25,970
2	1,4-BDC	29,850	25,410	30,960	25,970
3	1,4-BDC	29,850	25,410	30,960	25,970
4	1,4-BDC	29,850	25,410	30,960	25,970
5	1,3-BDC	32,790	25,060	31,250	25,910
6	1,3-BDC	32,790	25,060	31,250	25,910
7	OBA	34,680	27,840	26,670	22,420
8	PYDC	32,790	25,970	26,180	21,050
9	FDC	31,619 ^a	23,186 ^a	30,030	21,834
10	BPDC	30,580	23,420	23,040	20,410

^aHydrolyzed linker calculated with Gaussian. [84]

5.2.2 Evaluation of Band-Based Approach.

After the analysis of **1 – 9** using the commonly used molecular triplet state approach, inexplicable deviation in nearly every system arose. Taking the extended network nature of CPs coupled with the unique chemistry of lanthanide ions, it was hypothesized that the organic linkers would behave more like aggregated organic compounds with band structure rather than discrete molecular antennae. [61-63] As such, the band nature of network solids would need to be considered when studying sensitized luminescence. The composition of a CP's conduction band is largely derived from the organic linker as shown by several computational studies. [163-165] It has even been noted that in lower energy band gaps are observed for linkers with larger numbers of sp^2 carbon atoms. [165] In such instances, an electron is being excited from the material's valence band to the conduction band. Charge carrier recombination eventually occurs resulting in an energy transfer that permits population of the f^* state to promote sensitized emission. To investigate this further, compounds **1 – 9** were synthesized with Gd(III) ions to form isostructural analogs from which the triplet band energy level of these compounds were determined. The triplet band energies were then used to justify the photoluminescent behavior of **1 – 9** (Table 20).

The triplet state of the band in BDC-based systems (**1 – 5**), at $22,220\text{ cm}^{-1}$, more accurately explains the observed quantum yields of these systems ($\sim 10\%$ in Eu, $\sim 33\%$ in Tb). In the Eu system, energy can transfer from BDC's triplet band to the 5D_1 level ($\Delta E = 3,200\text{ cm}^{-1}$) occurs, followed by internal conversion to 5D_0 , which more readily rationalizes its quantum yield. In the Tb system, the triplet band is $1,790\text{ cm}^{-1}$ from the emissive 5D_4 level of the Tb(III) ion. This is outside the ideal range proposed from the

classic model for complexes, usually resulting in ineffective population of f^* due to back transfer, yet moderately decent quantum yields are observed. This could be due to the nature of CP structures compared to discreet complexes, where aggregation and intermolecular interactions are strong and static. While this ideal range for energy transfer in complexes was empirically determined from decades of research, it is likely that some modifications to this may be required for CPs, but can only be estimated once significantly more data have been collected.

The OBA linker in **6**, with too high a molecular triplet state, does not convincingly explicate the observed luminescence in this system. In the band model, however, a triplet energy band of $22,420\text{ cm}^{-1}$ is $1,990\text{ cm}^{-1}$ from Tb's 5D_3 emissive level, explaining the high quantum yields. The triplet band energy is in resonance with Eu's 5D_2 energy manifold, allowing for potential back transfer and subsequent luminescence quenching and/or energy loss to internal conversion processes to populate Eu's 5D_0 emitting level, explaining the poor quantum yield of 3.9% for the Eu system.

In the BPDC system (**7**), which has been described previously, the triplet band energy of $20,410\text{ cm}^{-1}$ is essentially identical to Tb's 5D_4 , too close to its emissive level, explaining the poor quantum yields of 6.0%. In the Eu system, the energy can be effectively transferred to the 5D_0 state of the Eu ion, producing a quantum yield of 35%.

In the PYDC system (**8**), the triplet band energy transfer to the 5D_0 level of the Eu(III) ion is favorable at $3,800\text{ cm}^{-1}$, although a close interaction range of $2,030\text{ cm}^{-1}$ to Eu's 5D_1 manifold may allow for back transfer, effectively predicting the outcome of poor Eu luminescence in this system. In the Tb system, the only manifold that could potentially be occupied is the 5D_4 emissive manifold, which is too close in energy from

PYDC's triplet band ($\Delta E = 620 \text{ cm}^{-1}$) to allow for efficient energy transfer, explaining the poor quantum yield value of 4.6%. There also exists multiple strong π - π interactions within this system, which may influence the energy transfer mechanism, as discussed later.

The triplet band system of **9** has an energy of $21,830 \text{ cm}^{-1}$. This energy is too close in resonance for the 5D_2 energy level of the Eu(III) ion, which may deactivate luminescence resulting in the poor quantum yields observed. Similarly, the triplet band is in close resonance with the 5D_4 level of the Tb(III) ion, producing the same results. Similar to **8**, the strong interactions between the π systems of the organic linkers may also play a role in the photophysical processes involved.

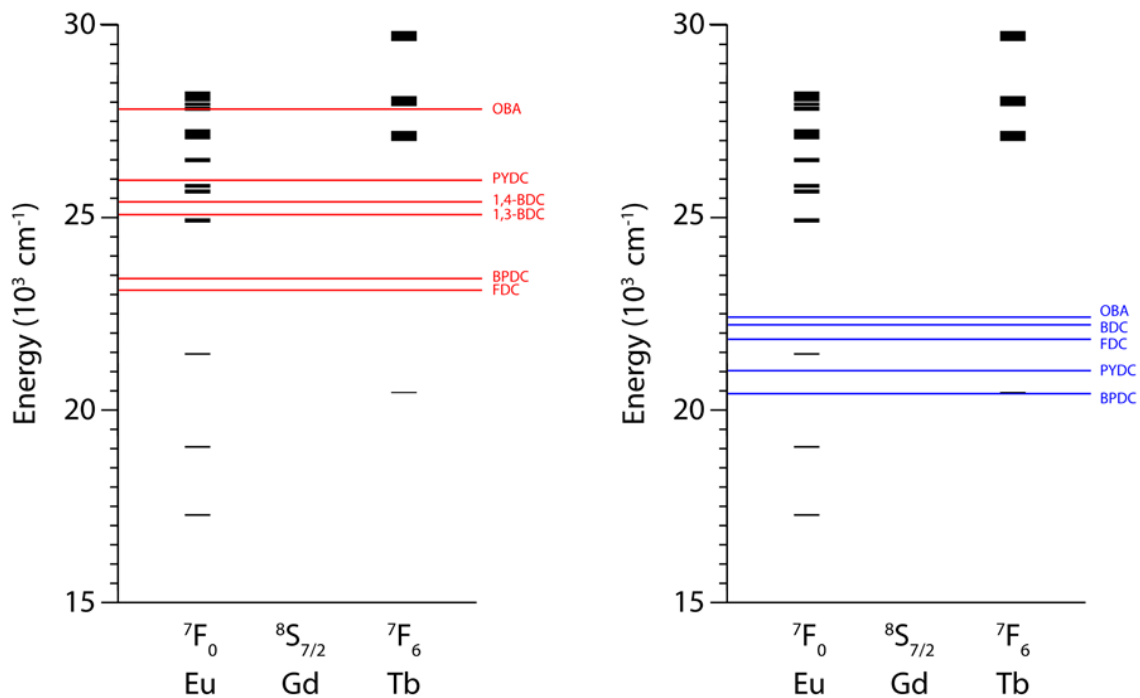


Figure 36. Modified Dieke diagrams of Eu, Gd, and Tb ions with experimentally obtained energy levels of the molecular triplet states (left, red) and triplet bands (right, blue) of the linkers and CPs used. Since 1,3-BDC and 1,4-BDC have the same triplet band energies, they have been combined in the band figure for clarity.

Table 21. *Difference from energy levels of linker to energy states of Ln(III) ions.*

	Triplet State for Molecule					Triplet Band for CP				
	Eu(III) System ^a			Tb(III) System ^b		Eu(III) System ^a			Tb(III) System ^b	
	⁵ D ₀	⁵ D ₁	⁵ D ₂	⁵ D ₄	⁵ D ₃	⁵ D ₀	⁵ D ₁	⁵ D ₂	⁵ D ₄	⁵ D ₃
1,4-BDC	8,140	6,380	3,910	4,950	-860	4,950	3,190	720	1,760	-4,050
1,3-BDC	7,790	6,030	3,560	4,600	-1,210	4,950	3,190	720	1,760	-4,050
OBA	10,570	8,810	6,340	7,380	1,570	5,150	3,390	920	1,960	-3,850
BPDC	6,150	4,390	1,920	2,960	-2,850	3,140	1,380	-1,090	-50	-5,860
PYDC	8,700	6,940	4,470	5,510	-300	3,780	2,020	-450	590	-5,220
FDC	5,920	4,130	1,690	2,730	-3,080	4,560	2,800	330	1,370	-4,440

^aWhere ⁵D₀: 17,270 cm⁻¹; ⁵D₁: 19,030 cm⁻¹; ⁵D₂: 21,500 cm⁻¹. ^bWhere ⁵D₄: 20,460 cm⁻¹; ⁵D₃: 23,270 cm⁻¹. [166]

5.2.3 Further Considerations of the Band Nature of Organic Solids

In molecular complexes, the absorption and emission of UV/Vis/NIR radiation are dictated by two selection rules: Laporte and Spin selection rules. In the antenna effect, what this generally means is that singlet state emission, being an allowed transition, is short-lived, decaying faster than energy transfer to a Ln can generally occur, but intersystem crossing to the triplet state can happen. Once the triplet state is populated, its longer lifetime caused by its forbidden return to the ground state provides enough time for energy transfer to occur, exciting the Ln ion followed by emission. In network solids where band formation occurs, an additional selection rule concerning the absorption and emission of phonons (Δk , crystal momentum) is required if the band transition is indirect (i. e., forbidden) in nature. This means that if the Ln CP under study has an indirect band gap, decay from the singlet band is forbidden, possibly being long-lived enough to be a contributor to lanthanide sensitization. Thus, singlet sensitization of lanthanide ions in Ln CPs and MOFs is a potentially more common occurrence than in complexes, and needs to be considered when evaluating the luminescence of these

materials. While most linkers currently in use in the construction of Ln CPs have large band gaps with high singlet band energies, in linkers with lower band gap energies (close to those found in semiconductors instead of insulators), the singlet sensitization pathways could be significant. Of course, this is a simplistic evaluation, as band structure and band transitions in organic semiconductors are fundamentally more complicated than inorganic semiconductors. [167-172]

5.2.4 Triplet versus Spectral Overlap Approaches

When luminescent lanthanide-hybrid systems are analyzed, it is very common to see the discussion restricted to a cursory description based largely on the triplet state. This often provides a simplified discussion as to the sensitization process, and while convenient, it does not always produce a complete picture. In molecular systems, the triplet discussion is arguably sufficient in that any population of higher energy states on the lanthanide by higher energy levels of the ligand would likely be insignificant compared to the dynamics involved in ligand exchange, solvent interactions, etc. Lanthanide CP systems, however, are static. If a higher energy level on the lanthanide is populated, there are fewer competing mechanisms for nonradiative deactivation. Aside from loss during internal conversion, the population of these higher energy manifolds in lanthanide CPs may be more significant. For a more accurate and precise view of the energy transfer processes in lanthanide CPs, the overlap between donor (linker) emission and acceptor (lanthanide) absorption spectra may need to be considered instead of just the singlet or triplet band energies, where better overlap generally produce better luminescent behavior. [155]

5.2.5 Influence of High-Energy Vibrational Quanta

Vibrational quanta such as high-energy CH, NH, and OH oscillators provide a pathway for nonradiative decay, reducing efficiencies in these systems. When constructing luminescent lanthanide complexes, the sensitizing organic ligand is designed to reduce the presence of these oscillators, especially those from bound aqua ligands. [72] Three to four OH quanta are sufficient to fill the energy gap between Eu and Tb's excited and ground states. [56, 71] Within CPs, bound aqua ligands do not appear to be nearly as detrimental, likely due to the presence of extensive, static hydrogen bonding. The systems selected for this study contain 1 to 6 OH oscillators bound to the lanthanide ion, and it is expected that a decrease in emission efficiency should be seen as more aqua ligands coordinate to the lanthanide center. Instead, quantum yields for both the Eu (~10%) and Tb (~35%) systems are statistically nearly identical in cases for the 1,4-BDC systems, even though the lanthanide centers were coordinated to an ethanol (**1**), one aqua ligand (**4**), and two aqua ligands (**2**, **3**). While the presence of increasing oscillators more or less decreases the excited state lifetimes as expected (Table 19), their presence does not appear to consistently influence emission quantum yields in a similar manner. Since it is well known and has been reported that these high-energy oscillators do impact emission quantum yields, it is evident that decently emissive lanthanide CPs can be constructed even with such oscillators present. It is believed that the strong hydrogen bonding networks reduce their overall impact, and that similar hydrogen bonding motifs in the 1,4-BDC systems result in similar quantum yields despite the presence of varying numbers of OH oscillators. Interestingly, there is a strong linear correlation between lifetimes and number of OH oscillators in all but **8**, possibly due to the influence of the

Ln-N bond from the pyridine moiety of the linker. [173] It is possible that a coordination sphere largely dominated by aqua ligands and/or a weak hydrogen-bonding network would negatively impact the sensitization efficiency more than observed within these systems.

There have been studies highlighting the influence of such high-energy oscillators in CP systems. [155, 174] In some cases, such as changing H₂O to D₂O, there is an easy correlation. In other systems, such as changing CH to CF in 1,4-BDC, the correlation may be less straightforward. In such instances, the electronic effects of changing substituents on the linkers need to likewise be considered. This change can impact singlet/triplet band energies, as well as overall energy transfer dynamics due to electron-withdrawing or -donating effects. As this model is further developed with additional research, such differences will need to be carefully distinguished between and evaluated separately.

5.2.6 Topological Impact on Sensitized Luminescence

The 1,4-BDC and 1,3-BDC systems, with essentially identical quantum yields and singlet/triplet band energies can be used to show how topological diversity does not seem to have a drastic impact on sensitized luminescence in these lanthanide CPs. With varying overall dimensionality (1-3), differing SBU dimensionality (0-2), and different general overall structural motifs (2D CP → 3D MOF → clay-mimetic), it would appear that the general CP/MOF structure has minimal influence on luminescence. Other structural effects related to NRD mechanisms and organic aggregation effects seem more important than the nature of the inorganic unit. While this study aimed to show diversity in both structural topology and organic linker energetics, the number of structures is

limited and this correlation cannot be definitively stated. One aspect of these structural motifs that can impact emission is the SBU, in that it can promote concentration quenching effects. By diluting the emissive lanthanide centers in a “non-emissive” lanthanide matrix such as La, Ce, or Gd, optimal doping concentrations for maximum efficiencies can be determined (Chapter 6). [32, 33, 175-181] This is also used to promote Ln-Ln' sensitized emission, which can tailor emission profiles and is commonly used to produce white-light emitting materials. [30-34, 182-184]

The potential for aggregation can arise in these materials, which is not necessary to consider in isolated molecular complexes, but can impact concentrated solutions and solid phases of such complexes. Compounds **6** (OBA), **7** (BPDC), **8** (PYDC), and **9** (FDC) do have significant π - π interactions within the 3.0 to 4.9 Å range, which may provide a pathway for deactivation of luminescence. [185, 186] In the OBA system (**6**), the close interacting centroid systems are stacked at unfavorable angles (less than 45°), unlikely allowing effective aggregation-based reduction of emission. The unusual channels within the structure of **7** consisting of head-to-tail interactions of the BPDC linkers could lead to possible aggregation-based behavior. [187] These distances around 2.6 Å between linkers in the same geometric plane and π - π interactions distances around 3.5 Å could lead to reduced emission, but this impact on luminescence is currently uncertain, as Eu luminescence was remarkably high. Other systems, with π - π , C-H $\cdots\pi$, S $\cdots\pi$ interactions show significant increases (1.5 to 7-fold increases) upon introduction of various stacking motifs into organic crystals. [188] The result of these effects on emission and the fundamental luminescence of lanthanide CPs is largely underdeveloped, but should be taken into consideration when evaluating luminescent lanthanide CPs.

5.2.7 Quantitative Assessment of Eu Emission

The emission profile of Eu complexes has long been used to estimate several quantitative factors impacting sensitized emission. These include the determination of radiative and nonradiative decay rates, intrinsic Eu quantum yield, and sensitization efficiency of the organic linker. When similar studies are applied to Ln CPs, the necessity to treat these compounds differently from complexes is further demonstrated (Table 22). From this table, it is evident that radiative rates do not vary much. This supports the premise that the SBU structure has minimal impact on sensitized emission. Most strikingly, however, is the possibility of obtaining quantum yields that surpasses the intrinsic Eu quantum yield, leading to linker sensitization efficiencies greater than 100%. In the BPDC system in Chapter 4, such an increase was attributed to a coupling of high-energy OH oscillations with internal conversion processes that acted to support the Eu sensitization pathway. Since the values in Table 22 are determined indirectly from experimental data rather than directly calculated, the nonphysical values of $\eta_{\text{sens}} \gg 100\%$ is a reflection of this. The experimental lifetimes used in these calculations is only a measure of NRD pathways and does not account for any assistance these oscillators may contribute to the sensitization process. Thus, η_{sens} may appear to be greater than 100% in systems where this assistance is occurring. It is further speculated that the strong hydrogen-bonding interactions may also be partially responsible for this observation. Regardless, it is clear that using methods and techniques derived from complexes are not fully applicable in CPs.

Table 22. *Luminescence parameters for compounds 1 – 9.*

Compound	η_{sens}	Φ_{Eu}	τ_{rad}	κ_{rad}	κ_{nonrad}
1	114%	11.1%	0.0051 s	196.08 s ⁻¹	1589.6 s ⁻¹
2	192%	4.94%	0.0053 s	188.68 s ⁻¹	3599.2 s ⁻¹
3	244%	4.33%	0.0055 s	181.82 s ⁻¹	3984.8 s ⁻¹
4	143%	6.86%	0.0052 s	192.31 s ⁻¹	2600.9 s ⁻¹
5	102%	10.1%	0.0047 s	212.77 s ⁻¹	1888.1 s ⁻¹
6	49%	7.9%	0.0035 s	285.71 s ⁻¹	3285.7 s ⁻¹
7	697%	5.1%	0.0052 s	193.67 s ⁻¹	3579.9 s ⁻¹
8	25%	10.3%	0.0056 s	178.57 s ⁻¹	1708.2 s ⁻¹
9	15%	7.5%	0.0053 s	188.68 s ⁻¹	2395.3 s ⁻¹

5.3 An alternative to the antenna model for molecular complexes

From the systems studied, there are several criteria to consider for the band model of sensitized luminescence in lanthanide coordination polymers.

First, the triplet band of the organic must resonate with any of the f-excited states within the lanthanide ion manifold, but the higher the energy of the manifold, energy losses from internal conversion are expected. In this case Ln ions act as a dopant within an organic matrix with band structure, similar to lanthanide-doped inorganic semiconductors. This is due to the contracted nature of the f-orbitals not interacting with the organic linker, thus having minimal influence on the photodynamics of the organic matrix. [189, 190] Based on molecular systems, the energy transfer from the conduction band to an f*-state is assumed to have an ideal range around 2,000 to 4,000 cm⁻¹. While significant deviation from this guideline is not expected, further studies will need to be performed to empirically determine a range appropriate for CP systems. Congruent sensitization by both the singlet and triplet bands in Ln CPs is likely more common in

CPs dependent upon if the band transition is direct (allowed) or indirect (forbidden). [171, 191, 192]

Next, high-energy oscillators may play either a positive or detrimental role for sensitized emission. High-energy oscillators can be detrimental by offering nonradiative decay pathways through OH/OD or CH/CF oscillators. [174] Although this may not be as detrimental as in molecular complexes since there is no dynamic ligand exchange and the framework is often stabilized by strong hydrogen bonding interactions, it is clear that their presence does not necessarily result in poor luminescence. In other instances, it has been noted that these oscillators can sometimes be beneficial to the luminescence where emissions is increased in their presence. [26, 73, 155] When studying these oscillators, care should be taken to consider any potential electronic effects induced upon changing of sensitizing linker functionality (e.g., changing from C-H bonds to C-F bonds in BDC).

Finally, the nature of the secondary building unit and overall dimensionality of in Ln CPs seems to be less important as anticipated (Table 19). In the case of lanthanide CPs, self-quenching is much more important than SBU structure, so dilute concentrations of the emissive Ln may need to be considered. [193-195] Linker aggregation effects are likely to pose a significant contribution to sensitized emission in these materials. [187] All of these influences may be seen in the quantitative assessment of the photodynamics of these systems, where linker sensitization efficiencies may appear larger than physically feasible.

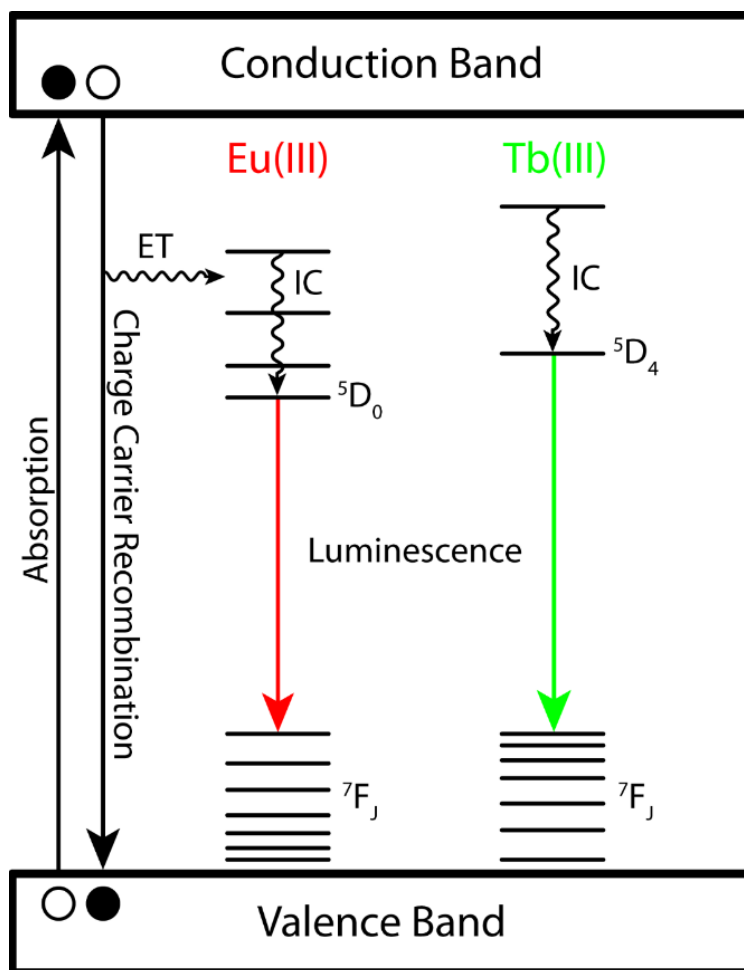


Figure 37. Proposed band model diagram where an electron is promoted from the valence band to conduction band, charge carrier recombination occurs and the energy is then transferred to the manifold of the Ln ion. The emissive state of the Ln ion is occupied through internal conversion, followed by luminescence. Here, ET=energy transfer, IC=internal conversion.

Using methodologies derived from molecular systems on lanthanide CPs needs to be considered carefully. While the antenna effect is a valid way to promote sensitized emission in lanthanide CPs, guidelines established from molecular complexes need to be modified to account for the unique nature of lanthanide CPs. Comparing the newly

proposed “band model” versus the antenna model illustrates that in many instances the antenna model guidelines fail to explain sensitized emission in lanthanide CPs. The antenna model emphasizes the triplet state energy of the organic linker being important for energy transfer to the lanthanide ion, whereas in the band model the triplet band produced from the periodic array of the organic within these materials is a more accurate predictor of sensitization efficiency, though singlet sensitization and other effects may also need to be considered. The spectral overlap approach may also provide a more precise and more accurate depiction of the energy transfer processes involved. Aromatic linkers are required for both models; in the antenna model they are required to produce bands through delocalization of sp^2 orbitals. In both approaches, the presence of high-energy oscillators can reduce emission by nonradiative decay mechanisms, but seems to be less detrimental in lanthanide CP systems, and in some rare cases can even assist in the sensitization efficiency.

5.4 Conclusion

Herein, the features of lanthanide CP systems that need to be considered when studying their sensitized luminescence has been outlined, though there is more research needed to further establish concrete guidelines. It is expected that future work on luminescence lanthanide CPs and MOFs will be evaluated by the band model, allowing for this approach to be further developed. Detailed excitation, absorption, and computational studies will also surely serve to address these parameters to a greater extent.

CHAPTER 6: EFFECTS OF LANTHANIDE DOPING IN

$[\text{Ln}(\text{C}_6\text{H}_8\text{O}_4)_3(\text{H}_2\text{O})_2] \cdot (\text{C}_{10}\text{H}_8\text{N}_2)$, GWMOF-6

Heteronuclear lanthanide coordination polymers have shown great promise in recent years due to their presence in a diversity of applications. Previous contributions have shown in mixed Eu/Tb systems, the Tb ion can act as an antenna, after receiving energy from the organic sensitizer, and transfer its energy to the Eu ion. [196] This has also been noted by other groups [151, 193, 197, 198], not only in Eu/Tb systems but with Tb/Yb and Ce/Tb mixtures as well. [31, 199, 200] Investigation into the luminescent behavior of Eu and Tb ions within MOFs by doping of optically inert Ln ions such as Gd(III), since the emissive level of the Gd(III) ion (${}^6\text{P}_{7/2}$) lies too high in energy, can also produce highly luminescent materials [201], which will be shown within the scope of this chapter.

To this end, a series of isostructural MOFs were synthesized with adipic acid, 4,4'-dipyridyl, and varying Ln ion mixtures for the general formula $[\text{Ln}_x\text{Ln}_{1-x}(\text{C}_6\text{H}_8\text{O}_4)_3(\text{H}_2\text{O})_2] \cdot 4,4'$ -dipy (where $\text{Ln}_x = \text{Eu}$ or Tb , and $\text{Ln}_{1-x} = \text{Gd}$) to investigate the effects of concentration quenching with optically inert Ln ions. Further investigation with an optically active spacing ion in an isostructural Tb/Eu system was employed to give insight into the role of Ln-Ln' sensitization. These systems were characterized with powder X-ray diffraction and photophysical measurements.

6.1 Synthesis

In a typical synthesis, a mixture of $\text{Eu}(\text{NO}_3)_3 \cdot 6\text{H}_2\text{O}$ (207 mg, 0.60 mmol), 4,4'-dipyridyl (95 mg, 0.60 mmol), and adipic acid (86 mg, 0.60 mmol) was added to 1.7 mL of water. Ammonium hydroxide (aqueous, concentrated) was then added (60 μL) to adjust the pH to ~ 9 . The vessel was then tightly sealed and heated autogenously at 180 $^\circ\text{C}$ for 3 days (72 hours). After naturally cooling to room temperature, the white cloudy liquid was decanted from crystalline white solids. These solids were thoroughly washed with water and ethanol and left to air dry. Isostructural compounds with varying lanthanide ion concentrations were synthesized in an otherwise identical manner.

6.2 Doping and Powder X-ray Diffraction

The synthesis of isostructural GWMOF-6 systems were confirmed with an Olympus BTX Benchtop PXRD. PXRD patterns were compared to those calculated from single crystal data to confirm phase purity. Isostructural compounds were successfully synthesized with Eu:Gd and Tb:Gd with ratios of 25:75, 50:50, 75:25, and 100:0. Attempts to synthesize compounds with other optically inert lanthanide ions La(III), Ce(III), and Lu(III) were unsuccessful. The ionic radii of these compounds may not be suitable to incorporate into the structure along with Eu or Tb. [45] Elemental analyses were also collected to determine the concentration of lanthanide ions within each sample (Table 23, Table 24, Table 25).

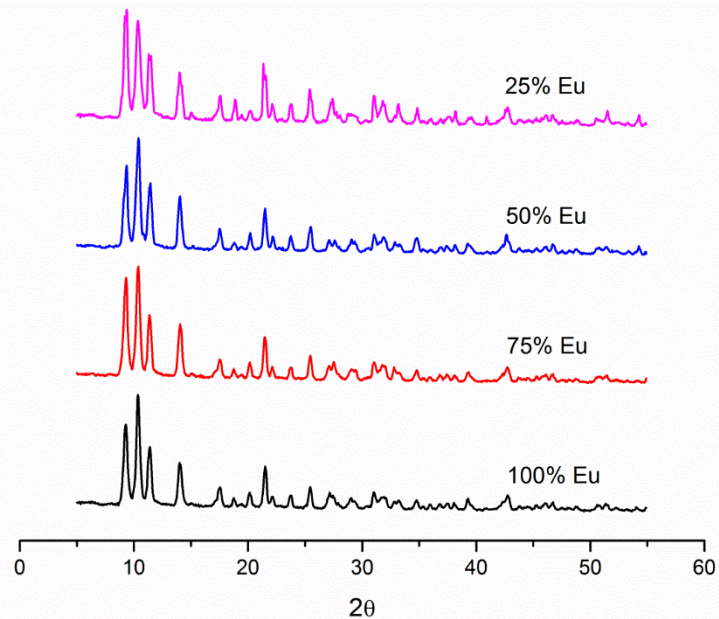


Figure 38. Powder X-ray diffraction pattern of Eu:Gd-GWMOF-6 analogs at 100:0, 75:25, 50:50, and 25:75 doping ratios.

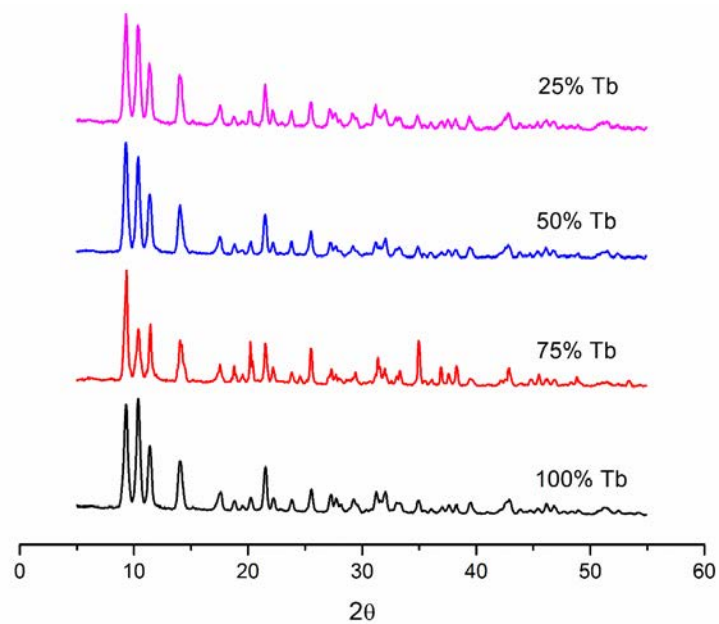


Figure 39. Powder X-ray diffraction pattern of Eu:Gd-GWMOF-6 analogs at 100:0, 75:25, 50:50, and 25:75 doing ratios.

Table 23. Elemental analyses of the doped systems of $[Eu_xGd_y(C_6H_8O_4)_3(H_2O)_2] \cdot 4,4'$ -dipy.

$[Eu_xGd_y(aa)_3(H_2O)_2] \cdot 4,4'$ -dipy	Calculated Ratio	Experimental Ratio	Calculated (found) %				
			Eu	Gd	C	H	N
Eu					35.92	3.82	3.09
Eu_{0.75}Gd_{0.25}	3.00	2.96	24.80	8.37	36.09	3.77	3.02
Eu_{0.5}Gd_{0.5}	1.00	1.02	16.60	16.3	35.98	3.75	2.96
Eu_{0.25}Gd_{0.75}	0.33	0.34	8.56	25.4	35.80	3.72	2.94

Table 24. Elemental analyses of the doped systems of $[Tb_xGd_y(C_6H_8O_4)_3(H_2O)_2] \cdot 4,4'$ -dipy.

$[Tb_xGd_y(aa)_3(H_2O)_2] \cdot 4,4'$ -dipy	Calculated Ratio	Experimental Ratio	Calculated (found) %				
			Tb	Gd	C	H	N
Tb					35.55	3.80	2.95
Tb_{0.75}Gd_{0.25}	3.00	3.01	26.3	8.75	35.46	3.77	2.89
Tb_{0.5}Gd_{0.5}	1.00	1.09	18.2	16.9	34.80	3.74	2.68
Tb_{0.25}Gd_{0.75}	0.33	0.27	7.04	26.5	35.65	3.73	2.94

Table 25. Elemental analyses of the doped systems of $[Eu_xTb_y(C_6H_8O_4)_3(H_2O)_2] \cdot 4,4'$ -dipy.

$[EuTb(aa)_3(H_2O)_2] \cdot 4,4'$ -dipy	Calculated Ratio	Experimental Ratio	Calculated (found) %				
			Tb	Gd	C	H	N
Eu_{0.5}Tb_{0.5}	1.00	1.00	16.8	16.8	35.89	3.79	2.98

6.3 Photophysical Results

6.3.1 *Eu:Gd and Tb:Gd GWMOF-6 systems*

For emission spectra, all samples were in equimolar concentrations and excited at a wavelength of 285 nm, which was also used in the literature (Figure 41, Figure 42). [196] In the doped Eu:Gd system, the compound with the highest intensity was the 50:50, followed by the 25:75, 75:25, and the system with the lowest emission intensity was the pure Eu(III) compound. In the Tb:Gd system, the 50:50 ratio also showed higher emission intensities than the other systems, followed by the 75:25, 25:75, and 100:0. This trend is slightly different than that of the Eu system, where the 25:75 was the second highest in intensity. This difference can be attributed to the energy level of the Eu(III) ion ($17,270\text{ cm}^{-1}$) residing at a lower energy than the Tb(III) ion ($20,460\text{ cm}^{-1}$) [166], which may make the Eu(III) ion more sensitive to neighboring emissive species. Also, Tb(III) has less receiving energy levels, only the 5D_4 , for energy transfer, while the Eu(III) ion has the $^5D_{0,1,2}$ energy levels close together, allowing for the potential for energy transfer processes (Figure 40).

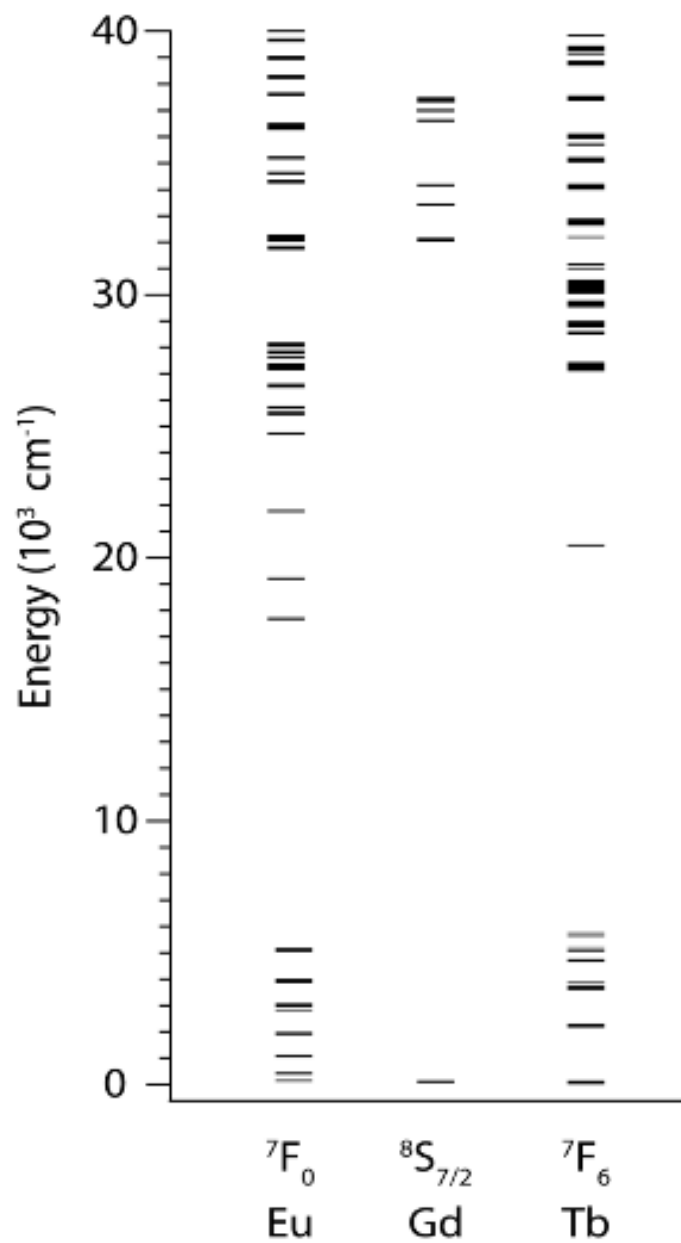


Figure 40. Modified Dieke diagram of Eu, Gd, and Tb ions.

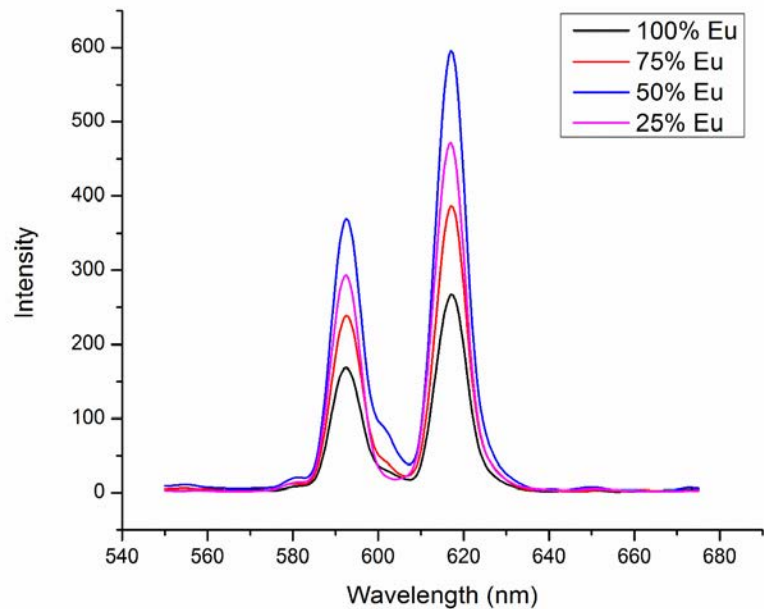


Figure 41. Emission spectra of the Eu:Gd analog of GWMOF-6 at 100:0, 75:25, 50:50, and 25:75 concentration ratios.

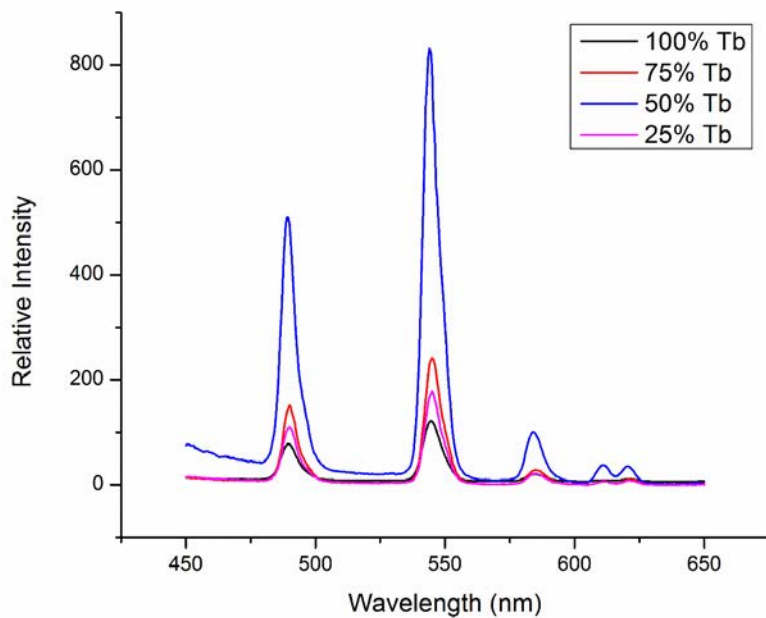


Figure 42. Emission spectra of the Tb:Gd analog of GWMOF-6 at 100:0, 75:25, 50:50, and 25:75 concentration ratios.

Lifetime measurements were also performed and were excited at 285 nm (Table 27). Lifetime values increased as gadolinium concentration increased, which follows the trend seen in doped systems, indicating the Gd ion facilitates longer lived excited energy states. [201]

The quantum yield of the 50:50 Eu:Gd system is the highest at 3.65%, and lifetime values increase upon increasing Gd concentrations as seen in the Tb system. The intrinsic quantum yield of the Eu ion (Φ_{Eu}), radiative lifetime, and the radiative rate constant remain similar across all systems, where the nonradiative rate constant fluctuates depending on the concentration of Gd ions (Table 27), suggesting the presence of nonradiative pathways for deactivation of excited states. Emission data supports the trends in quantum yields, however, the lifetime data varies. This is attributed to receiving energy levels of the Eu(III) ion ($^5\text{D}_{0,1,2}$), where the Tb(III) ion only has one emissive level ($^5\text{D}_4$) close to the triplet state of the 4,4'-dipyridyl antenna.

Table 26. *Quantum yield and lifetime values for $[\text{Ln}_x\text{Ln}_{1-x}(\text{C}_6\text{H}_8\text{O}_4)_3(\text{H}_2\text{O})_2] \cdot 4,4'$ -dipy (where $\text{Ln}_x = \text{Eu}$ or Tb , and $\text{Ln}_{1-x} = \text{Gd}$).*

Compound	Φ_{Eu} (%)	Eu τ (ms)	Φ_{Tb} (%)	Tb τ (ms)
100:0	2.13 ± 0.66	0.7525 ± 0.028	5.65 ± 0.61	1.520 ± 0.002
75:25	1.13 ± 0.15	0.7667 ± 0.006	7.07 ± 1.08	1.559 ± 0.012
50:50	3.65 ± 1.35	0.7837 ± 0.005	7.61 ± 1.30	1.591 ± 0.176
25:75	3.18 ± 0.43	0.7812 ± 0.018	5.54 ± 1.60	1.689 ± 0.023

Table 27. *Luminescence parameters for Eu:Gd systems (100:0, 75:25, 50:50, and 25:75 ratios)*

Compound	η_{sens}	Φ_{Eu}	τ_{rad}	κ_{rad}	κ_{nonrad}
100:0	21.3%	10.0%	0.0075 s	132.95 s ⁻¹	1195.95 s ⁻¹
75:25	11.0%	10.3%	0.0075 s	134.14 s ⁻¹	1170.15 s ⁻¹
50:50	34.9%	10.5%	0.0075	133.59 s ⁻¹	1142.28 s ⁻¹
25:75	30.0%	10.6%	0.0074 s	135.57 s ⁻¹	1144.54 s ⁻¹

Literature reports state that the energy transfer interactions become inefficient when the emissive metal centers are at a distance larger than 10 Å. [87] GWMOF-6 consists of LnO₉ edge shared polyhedra that propagate into chains that extend in the [010] direction that are 9.901 Å apart from neighboring chains. Gadolinium ions can act as spacers between Tb (Eu) centers to reduce the Tb-to-Tb (Eu-to-Eu) energy transfer. [193] The ions within these chains have interatomic distances to neighboring polyhedra of 4.129 Å; however, the distance between alternating metal centers is 7.788 Å. This accounts for the increased quantum yield in the Tb system, as every third metal center along the chain would be 11.762 Å away from the other emissive center. Assuming the random distribution of metal ions between neighboring chains, the closest distance emissive ions can be to each other is 9.907 Å and would constitute a very small fraction within the structure. These reasons lead to the belief that the 50:50 Tb:Gd or Eu:Gd have the optimal distance between lanthanide emissive centers and optimal lanthanide concentration for the maximum emission possible of the ones studied.

6.3.2 Eu:Tb GWMOF-6 System

The next system studied was doping 50:50 Eu:Tb to observe the emission profile and photophysical characteristics of emissive Ln(III) ions within the same matrix. Upon

excitation, energy absorbed by the 4,4'-dipy antenna is transferred to both Eu and Tb ions. The energy residing in the 5D_4 energy level of the Tb(III) ion is then subsequently transferred to the 5D_1 and 5D_0 levels of the Eu(III) ion, as previously reported. [87, 160] This Tb-to-Eu energy transfer process can be estimated by replacing the Eu ion with Gd. The emissive level of the Gd(III) ion ($^6P_{7/2}$) lies too high in energy, therefore cannot act as an acceptor to transfer to the Tb ion, therefore only lifetime values for Tb will be observed, while maintaining a similar doping concentration. Based on the lifetime values in Table 28, this energy transfer efficiency from Tb-to-Eu can be determined by the following equation [160, 202], where τ is the presence and τ_0 is the absence of Eu(III) acceptor ions.

$$E_{Tb \rightarrow Eu} = 1 - \frac{\tau}{\tau_0}$$

The intermetallic energy transfer probability from Tb(III) to Eu(III) ions is 80% and has been attributed to the phonon-assisted Förster transfer mechanism. [202-204] This result is an improvement to other 50:50 systems at 42.4% and 23.1%, although values of 92% are obtained with pyromellitic acid linkers. [193, 204] The sensitization efficiency (η_{sens}) greater than 100% in the mixed system at 617 nm can be attributed to the energy being transferred from the Tb(III) ion to the energy levels of the Eu(III) emissive center, subsequently increasing the efficiency of the system.

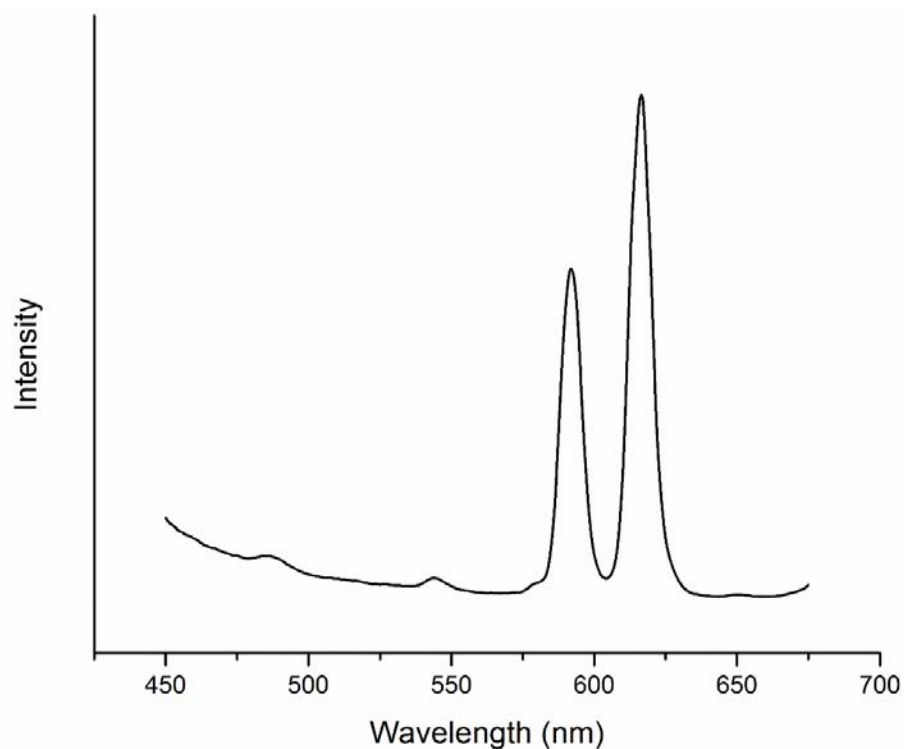


Figure 43. Emission spectrum of the Eu:Tb analog of GWMOF-6 at a 50:50 concentration ratio.

Table 28. Quantum yield and lifetime values for Eu:Tb 50:50 system at the maximum emission of Eu (545 nm) and Tb (617 nm).

Eu:Tb	Φ (%)	τ at 545 nm (ms)	τ at 617 nm (ms)
50:50	12.75 ± 3.35	0.3184 ± 0.016	0.7611 ± 0.001

6.4 Conclusion

A doped lanthanide adipate metal-organic framework was synthesized with Eu and Tb ions through hydrothermal methods with varying Gd concentrations to determine the optimal doping concentration. Photophysical measurements were performed and the highest emission intensities were from the 50:50 Ln:Gd (Ln = Eu or Tb) systems with Eu and Tb at 3.65% and 7.61%, respectively. A system synthesized with 50:50 Eu:Tb had

an energy transfer from the higher 5D_4 emissive energy level of the Tb(III) ion to the 5D_0 of the Eu(III) ion, with enhanced emission and a quantum yield of 12.8% compared to systems doped with optically inert metals. The 50:50 doping concentrations allow for optimal spacing between emissive centers to circumvent the problem of concentration quenching within the GWMOF-6 system.

CHAPTER 7: A LANTHANIDE COORDINATION POLYMER BASED ON 2,2'-BITHIOPHENE-5,5'-DICARBOXYLATE FOR NITROAROMATIC DETECTION

Coordination polymers and metal-organic frameworks have had a surge of interest in applications in sensing, particularly for nitroaromatic compounds used in explosives and their adverse effects on environmental health. [25, 205, 206] Detection methods such as capillary electrophoresis and gas chromatography have drawbacks of tedious preparation of samples, high cost of use, and sophisticated instrumentation. [207, 208] MOFs can be used as fluorescence-based sensors, which have the advantage of having high sensitivity, simplicity, short response time, and selectivity. [209] Nitroaromatics are able to be detected with low false positive rates; however, selectivity between nitroaromatic species is still an active area of research and the ability to detect on site would be invaluable. [210, 211] With these considerations in mind, a lanthanide-organic framework was synthesized with a bithiophene-based linker to detect nitroaromatic derivatives.

A new lanthanide CP based on 2,2'-bithiophene-5,5'-dicarboxylic acid (DTDC) was prepared ($[\text{Ln}_2(\text{C}_{10}\text{H}_4\text{O}_4\text{S}_2)_3(\text{H}_2\text{O})_6]_n$, Ln = Sm - Yb) for use as a chemosensor. This linker has been used in previous studies [212-216] with transition metal coordination polymers, but not with lanthanides or for applications in nitroaromatic sensing. Some thiophene-containing molecules, however, have been used to detect nitroaromatics, [217, 218] used as films for gas sensing, [219, 220] or even used to functionalize silicon-

containing aggregation-induced emission materials. [221] Thiophene-2,5-dicarboxylic acid has been used as an organic linker in both transition metal [222, 223] and lanthanide [224, 225] coordination polymers. Furthermore, to the best of our knowledge, this is the first system where a thiophene-based linker is used within a CP for the purpose of explosives detection. The nitroaromatic species studied herein include 2-nitrophenol (2-NP), 3-nitrophenol (3-NP), 4-nitrophenol (4-NP), 1,3-dinitrobenzene (DNB), 2-nitrotoluene (NT), 2-nitroaniline (NA), and 4-nitrobenzotrile (NBN). Benzene derivatives without nitro groups (Phenol; 4-methylphenol) were used as a control to test the selectivity of the title compound.

7.1 Synthesis

7.1.1 Synthesis of 2,2'-bithiophene-5,5'-dicarboxylic acid

The linker 2,2'-bithiophene-5,5'-dicarboxylic acid was synthesized according to modified literature methods (Figure 44). [226] To a solution of 550 mg (3.30 mmol) of 2,2'-bithiophene in 50 mL dry THF was added 4.4 mL (7.04 mmol) n-BuLi solution (1.6 M in hexanes) dropwise at -78 °C using a Schlenk line under an N₂ atmosphere. After stirring for four hours, the milky white solution was poured over crushed dry ice, also under an N₂ atmosphere. The light yellow suspension was allowed to warm to room temperature under mild stirring and then acidified with 2 M aqueous HCl. The resulting yellow suspension was then filtered, washed with diethyl ether, and left to dry in air at room temperature. The same synthesis using 5,5'-dibromo-2,2'-dithiophene also produced the DTDC acid moiety in similar yields. Overall yield: 64-82%. ¹H NMR (400 MHz, DMSO, ppm) δ7.70 (d, 2H), 7.54 (d, 2H). ¹³C NMR (101 MHz, DMSO, ppm) δ175.84, 163.14, 142.06, 134.95, 127.08.

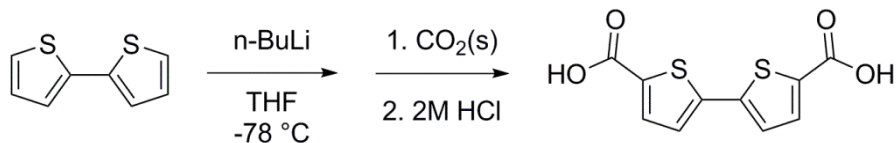


Figure 44. Synthesis of DTDC linker.

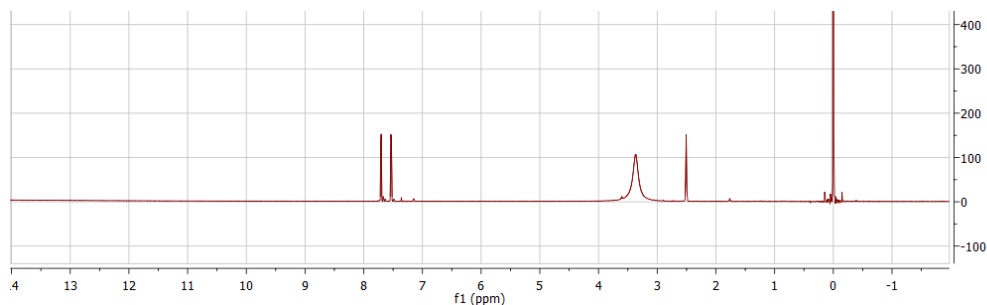


Figure 45. DTDC product ^1H NMR (400 MHz, DMSO, ppm) δ 7.70 (d, 2H), 7.54 (d, 2H).

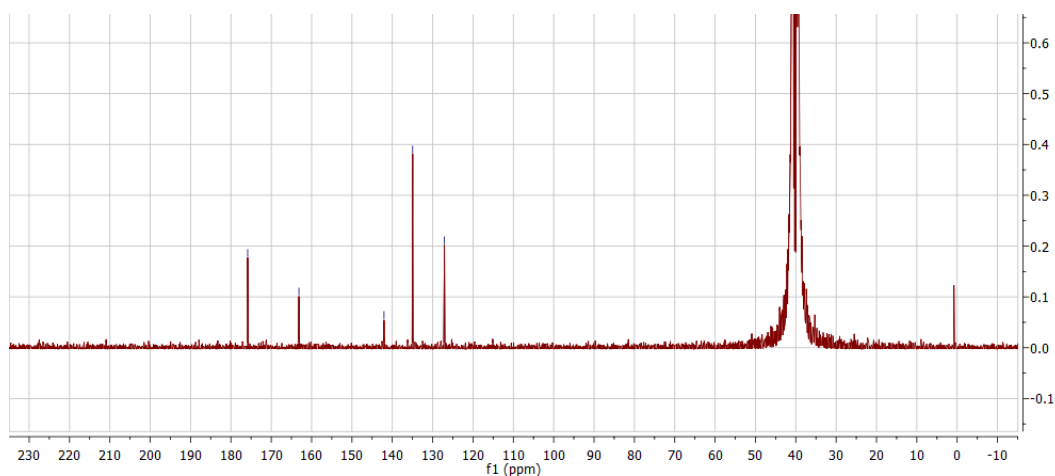


Figure 46. DTDC product ^{13}C NMR (101 MHz, DMSO, ppm) δ 175.84, 163.14, 142.06, 134.95, 127.08.

7.1.2 Synthesis of $[\text{Er}_2(\text{C}_{10}\text{H}_4\text{O}_4\text{S}_2)_3(\text{H}_2\text{O})_6]_n$

In a 23 mL Teflon lined autoclave, $\text{ErCl}_3 \cdot \text{H}_2\text{O}$ (0.20 mmol, 54 mg) and DTDC linker (0.20 mmol, 51 mg) were dissolved with DMF (7 mL) and mixed to form a clear solution. After five minutes of stirring, water (8 mL) was added turning the clear solution a cloudy yellow. The autoclave was sealed, placed in an oven, and heated under

autogeneous pressure for seven days (168 hours) at 100 °C. After cooling to room temperature, a clear, light yellow, liquid was decanted from a beige crystalline solid, which was then washed three times with water and ethanol. Similar synthetic methods were used for other isostructural CPs where Ln = Sm, Eu, Gd, Tb, Dy, Ho, Tm, Yb). Elemental analyses were conducted on Eu and Tb samples by Galbraith Laboratories, Inc., Knoxville, TN, USA. Eu: calcd. C 30.04, H 2.02, S 16.04; found C 30.04, H 2.05, S 15.59. Tb: calcd. C 52.95, H 3.26; found C 52.66, H 3.02.

7.1.3 Single crystal X-ray Diffraction

A single crystal of the Er compound was selected and mounted atop a glass fiber. Data were collected on a Bruker D8 QUEST CMOS system equipped with a TRIUMPH curved-crystal monochromator and a Mo K α fine-focus tube ($\lambda = 0.71073 \text{ \AA}$). A total of 13,358 reflections up to a maximum of 56.70° were collected of which 4584 were independent. The frames were integrated with Bruker SAINT Software package and the structure was solved with direct methods using the SHELXT-2014 package. The structure was further refined using SHELX-97 [227] within the WINGX software suite. Crystallographic details can be found in Table 30.

7.1.4 Luminescence

Emission spectra were collected using a Perkin Elmer LS55 Fluorescence Spectrometer at room temperature. In a typical experiment, 2 mg of finely ground Er-DTDC was suspended in 10 mL of ethanol and shaken for 15 minutes. The emission spectra were collected at an excitation wavelength of 371 nm with incremental additions of different nitroaromatic compound solutions (1 mM in ethanol) to 2 mL of the ethanol dispersion of Er-DTDC.

7.2 Structural Description

The Er-DTDC compound is a dense, three-dimensional CP. The following structural description will focus on that of the Er compound (Fig, Table). Other DTDC CPs (Ln = Sm, Eu, Gd, Tb, Dy, Ho, Tm, Yb) were found to be isostructural, as confirmed with powder X-ray diffraction, FTIR, and TGA. Crystals from the other Ln ions were not suitable for structural determination by single crystal diffraction methods. Disordered square antiprismatic monomers of ErO₈ are bridged to adjacent Er ions through DTDC linkers. Three of these oxygen atoms form monodentate attachments through carboxylate moieties of the linker (O1, O2, O5), two oxygen atoms form a bidentate attachment from one DTDC linker (O3, O4), and three bound aqua ligands (O7, O8, O9) are coordinated to the Er ions to saturate the coordination environment. The monomers are bridged together through DTDC in the [100] and [001] direction to afford the overall three dimensional structure.

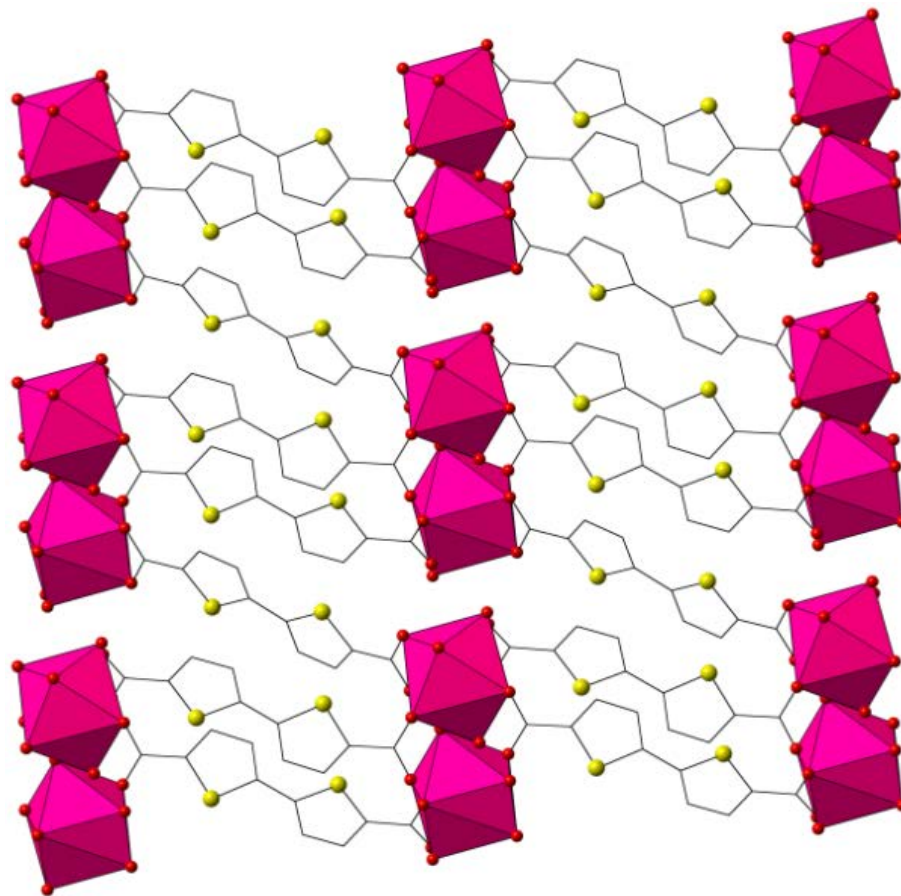


Figure 47. *View of Er-DTDC down the [100] direction. Magenta polyhedra represent Er monomers, yellow spheres are sulfur atoms, red spheres are oxygen atoms, and black lines are carbon atoms. Hydrogen atoms have been omitted for clarity.*

Table 29. Crystallographic information for the Er-DTDC CP.

Formula	[Er ₂ (C ₁₀ H ₄ O ₄ S ₂) ₃ (H ₂ O) ₆] _n
Formula weight (g/mol)	1199.42
Crystal class	Triclinic
Space group	<i>P</i> -1
<i>a</i> (Å)	7.7389(5)
<i>b</i> (Å)	9.6787(6)
<i>c</i> (Å)	13.1985(8)
<i>α</i> (°)	89.999(2)
<i>β</i> (°)	75.000(1)
<i>γ</i> (°)	75.514(2)
<i>Z</i>	2
Cell volume (Å ³)	921.62(10)
Density (mg m ⁻³)	2.1611(2)
<i>μ</i> (mm ⁻¹)	4.941
<i>R</i> _{int}	3.08%
<i>R</i> ₁	2.64%
<i>wR</i> ₂	6.07%
GOF	1.113
Total Reflections	4584

The structure contains two crystallographically unique DTDC linkers. The first DTDC coordinates to two Er ions through monodentate attachments from carboxylate oxygen (O3, O4). These linkers assist in propagating the CP in the [001] direction. The bithiophene units in this linker possess a nearly planar torsion angle of 1.16°. The second unique DTDC linker in this CP contains bridging carboxylate groups and propagates the XCP in the [100] direction. One carboxylate group in this linker bridges together Er atoms (O1, O2), while the second carboxylate group is attached in a monodentate fashion to one Er atom (O5) and the carbonyl oxygen (O6) does not participate in coordination. This linker possesses antiperiplanar torsion angles of 12.20° and 10.47° between the

thiophene units. Selected bond lengths and angles and π - π interactions can be found in Table 30 and Table 32, respectively.

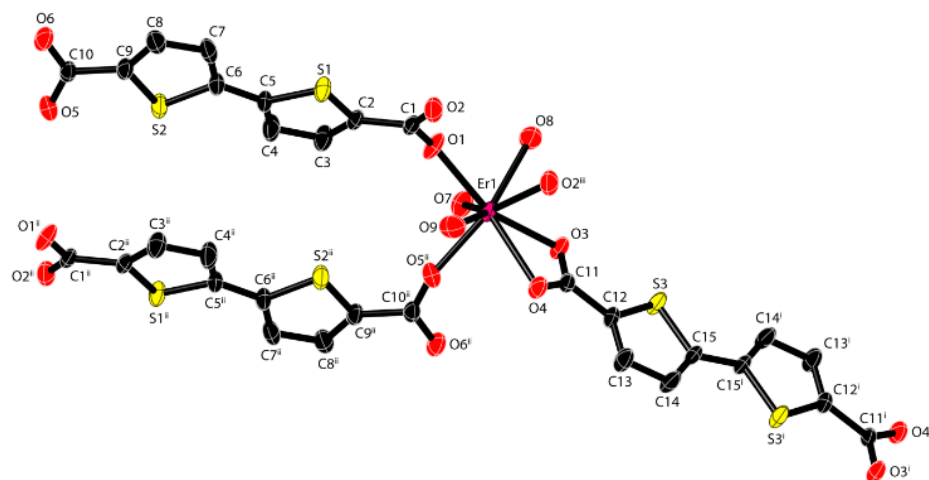


Figure 48. Thermal ellipsoid plot (50% level) of *Er-DTDC* (where superscripts indicate symmetrically generated atoms, $I = 1 - x, 2 - y, -z$; $ii = 1 - x, 1 - y, 2 - z$; and $iii = 2 - x, 1 - y, 1 - z$). Hydrogen atoms have been omitted.

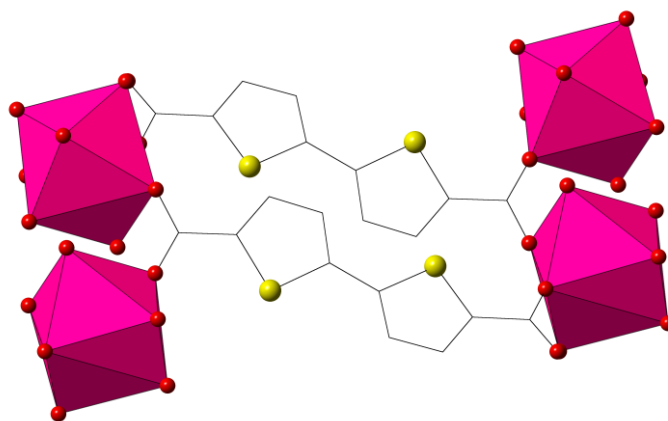


Figure 49. View of *Er-CP* down $[100]$ illustrating the bridging of the carboxylate groups connecting ErO_8 polyhedra, illustrating the monomer SBU structures.

Table 30. *Selected bond lengths for Er-DTDC.*

Er-Ox	Distance (Å)
1	2.4488
3	2.3872
4	2.4505
7	2.3534
8	2.4390
9	2.3464
2ⁱ	2.2495
5ⁱⁱ	2.2548
C1-O1	1.2573
C1-O2	1.2362
C10-O5	1.2632
C10-O6	1.2429
C11-O3	1.2682
C11-O4	1.2537

Table 31. Intermolecular interactions between neighboring centroids where Cg(1) is S(1), C(2), C(3), C(4), C(5), Cg(2) is S(2), C(6), C(7), C(8), C(9), and Cg(3) is S(3), C(12), C(13), C(14), C(15).

Centroid	Distance (Å)
Cg(1)-Cg(1)	4.4431
Cg(1)-Cg(1)	5.3538
Cg(1)-Cg(2)	3.7965
Cg(1)-Cg(2)	5.5982
Cg(1)-Cg(3)	4.8569
Cg(2)-Cg(3)	5.2304
Cg(2)-Cg(3)	5.7014
Cg(3)-Cg(1)	5.1727
Cg(3)-Cg(1)	5.3664
Cg(3)-Cg(2)	5.2574
Cg(3)-Cg(2)	5.4506

7.3 Luminescence and Sensing Properties

The emission spectrum of Er-DTDC in ethanol ($\lambda_{\text{exc}} = 371$ nm) shows a maximum emission peak at 438 nm (Figure 50) while the uncoordinated DTDC molecule shows a maximum emission at 440 nm, and are assigned to the π - π^* transition. [228] This shift can be attributed to the rigidity on the DTDC upon CP formation. [187, 229]

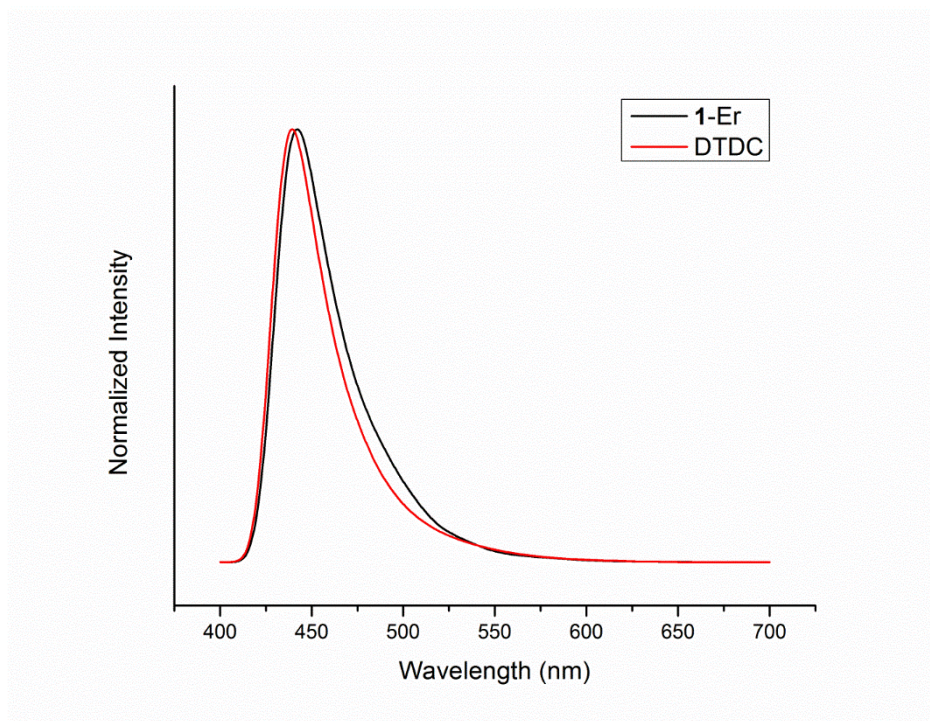


Figure 50. Emission spectra of Er-DTDC and the DTDC linker in ethanol ($\lambda_{exc} = 371$ nm).

Fluorescence quenching titrations of Er-DTDC using nitroaromatic derivatives were performed in ethanol (Figure 51). The fluorescence quenching efficiency was calculated using $[(I_0 - I)/I_0] \cdot 100\%$ monitoring emission at 440 nm upon photoexcitation at 371 nm, [230] and quenching was most efficient with compounds containing nitro groups (NA > 2-NP > 4-NP > 3-NP > DNB > NT > NBN), as molecules without this moiety such as phenol and 4-methylphenol significantly shows less luminescence quenching compared to the nitro-containing species (Figure 52, Table 33).

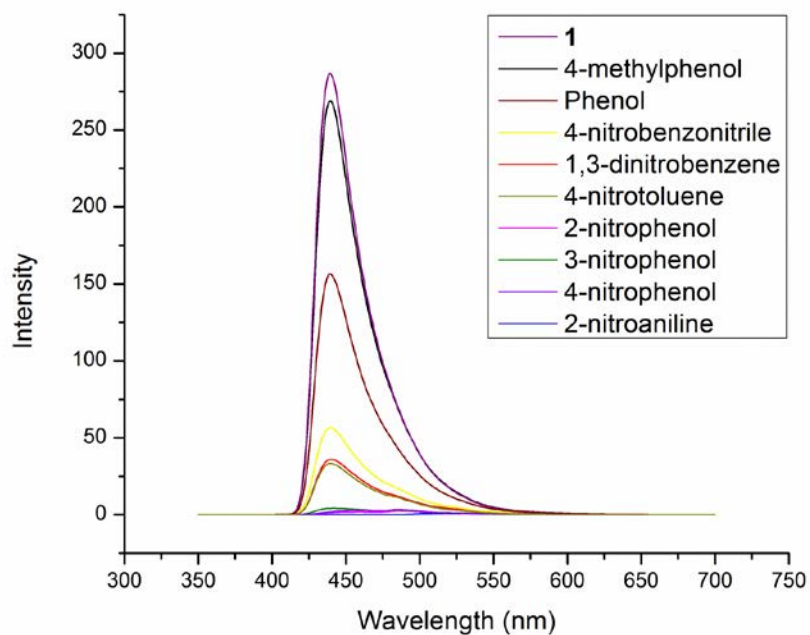


Figure 51. Emission spectrum of Er-DTDC and additions of analytes at 1 mM concentration, excited at 371 nm.

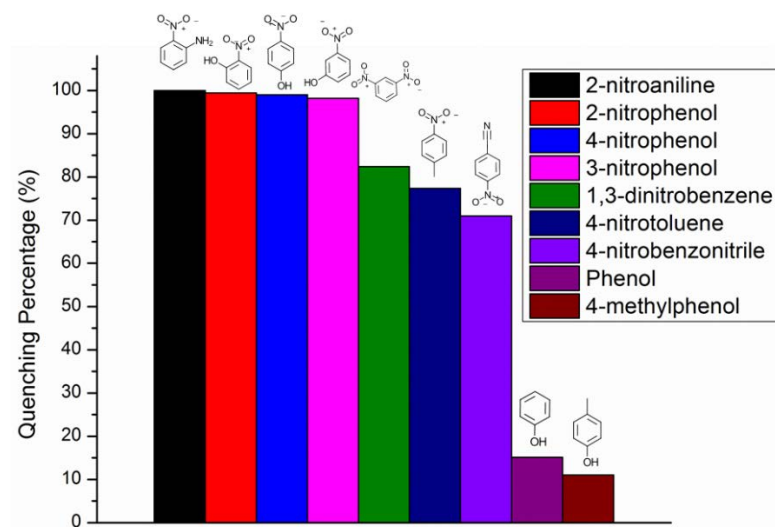


Figure 52. Percentage of photoluminescence quenching of Er-DTDC upon addition of analytes.

This quenching of emission attributed to the DTDC linker within the CP is due to the highly electron deficient nature of the nitroaromatic molecules. [25, 205] Upon excitation, electron transfer from the π -rich DTDC electron donor to the electron deficient nitroaromatic moieties occurs, resulting in oxidation of the excited state and quenching of the luminescence. The phenol and 4-methylphenol do not contain these withdrawing groups, and do not as readily influence the emission of Er-DTDC.

The process of quenching within this system can be attributed to the relative energies of the LUMOs of DTDC and the analytes (Figure 54, Table 33). [209, 231] When irradiated, an electron is promoted from the HOMO of DTDC to its LUMO, and this excited electron can be subsequently transferred to the LUMO of the analyte, resulting in fluorescence quenching. The LUMO of DTDC is within ± 0.38 eV for analytes that exhibit almost complete fluorescence quenching (NA, 2-NP, 3-NP, 4-NP) and within 0.71 eV for analytes that quench $\sim 75\%$ fluorescence (DNB, NT, NBN, Table 33). Phenol and 4-methylphenol have LUMO energies well above the LUMO of DTDC at +2.52 and 2.54 eV, respectively. This energy difference is too high for an electron to be transferred for quenching.

Table 32. *Quenching rates and efficiencies of nitroaromatic analytes with Er-DTDC in ethanol.*

Analyte	Quenching efficiency (%)	K_{SV} (M^{-1})
4-nitrotoluene (4-NT)	77.8	419.31
1,3-dinitrobenzene (DNB)	82.4	176.98
2-nitroaniline (NA)	100	23,137
4-methylphenol (MP)	11.0	NA
Phenol	15.1	NA
4-nitrobenzotrile (NBN)	71.5	106.93
2-nitrophenol (2-NP)	99.4	5,729.56
3-nitrophenol (3-NP)	98.2	4,879.23
4-nitrophenol (4-NP)	99.0	1,179.02

The order of quenching is not in full agreement with the LUMO energies of all the analytes. One possibility for this discrepancy is a resonance energy transfer mechanism. [205, 232] The absorption spectra of the different aromatic analytes in ethanol were compared to the emission spectrum of Er-DTDC dispersed in ethanol (Figure 53). The overlap seen between NA and Er-DTDC demonstrated the probability of resonance energy transfer between the emission bands of Er-DTDC and the absorption band of NA. Minimal overlap is observed in the absorption spectra 2-NP, 3-NP, and 4-NP systems with the emission of Er-DTDC, indicating that this quenching mechanism is less probable within these systems, with the main method of quenching from LUMO to LUMO electron transfer discussed previously. No overlaps were seen with other systems, suggesting no resonance energy transfer occurs between Er-DTDC and the inefficient quenchers.

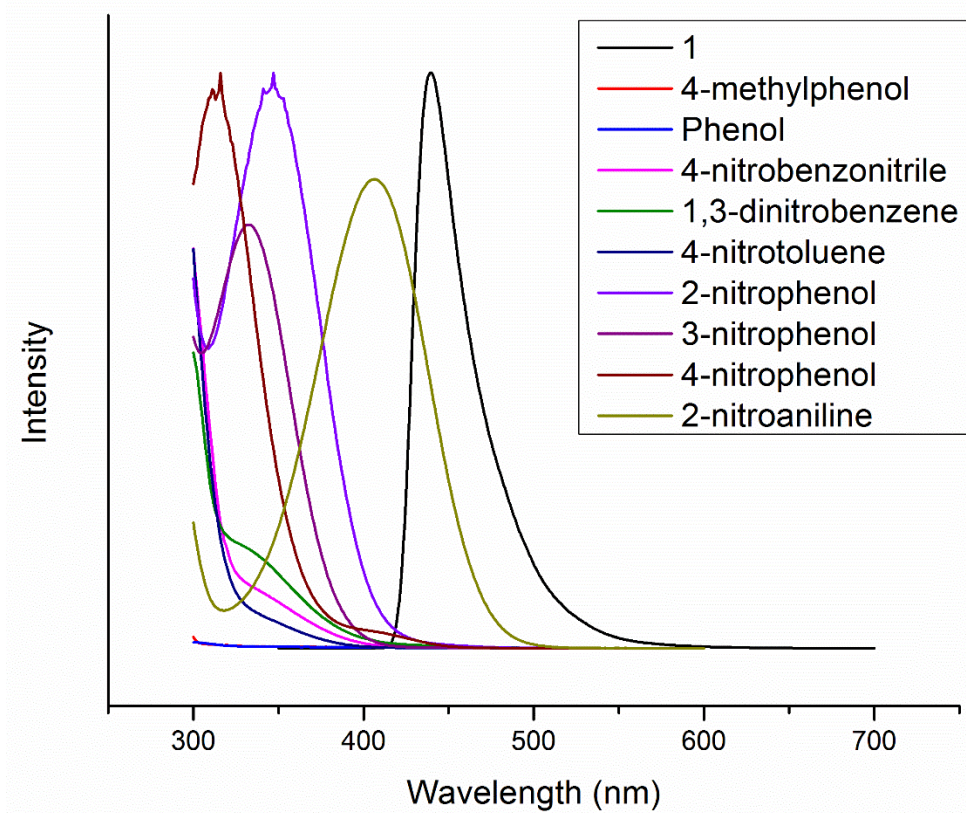


Figure 53. Spectral overlap between the absorption of aromatic analytes and the emission of Er-DTDC in ethanol.

Quenching values can also be corroborated with the energy difference between the HOMO and LUMO of the analytes. Energies were obtained through TD-DFT calculations (B3LYP level of theory using the 6-31G basis set) using the Gaussian [233] program (Table 33). For systems with ~99% quenching, the energy differences range from 4.06 to 4.71 eV while slightly less efficient systems range from 4.92 to 5.09 eV, meanwhile inefficient quenchers have HOMO/LUMO energy differences greater than 5.8 eV.

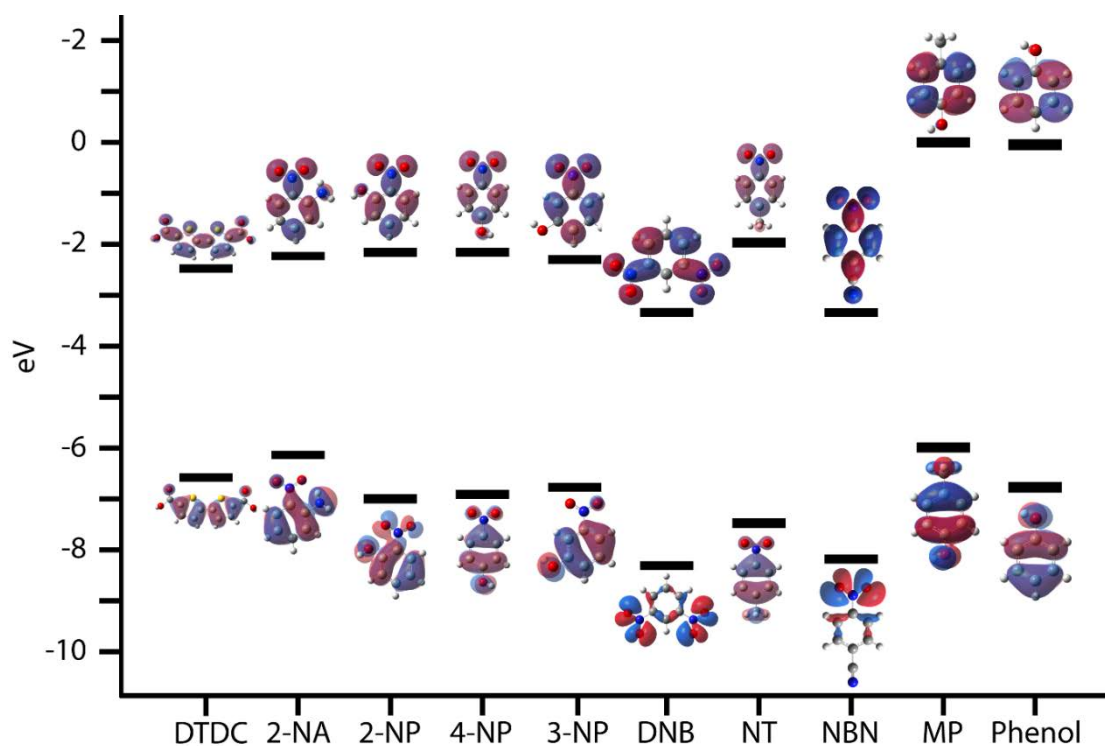


Figure 54. *HOMO and LUMO energy levels of the DTDC linker and nitroaromatic analytes, as well as representations of these molecular orbitals. These compounds are ordered in decreasing quenching ability.*

Table 33. *HOMO and LUMO energies calculated for DTDC linker and analytes.*

Analyte	HOMO (eV)	LUMO (eV)	Energy Gap (eV)
DTDC	-6.7070	-2.6082	4.0988
4-nitrotoluene (4-NT)	-7.4573	-2.3704	5.0869
1,3-dinitrobenzene (DNB)	-8.4170	-3.3191	5.0979
2-nitroaniline (NA)	-6.4548	-2.3946	4.0602
4-methylphenol (MP)	-5.9155	-0.0587	5.8568
Phenol	-6.7070	-0.0810	6.6260
4-nitrobenzotrile (NBN)	-8.1489	-3.2278	4.9211
2-nitrophenol (2-NP)	-7.0129	-2.2989	4.7140
3-nitrophenol (3-NP)	-6.7814	-2.3930	4.3884
4-nitrophenol (4-NP)	-6.9210	-2.2210	4.7000

The quenching efficiencies were further investigated through Stern-Volmer (SV) plots using the equation $I_0/I = K_{SV}[Q] + 1$, where I_0 is the initial luminescence intensity of Er-DTDC without any analyte, I is the luminescence intensity in the presence of analyte, K_{SV} is the quenching constant (M^{-1}), and $[Q]$ is the molar concentration of the analyte. The quenching constant for 4-NP, for example, was found to be $1190.80 M^{-1}$, from a linear fitting of the SV plot at low concentration ranges from 0 to $300 \mu M$ (Figure 55). At higher concentrations, deviation from linearity was seen, attributed to self-absorption and static or dynamic quenching processes. [205, 209] See Table 33 for quenching rates of all analytes.

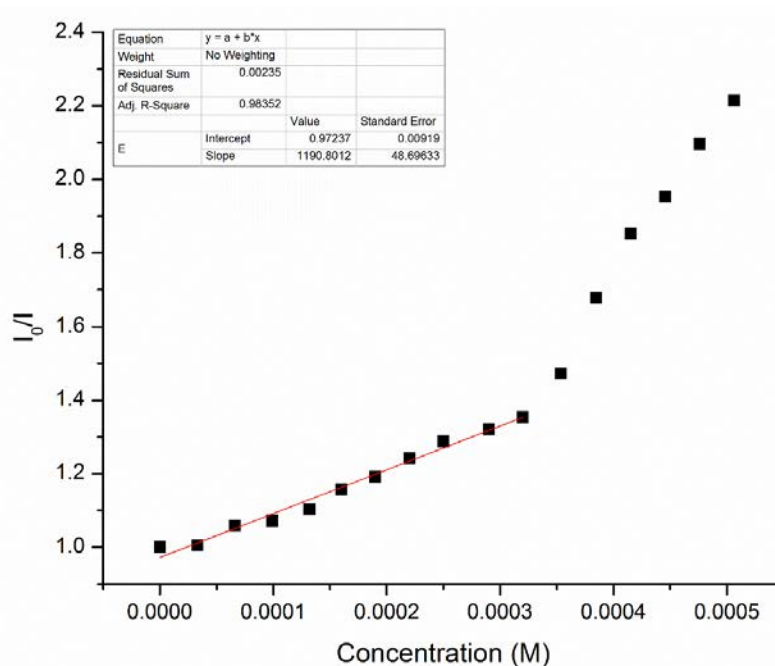


Figure 55. Stern-Volmer plot of Er-DTDC in ethanol with 1 mM 4-nitrophenol 5 μL increments at an excitation wavelength of 371 nm.

7.4 Conclusion

A new three dimensional coordination polymer comprised of 2,2'-bithiophene-5,5'-dicarboxylic acid was solvothermally synthesized and characterized using single crystal X-ray diffraction, PXRD, and luminescence measurements. The emission of this compound is linker based and is quenched upon addition of nitroaromatic species due to a charge transfer quenching from the CP to the nitroaromatic. This work demonstrates the utility of lanthanide-organic frameworks based on a bithiophene scaffold in advancing the field of explosives detection.

CHAPTER 8: RETICULAR CHEMISTRY AND SECONDARY BUILDING UNIT
FORMATION IN TRIVALENT LANTHANIDE SYSTEMS UNDER
HYDROTHERMAL CONDITIONS

One feature that allows MOFs and CPs to stand out is the ability to target pore sizes, shapes, and surface properties through reticular synthesis. [2, 4, 234, 235] This approach works well in transition metal (TM) systems, where bonding is directional and primarily dictated by the d-orbitals. [35, 36] In lanthanide systems, however, the contracted nature of the f-orbitals gives rise to primarily electrostatic bonding, where ligand bonding is largely determined by ligand steric considerations. This, combined with large ionic radii, results in lanthanide complexes with large coordination numbers (8 and 9 being the most common). As a consequence of ionic bonding, no geometric restrictions are imparted upon lanthanide coordination, therefore lanthanide ions will tend to have their coordination spheres fully saturated unless ligand sterics block available coordination sites. These traits, while apparently cumbersome, allow the diverse structural motifs seen only in lanthanide coordination polymers.

The most widely used linker in coordination polymers (both in transition metal and lanthanide systems) is arguably terephthalic acid (1,4-benzenedicarboxylic acid). This multifunctional linker exhibits a wide range of coordination modes and is seen in 1-, 2-, and 3-dimensional CPs. [236-240] The extensive use of this linker is attributed to many favorable features it possesses. One feature includes a delocalized π system, giving

the potential for π - π stacking interactions. Furthermore, chelating carboxylate groups, which can coordinate to metals in a myriad of configurations, can facilitate bridging of adjacent metal ions through one carboxylate group or bridge longer distances through the para carboxylic acid group on the benzene ring. This versatility, along with a large library of structures previously synthesized makes this linker an excellent candidate for reticular syntheses. [240]

Favorable reaction conditions have been explored previously, for the MOF-5 system only, in transition metal systems. [241] McKinstry and coworkers mapped formation diagrams with respect to time and temperature for stirred and unstirred conditions. It was determined that MOF-5 can be formed at high concentrations, making scale up reactions feasible. Other groups report zinc nitrate and zinc acetate produce a pure phase MOF-5, indicating that the metal counter ion may play a role in MOF formation. [242] No studies have been performed on lanthanide coordination polymer systems with terephthalic acid to determine optimal formation under hydrothermal conditions.

To this end, a systematic study has been performed with a representative Ln ion (Pr(III)) and terephthalic acid. Synthetic parameters such as time, temperature, fill volume, and concentration/ratio of the metal and linker were changed; the resulting solids characterized with powder X-ray diffraction to determine optimal parameters for CP formation. These findings will further refine reticular synthesis in Ln CPs and increase the understanding of what conditions are favorable for CP formation.

8.1 Synthesis and Characterization

All compounds for this study were synthesized in a similar manner using hydrothermal methods. In a typical synthesis, PrCl_3 (19 mg to 187 mg, 0.05 mmol to 0.50 mmol) and terephthalic acid (9 mg to 83 mg, 0.05 to 0.50 mmol) were added to a 23 mL Teflon-lined autoclave. Water (3 or 5 mL) was added and the autoclave was sealed. The vessel was placed in an oven at 120, 150, or 180 °C for 3 to 7 days (72 to 168 hours) at which point the autoclave was removed from the oven and left to naturally cool to room temperature. The solids were isolated by decanting the supernatant, washed twice with water and ethanol, and allowed to air dry at room temperature.

All samples were structurally characterized using powder X-ray diffraction with an Olympus BTX II Bench XRD using Co $K\alpha$ ($\lambda = 1.79 \text{ \AA}$) radiation. Diffractograms were compared to those of the terephthalic acid-based structures in the Cambridge Structural Database (CSD) to identify reaction products.

8.2 Investigation into Hydrothermal Conditions

8.2.1 Contour Plots

A systematic study was performed by changing one synthetic parameter at a time between time, temperature, and concentration; the resulting reaction was then analyzed with powder X-ray diffraction (if solids present) to determine if a coordination polymer formed. Results were reported if the terephthalic acid recrystallized, if no reaction occurred, or CP formation was observed. The syntheses that yielded a coordination polymer had their powder diffraction patterns matched to entries in the CSD. The entire data set (both CPs and null results) were tabulated and contour graphs were produced.

First, comparisons between linker and lanthanide concentrations were considered (Figure 56). Previous works have shown concentration to be a key factor in CP formation, with the metal concentration being more significant than linker concentration. [243, 244] From Figure 56, recrystallized terephthalic acid linker is the preferable outcome at any linker concentration between 0.04 and 0.10 M. The metal concentration, however, does seem to influence formation of solids. Here, very low or very high concentrations (<0.02 M and >0.06 M) lead to no reaction occurring.

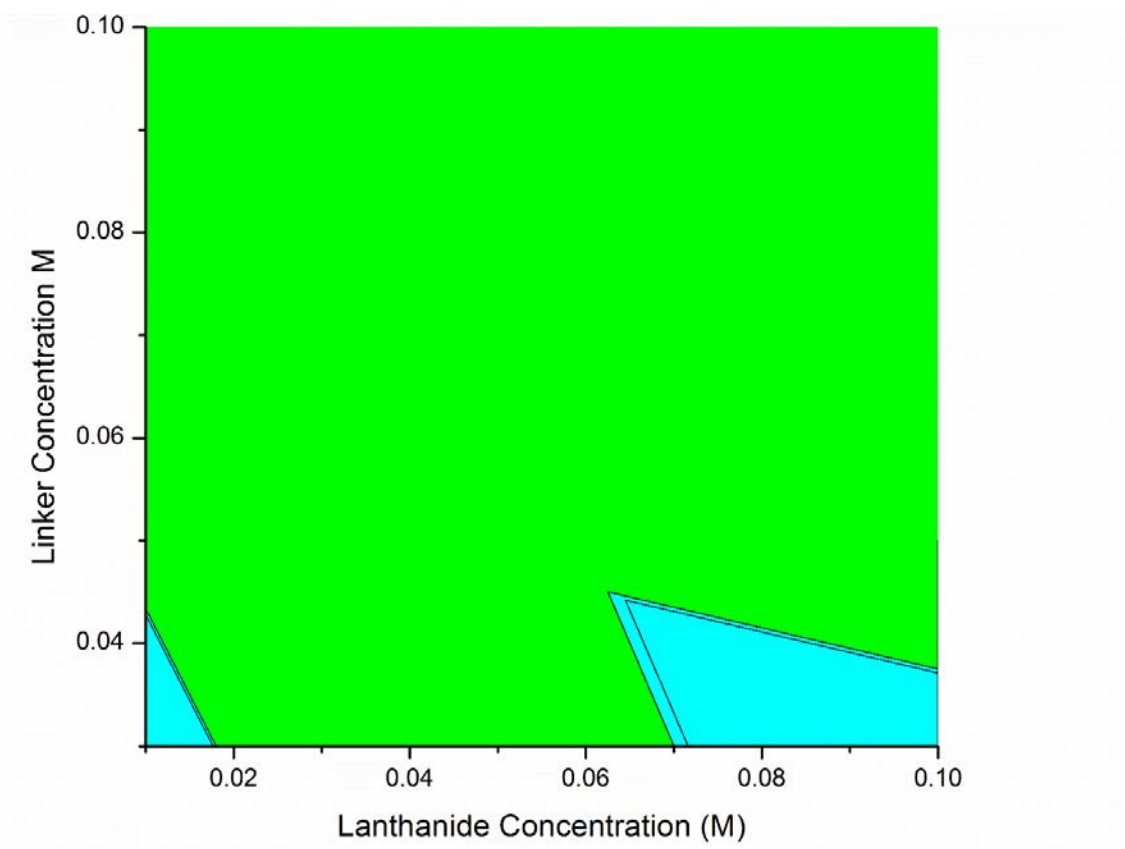


Figure 56. *Linker versus lanthanide concentration contour plot obtained from hydrothermal methods. Here, light blue is no reaction and green is recrystallized linker (terephthalic acid).*

If the concentration of the lanthanide or linker are studied compared to that of temperature (Figure 57 and Figure 58), there are “zones” in which no reaction can occur. In studying the lanthanide concentration, a narrower zone at low temperatures is seen from 0.04 M to 0.08 M in which recrystallized linker forms. If the concentration is below or above these values, no reaction occurs. When the temperature is increased, the area of recrystallized linker increases to 0.03 M to 0.10 M at 150 °C to nearly the complete range studied at 180 °C. In the linker-based system, a similar trend is seen, where recrystallized linker is observed at 120 °C at a concentration range of 0.04 M to 0.10 M. Again, increasing the temperature increases the area that recrystallized linker can occur to the full range at 180 °C.

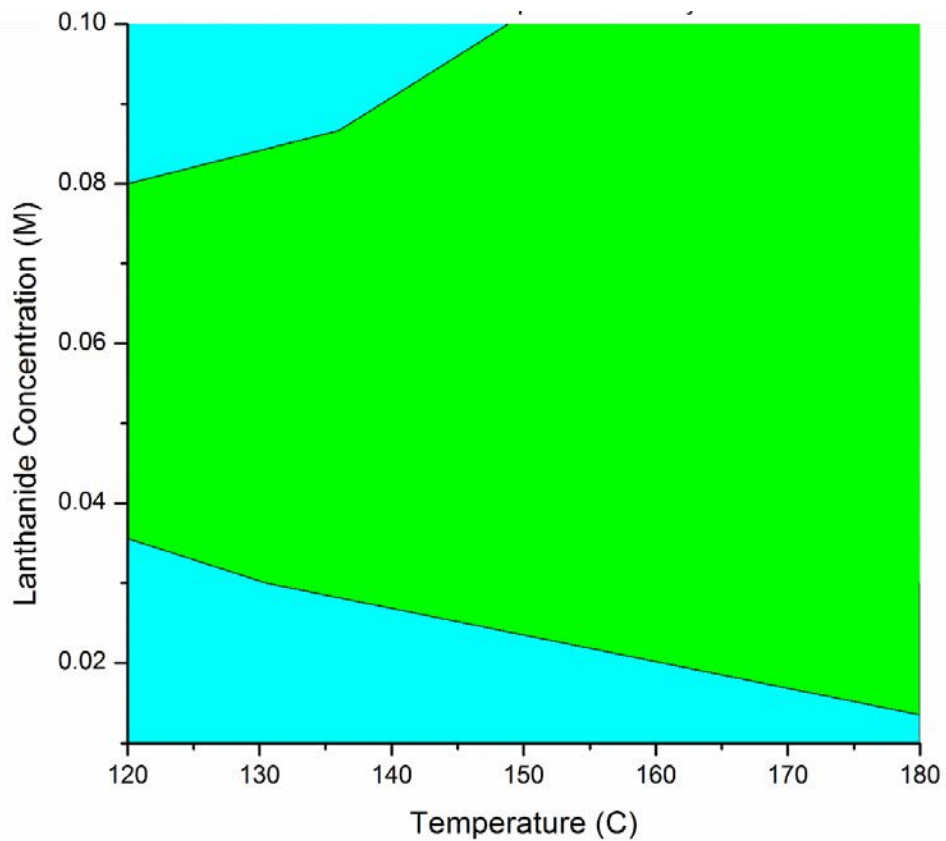


Figure 57. *Lanthanide concentration versus temperature contour plot using hydrothermal methods. Here, light blue is no reaction and green is recrystallized linker (terephthalic acid).*

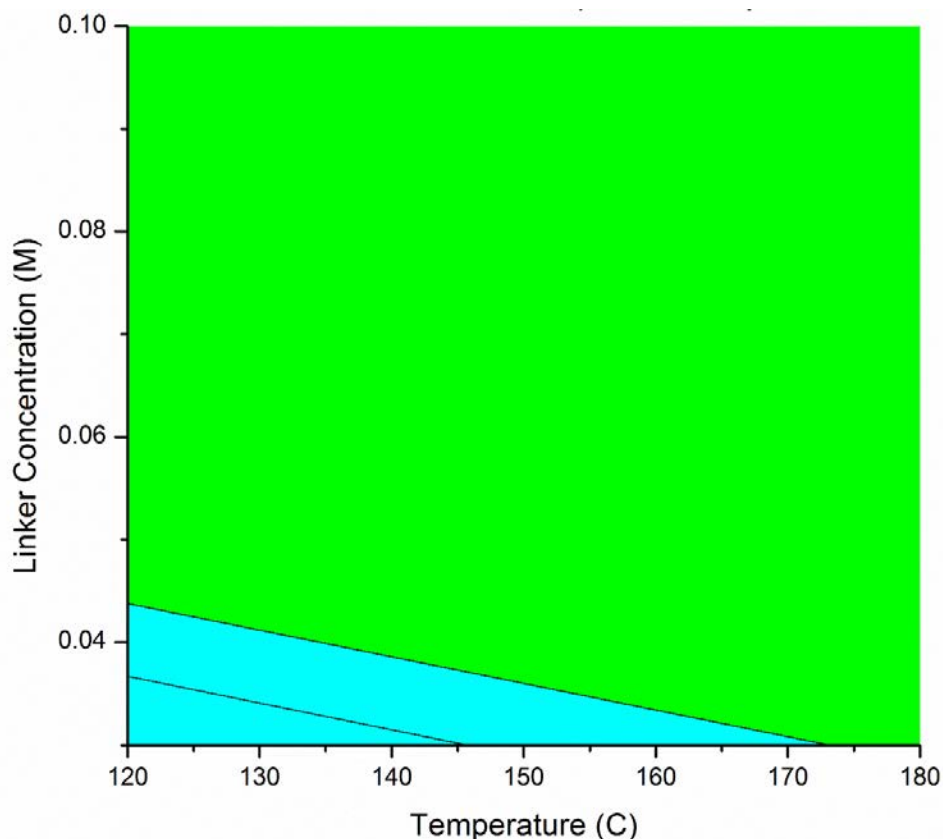


Figure 58. *Linker concentration versus temperature contour plot using hydrothermal methods. Here, light blue is no reaction and green is recrystallized linker (terephthalic acid).*

If lanthanide (Figure 59) and linker (Figure 60) concentrations are compared to time of the reaction, there is a “goldilocks” zone where CP formation is observed. In the lanthanide and time scenario, a minimum of three days is required before CP formation is observed. After five days of reaction time recrystallized terephthalic acid is the result instead. Three days has the highest probability of CP formation with varying lanthanide concentrations. In this three day reaction time period, concentrations of lanthanide ranging from 0.03 M to 0.07 M can produce a unique structure **1** (Figure 63). This concentration range narrows significantly after three days to a range of 0.05 M to 0.06 M

at 3.5 days to ~ 0.050 M at greater than four days. The fifth day of the reaction time only produces recrystallized linker regardless of lanthanide concentration.

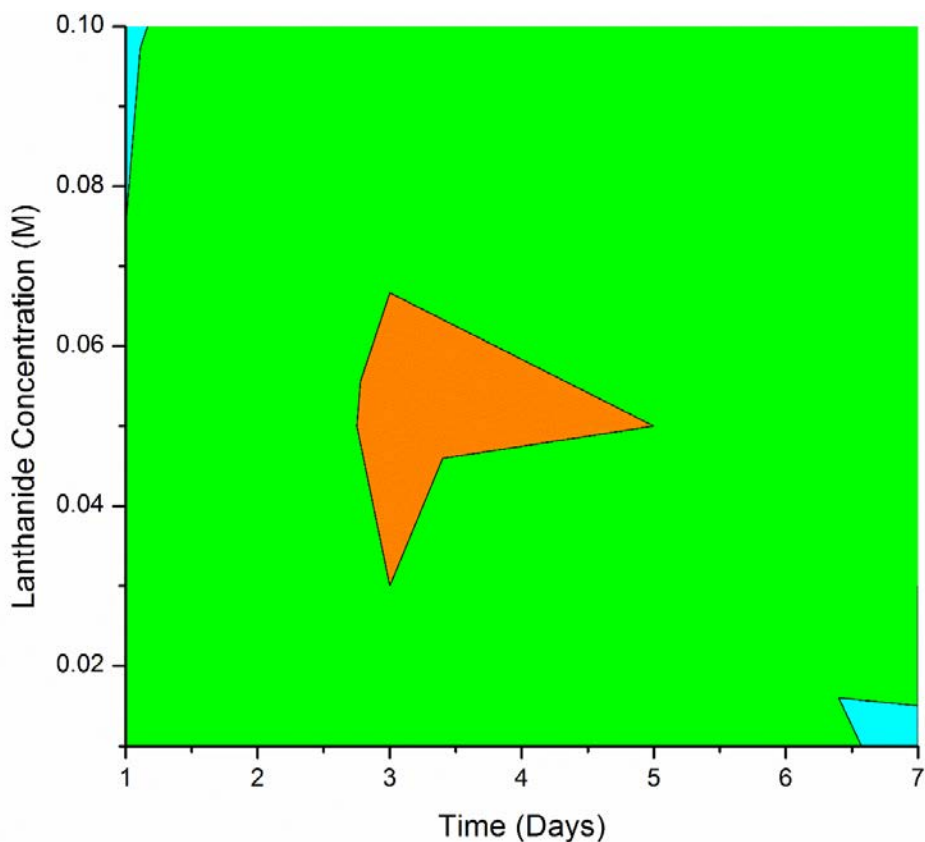


Figure 59. *Lanthanide concentration versus time contour plot from hydrothermal methods. Here, light blue is no reaction, green is recrystallized linker (terephthalic acid), and orange is compound 1.*

When considering linker concentration and time, high concentrations of linker (>0.08 M) can lead to formation of **1**, where lower concentrations of linker produced no product regardless of time. Beginning at 2.5 days, CP formation is observed at 0.10 M terephthalic acid concentration, with the lowest concentration needed at 0.08 M being between three and four days. Immediately after four days of reaction time, no product is observed and only recrystallized linker is produced

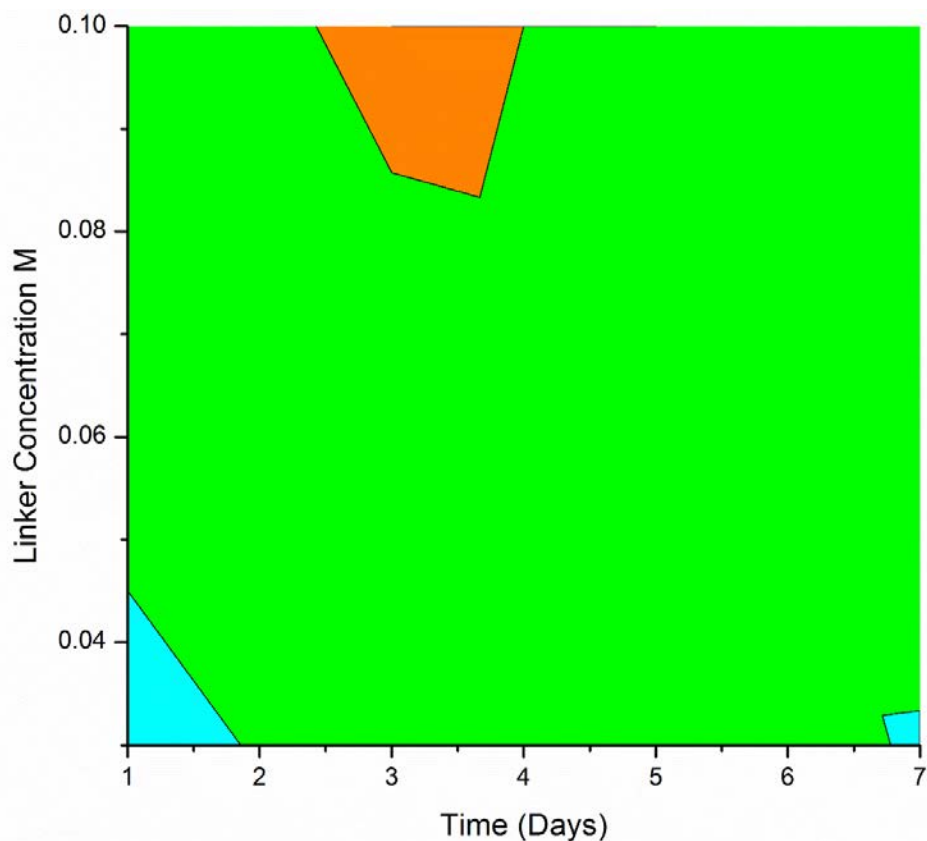


Figure 60. Linker concentration versus time contour plot from hydrothermal methods. Here, light blue is no reaction, green is recrystallized linker (terephthalic acid), and orange is compound **1**.

Next, the lanthanide and linker concentration were examined as a ratio compared to temperature (Figure 61) and time (Figure 62). A lanthanide to linker concentration ratio of 0.5 gives compound **1** regardless of the temperature range observed (120 to 180 °C). Any ratio outside this range produces either no reaction or recrystallized linker. The ratio compared to time also illustrates a zone of product(s) formation. At a ratio of 0.4 to 0.6 produces product **1** from one and a half days to seven days; however, from 2.5 to four days at a ratio of 0.5, compounds **2** and **3** form (Figure 64 and Figure 65). Any ratio

above 0.6, below 0.3, or before two days yields no reaction or produces recrystallized linker.

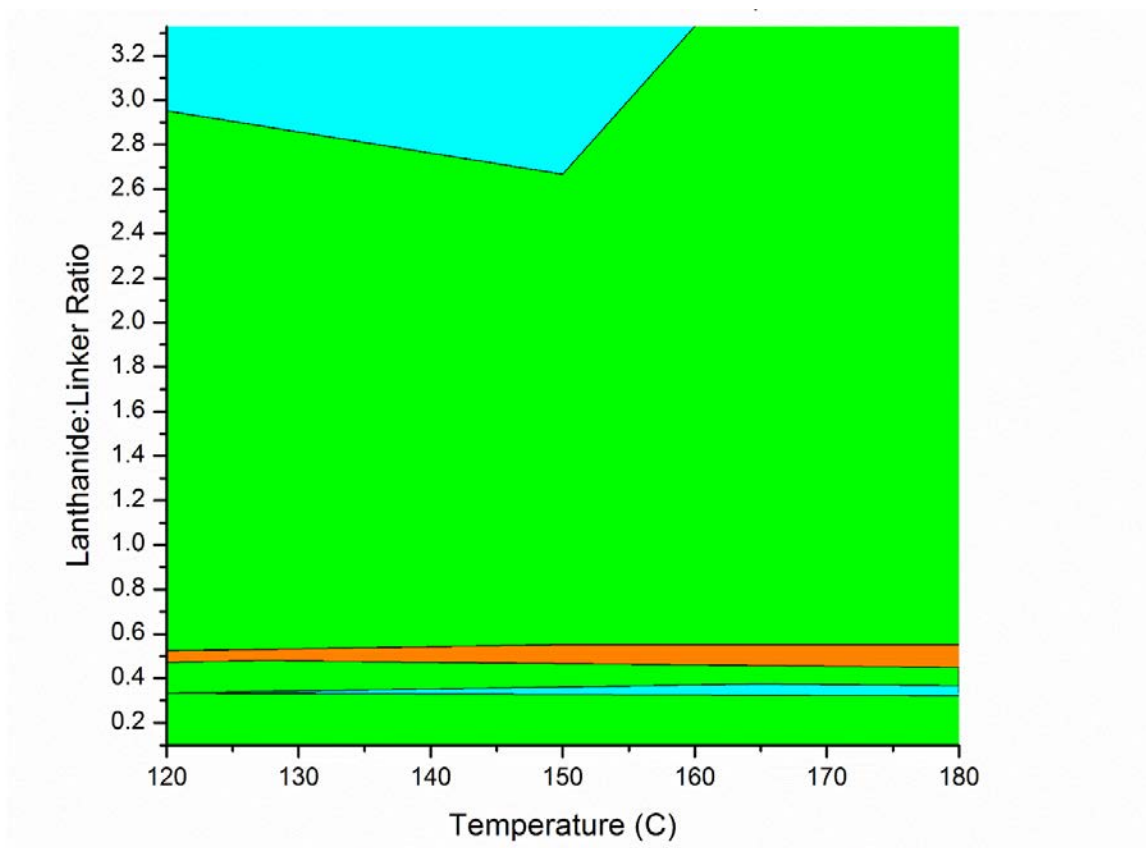


Figure 61. Lanthanide to linker concentration ratio versus temperature contour plot from hydrothermal methods. Here, light blue is no reaction, green is recrystallized linker (terephthalic acid), and orange is compound **1**.

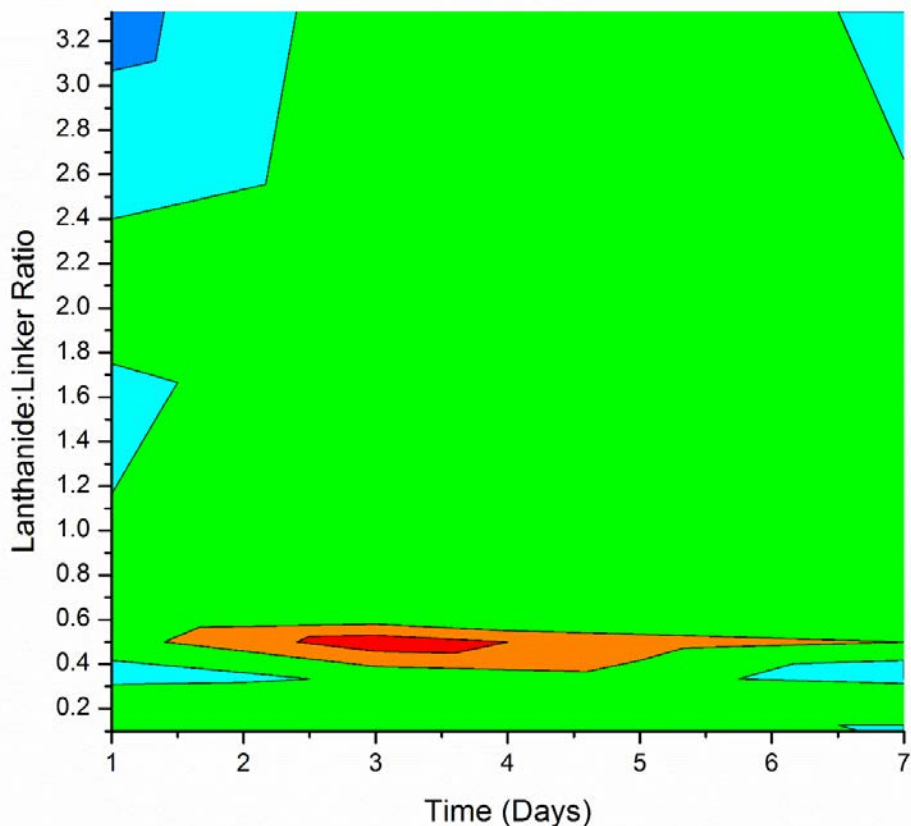


Figure 62. *Lanthanide to linker concentration ratio versus time contour plot from hydrothermal methods. Here, light and dark blue are no reaction, green is recrystallized linker (terephthalic acid), orange is compound 1, and red is a mixture of compounds 2 and 3.*

8.2.2 Matched Crystal Structures

The syntheses described above produced three unique coordination polymers. From the Cambridge Structural Database, these are AMIXIE (1) [245], NELRAY (2), and NERMON (3). [237]

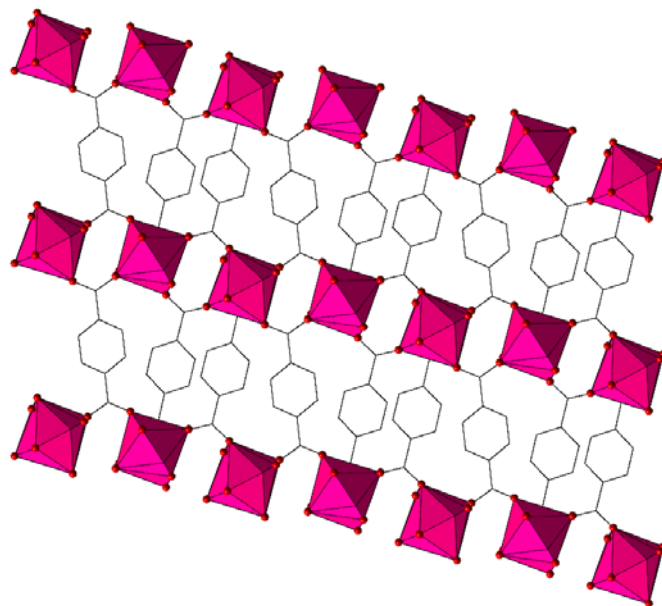


Figure 63. View of the AMIXIE (1) structure down the [100] direction. Here, pink polyhedra are Er atoms, red spheres are oxygen atoms, and black lines are carbon atoms.

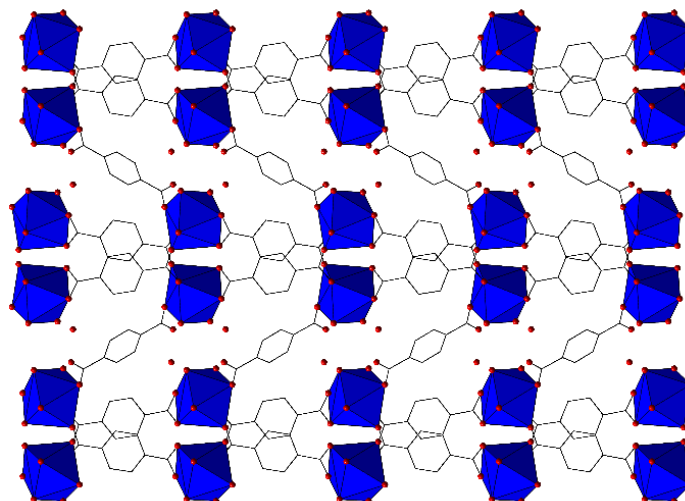


Figure 64. View of NELRAY (2) structure down the [100] direction. Here, blue polyhedra are Er atoms, red spheres are oxygen atoms, and black lines are carbon atoms.

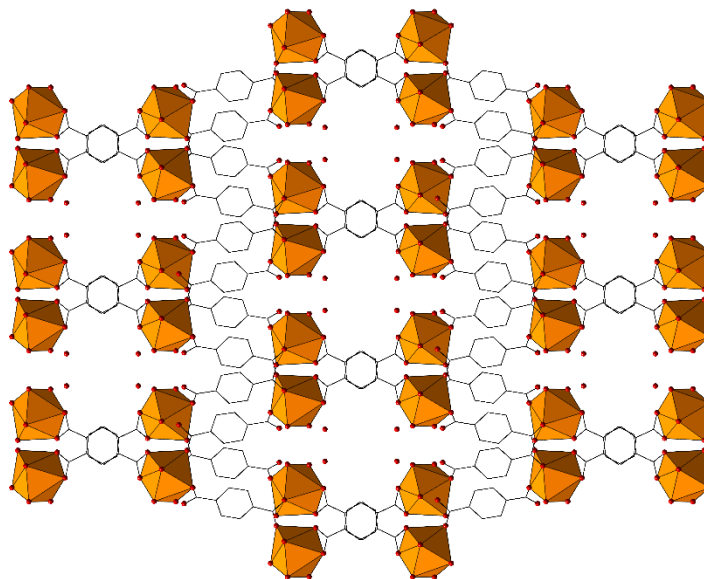


Figure 65. View of NERMON (**3**) structure down the [001] direction. Here orange polyhedra are Er atoms, red spheres are oxygen atoms, and black lines are carbon atoms.

Of the possible three CPs formed, there are some striking similarities between the structures (Table 35). All three compounds have LnO₈ coordination polyhedra, which form two dimensional Ln-O sheets with the aid of the terephthalic acid linker. The crystal class of **1** (triclinic) is different than that of **2** and **3** (monoclinic). Furthermore, the space groups are different between all compounds (compound **1** (*P*-1), **2** (*P*2₁/2), and **3** (*C*2/c)).

Table 34. *Crystal data of compounds 1 – 3.*

Formula	Er₂(BDC)₃(H₂O)₄	Er₂(BDC)₃(H₂O)₆·2H₂O	Er₂(BDC)₃(H₂O)₆·2H₂O
Formula weight	449.46	971.32	971.32
Crystal class	Triclinic	Monoclinic	Monoclinic
Space group	<i>P</i> -1	<i>P</i> 2 ₁ /2	<i>C</i> 2/c
a (Å)	6.1356(3)	6.7429(2)	38.5123(13)
b (Å)	9.9896(5)	22.4913(7)	11.1241(4)
c (Å)	10.170(5)	9.6575(3)	7.0122(2)
α (°)	102.170(3)	90	90
β (°)	91.433(4)	91.6400(18)	98.634(2)
γ (°)	58.737(5)	90	90
Z	2	4	4

Now that an initial set of parameters are obtained for favorable coordination polymer formation, expanding this research to encompass more metal and linker systems is needed. Further work on this project includes expanding systems to different linkers (both rigid and flexible), different metals (lanthanide, transition metal, and alkaline earth metals) and base modification.

8.3 Conclusion

The understanding of the synthesis of lanthanide coordination polymers is an active area of research due to the difficulty in predicting the resulting product as a result of the radially contracted f orbitals of the lanthanide ion. It was found that favorable reaction conditions include a time of three to five days at temperatures ranging from 120 to 180 °C. The favorable concentrations of the reagents are 0.05 M for the lanthanide ion and 0.1 M for the linker, forming an optimal ratio of 0.5 lanthanide to linker. These results discussed above will assist in laying the groundwork for refining reticular

synthesis in lanthanide coordination polymers and increase the understanding of what conditions are optimal for coordination polymer formation.

REFERENCES

1. Deng, H., et al., *Large-Pore Apertures in a Series of Metal-Organic Frameworks*. Science, 2012. **336**(6084): p. 1018-1023.
2. Furukawa, H., et al., *The Chemistry and Applications of Metal-Organic Frameworks*. Science, 2013. **341**(6149).
3. Furukawa, H., et al., *Ultrahigh Porosity in Metal-Organic Frameworks*. Science, 2010. **329**: p. 424-428.
4. Li, H., et al., *Design and synthesis of an exceptionally stable and highly porous metal-organic framework*. Nature, 1999. **402**: p. 276-279.
5. Rowsell, J.L.C. and O.M. Yaghi, *Effects of Functionalization, Catenation, and Variation of the Metal Oxide and Organic Linking Units on the Low-Pressure Hydrogen Adsorption Properties of Metal–Organic Frameworks*. Journal of the American Chemical Society, 2006. **128**(4): p. 1304-1315.
6. Yaghi, O.M. and Q. Li, *Reticular chemistry and MOFs for clean energy*. MRS Bulletin, 2009. **34**: p. 682-690.
7. Lin, W., *Homochiral porous metal-organic frameworks: Why and how?* Journal of Solid State Chemistry, 2005. **178**(8): p. 2486-2490.
8. Uemura, T., et al., *Radical polymerisation of styrene in porous coordination polymers*. Chemical Communications, 2005(48): p. 5968-5970.

9. Fletcher, A.J., K.M. Thomas, and M.J. Rosseinsky, *Flexibility in metal-organic framework materials: Impact on sorption properties*. Journal of Solid State Chemistry, 2005. **178**(8): p. 2491-2510.
10. Ferey, G., *Microporous Solids: From Organically Templated Inorganic Skeletons to Hybrid Frameworks...Ecumenism in Chemistry*. Chemistry of Materials, 2001. **13**(10): p. 3084-3098.
11. Rao, C.N.R., S. Natarajan, and R. Vaidhyanathan, *Metal carboxylates with open architectures*. Angewandte Chemie International Edition, 2004. **43**(12): p. 1466-1496.
12. Yaghi, O.M., et al., *Reticular synthesis and the design of new materials*. Nature, 2003. **423**: p. 705-714.
13. Janiak, C., *Engineering coordination polymers towards applications*. Dalton Transactions, 2003(14): p. 2781-2804.
14. Batten, S.R., et al., *Terminology of metal-organic frameworks and coordination polymers (IUPAC Recommendations 2013)*. Pure and Applied Chemistry, 2013. **85**(8): p. 1715-1724.
15. Jung, S., et al., *Bio-functionalization of metal-organic frameworks by covalent protein conjugation*. Chemical Communications, 2011. **47**(10): p. 2904-2906.
16. Bobbitt, N.S., J. Chen, and R.Q. Snurr, *High-Throughput Screening of Metal–Organic Frameworks for Hydrogen Storage at Cryogenic Temperature*. The Journal of Physical Chemistry C, 2016. **120**(48): p. 27328-27341.
17. Mueller, U., et al., *Metal-organic frameworks-prospective industrial applications*. Journal of Materials Chemistry, 2006. **16**(7): p. 626-636.

18. Kitagawa, S., R. Kitaura, and S.-i. Noro, *Functional porous coordination polymers*. *Angewandte Chemie International Edition*, 2004. **43**: p. 2334-2375.
19. Lee, J., et al., *Metal-organic framework materials as catalysts*. *Chemical Society Reviews*, 2009. **38**: p. 1450-1459.
20. Dincă, M. and J.R. Long, *Hydrogen Storage in Microporous Metal–Organic Frameworks with Exposed Metal Sites*. *Angewandte Chemie International Edition*, 2008. **47**(36): p. 6766-6779.
21. Wang, Z.-J., et al., *H-Bonding Interactions Induced Two Isostructural Cd(II) Metal–Organic Frameworks Showing Different Selective Detection of Nitroaromatic Explosives*. *Inorganic Chemistry*, 2016. **55**(21): p. 10999-11005.
22. Cui, Y., B. Chen, and G. Qian, *Lanthanide metal-organic frameworks for luminescent sensing and light-emitting applications*. *Coordination Chemistry Reviews*, 2014. **273–274**: p. 76-86.
23. Ding, S.-B., et al., *Surfactant-assisted synthesis of lanthanide metal-organic framework nanorods and their fluorescence sensing of nitroaromatic explosives*. *Materials Letters*, 2011. **65**: p. 1385-1387.
24. Zhou, J.-M., et al., *Highly selective luminescent sensing of fluoride and organic small-molecule pollutants based on novel lanthanide metal-organic frameworks*. *Inorganic Chemistry*, 2013. **52**: p. 8082-8090.
25. Xia, T., et al., *Highly selective luminescent sensing of picric acid based on a water-stable europium metal-organic framework*. *Journal of Solid State Chemistry*, 2017. **245**: p. 127-131.

26. Zhou, X., et al., *A microporous luminescent europium metal-organic framework for nitro explosive sensing*. Dalton Transactions, 2013. **42**(16): p. 5718-5723.
27. Cundy, C.S. and P.A. Cox, *The Hydrothermal Synthesis of Zeolites: History and Development from the Earliest Days to the Present Time*. Chemical Reviews, 2003. **103**(3): p. 663-701.
28. Rao, C.N.R., *Understanding Chemistry*. 2009, Singapore, SG: WSPC.
29. Ma, M.-L., C. Ji, and S.-Q. Zang, *Syntheses, structures, tunable emission and white light emitting Eu³⁺ and Tb³⁺ doped lanthanide metal-organic framework materials*. Dalton Transactions, 2013. **42**(10579-10586).
30. Shen, L., et al., *Construction of a series of lanthanide metal-organic frameworks: synthesis, structure, luminescence and white light emission*. CrystEngComm, 2015. **17**(48): p. 9363-9369.
31. Huo, R., X. Li, and D. Ma, *Lanthanide coordination frameworks constructed from 1,3-benzenedicarboxylate, oxalate and 1,10-phenanthroline: crystal structure, multicolor luminescence and high-efficiency white light emission*. CrystEngComm, 2015. **17**(20): p. 3838-3844.
32. Liu, J., W. Sun, and Z. Liu, *White-light emitting materials with tunable luminescence based on steady Eu(III) doping of Tb(III) metal-organic frameworks*. RSC Advances, 2016. **6**(31): p. 25689-25694.
33. Wu, J., H. Zhang, and S. Du, *Tunable luminescence and white light emission of mixed lanthanide-organic frameworks based on polycarboxylate ligands*. Journal of Materials Chemistry C, 2016. **4**(16): p. 3364-3374.

34. Wu, L.-L., et al., *A lanthanide(iii) metal-organic framework exhibiting ratiometric luminescent temperature sensing and tunable white light emission*. CrystEngComm, 2016. **18**(23): p. 4268-4271.
35. Cotton, S.A., *Lanthanides and Actinides*. 1991, New York: Oxford University Press.
36. Cotton, S.A., *Establishing coordination numbers for the lanthanides in simple complexes*. Comptes Rendus Chimie, 2005. **8**: p. 129-145.
37. Friedman, H.G., G.R. Choppin, and D.G. Feuerbacher, *The shapes of the f orbitals*. Journal of Chemical Education, 1964. **41**(7): p. 354.
38. Kitagawa, S., S.-i. Noro, and T. Nakamura, *Pore surface engineering of microporous coordination polymers*. Chemical Communications, 2006(7): p. 701-707.
39. Robin, A.Y. and K.M. Fromm, *Coordination polymer networks with O- and N-donors: What they are, why and how they are made*. Coordination Chemistry Reviews, 2006. **250**: p. 2127-2157.
40. James, S.L., *Metal-organic frameworks*. Chemical Society Reviews, 2003. **32**(5): p. 276-288.
41. Rosi, N.L., et al., *Advances in the chemistry of metal-organic frameworks*. CrystEngComm., 2002. **4**: p. 401-404.
42. Rosseinsky, M.J., *Recent developments in metal-organic framework chemistry: design, discovery, permanent porosity and flexibility*. Microporous Mesoporous Mater., 2004. **73**: p. 15-30.

43. Liu, C.-B., et al., *Template-assisted assembly of porous lanthanide coordination polymers with 2-aminoterephthalic acid*. Inorg. Chemical Communications, 2005. **8**: p. 1045-1048.
44. Mohanu, A., C. Brouca-Cabarrecq, and J.-C. Trombe, *New open-framework three-dimensional lanthanide oxalates containing as a template the diprotonated 1,2- or 1,3-diaminopropane*. Journal of Solid State Chemistry, 2006. **179**: p. 3-17.
45. Shannon, R., *Revised effective ionic radii and systematic studies of interatomic distances in halides and chalcogenides*. Acta Crystallographica Section A, 1976. **32**(5): p. 751-767.
46. Fu, J., Y. Tian, and J. Wu, *Seeking metal–organic frameworks for methane storage in natural gas vehicles*. Adsorption, 2015. **21**(6): p. 499-507.
47. Wang, M.-S., et al., *A direct white-light emitting MOF with tunable yellow to white photoluminescence by variation of excitation light*. Journal of the American Chemical Society, 2009. **131**: p. 13572-13573.
48. Hjortnaes, J., S.E.P. New, and E. Aikawa, *Visualizing novel concepts of cardiovascular calcification*. Trends in Cardiovascular Medicine, 2013. **23**: p. 71-79.
49. Horcajada, P., et al., *Metal-organic frameworks in biomedicine*. Chemical Reviews, 2011. **112**: p. 1232-1268.
50. Schiener, M., et al., *Nanomedicine-based strategies for treatment of atherosclerosis*. Trends in Molecular Medicine, 2014. **20**(5): p. 271-281.
51. Judd, B.R., *Optical Absorption Intensities of Rare-Earth Ions*. Physical Review, 1962. **127**(3): p. 750-761.

52. Ofelt, G.S., *Intensities of Crystal Spectra of Rare-Earth Ions*. The Journal of Chemical Physics, 1962. **37**(3): p. 511-520.
53. Van Vleck, J.H., *The puzzle of rare-earth spectra in solids*. Journal of Physical Chemistry, 1937. **41**: p. 67-80.
54. de Lill, D.T. and C.L. Cahill, *Coordination Polymers of the Lanthanide Elements : A Structural Survey*. Progress in Inorganic Chemistry, 2007. **55**: p. 143-203.
55. de Bettencourt-Dias, A., *Lanthanide-based emitting materials in light-emitting diodes*. Dalton Transactions, 2007: p. 2229-2241.
56. Horrocks, W.D., Jr. and D.R. Sudnick, *Lanthanide ion luminescence probes of the structure of biological macromolecules*. Accounts of Chemical Research, 1981. **14**(12): p. 384-392.
57. Einkauf, J.D., et al., *A highly hydrated Eu(III) coordination polymer with exceptional luminescence*. in preparation.
58. Einkauf, J.D., et al., *Toward understanding sensitized luminescence in lanthanide coordination polymers*. manuscript in preparation.
59. Matthes, P.R., et al., *The Series of Rare Earth Complexes [Ln₂Cl₆(μ-4,4'-bipy)(py)₆], Ln=Y, Pr, Nd, Sm-Yb: A Molecular Model System for Luminescence Properties in MOFs Based on LnCl₃ and 4,4'-Bipyridine*. Chemistry - A European Journal, 2013. **19**(51): p. 17369-17378.
60. Einkauf, J.D., et al., *Rethinking Sensitized Luminescence in Lanthanide Coordination Polymers and MOFs: Band Sensitization and Water Enhanced Eu Luminescence in [Ln(C₁₅H₉O₅)₃(H₂O)₃]_n (Ln = Eu, Tb)*. Inorganic Chemistry, 2016. **55**(16): p. 7920-7927.

61. Silva, C.G., A. Corma, and H. García, *Metal-organic frameworks as semiconductors*. Journal of Materials Chemistry, 2010. **20**: p. 3141-3156.
62. Alvaro, M., et al., *Semiconducting behavior of a MOF*. Chemistry - A European Journal, 2007. **13**: p. 5106-5112.
63. Xamena, F.X.L.i., A. Corma, and H. Garcia, *Applications for MOFs as Quantum Dot Semiconductors*. Journal of Physical Chemistry C., 2006. **111**: p. 80-85.
64. Rabenau, A., *The role of hydrothermal synthesis in preparative chemistry*. Angewandte Chemie International Edition, 1985. **24**: p. 1026-1040.
65. Cullity, B.D. and S.R. Stock, *Elements of X-ray Diffraction*. 3rd ed. 2001: Prentice Hall.
66. Glusker, J.P. and T.K. N., *Crystal Structure Analysis: A Primer*. 2nd ed. 1985: Oxford University Press.
67. Baur, K., et al., *Peer Reviewed: Looking at Trace Impurities on Silicon Wafers with Synchrotron Radiation*. Analytical Chemistry, 2002. **74**(23): p. 608 A-616 A.
68. Jones, K.W. and B.M. Gordon, *Trace element determinations with synchrotron-induced x-ray emission*. Analytical Chemistry, 1989. **61**(5): p. 341A-358A.
69. Wrighton, M.S., D.S. Ginley, and D.L. Morse, *A technique for the determination of absolute emission quantum yields of powdered samples*. Journal of Physical Chemistry, 1974. **78**: p. 2229-2233.
70. Allison, R., J. Burns, and A.J. Tuzzolino, *Absolute Fluorescent Quantum Efficiency of Sodium Salicylate*. Journal of the Optical Society of America, 1964. **54**(6): p. 747-751.

71. Horrocks, W.D.J. and D.R. Sudnick, *Lanthanide Ion Probes of Structure in Biology. Laser-Induced Luminescence Decay Constants Provide a Direct Measure of the Number of Metal-Coordinated Water Molecules*. Journal of the American Chemical Society, 1979. **101**(2): p. 334-340.
72. Choppin, G.R. and D.R. Peterman, *Applications of lanthanide luminescence spectroscopy to solution studies of coordination chemistry*. Coordination Chemistry Reviews, 1998. **174**: p. 283-299.
73. Daignebonne, C., et al., *Structural and Luminescent Properties of Micro- and Nanosized Particles of Lanthanide Terephthalate Coordination Polymers*. Inorganic Chemistry, 2008. **47**(9): p. 3700-3708.
74. Shavaleev, N.M., et al., *Influence of Symmetry on the Luminescence and Radiative Lifetime of Nine-Coordinate Europium Complexes*. Inorganic Chemistry, 2015. **54**(18): p. 9166-9173.
75. Werts, M.H.V., R.T.F. Jukes, and J.W. Verhoeven, *The emission spectrum and the radiative lifetime of Eu³⁺ in luminescent lanthanide complexes*. Physical Chemistry Chemical Physics, 2002. **4**(9): p. 1542-1548.
76. Crosby, G.A., R.E. Whan, and R.M. Alire, *Intramolecular energy transfer in rare earth chelates. Role of the triplet state*. Journal of Chemical Physics, 1961. **34**(3): p. 743-748.
77. Williams, D.E. and R.E. Rundle, *Crystal Structure of 3,4-Furandicarboxylic Acid*. Journal of the American Chemical Society, 1964. **86**(9): p. 1660-1666.

78. Zhang, L., et al., *Breaking the Mirror: pH-Controlled Chirality Generation from a meso Ligand to a Racemic Ligand*. Chemistry – A European Journal, 2009. **15**(4): p. 989-1000.
79. Jia, T.-J., et al., *Preparations, structures and properties of heterobimetallic complexes based on tetrahydrofuran-2,3,4,5-tetracarboxylate*. Journal of Solid State Chemistry, 2013. **201**: p. 208-214.
80. Zhang, L., et al., *Novel (3,6)-connected network and (4,6)-connected framework in two copper(II) and cadmium(II) complexes of flexible (2S,3S,4R,5R)-tetrahydrofuran-tetracarboxylic acid: synthesis, structure, thermostability, and luminescence studies*. CrystEngComm, 2009. **11**(9): p. 1934-1939.
81. Wang, X.-Y., M. Scancella, and S.C. Sevov, *Studies of the Mechanism of a Single-Crystal-to-Single-Crystal Reversible Dehydration of a Copper Carboxylate Framework*. Chemistry of Materials, 2007. **19**(18): p. 4506-4513.
82. Thuéry, P., et al., *Uranyl-Based Metallamacrocycles: Tri- and Tetranuclear Complexes with (2R,3R,4S,5S)-Tetrahydrofuran-tetracarboxylic Acid*. Journal of the American Chemical Society, 2004. **126**(22): p. 6838-6839.
83. Xu, J., et al., *Poly[[μ]-5-5-carboxylatotetrahydrofuran-2,3,4-tricarboxylic acid)sodium]*. Acta Crystallographica Section E, 2009. **65**(11): p. m1419-m1420.
84. Greig, N.E., et al., *Luminescent lanthanide coordination polymers synthesized via in-situ hydrolysis of dimethyl-3,4-furandicarboxylate*. Journal of Solid State Chemistry, 2015. **225**: p. 402-409.
85. Speck, A.L., *PLATON*. Acta Crystallogr., Sect. A, 1990. **46**: p. C34.

86. Binnemans, K. and C. Gorller-Walrand, *On the color of the trivalent lanthanide ions*. Chemical Physics Letters, 1995. **235**(3,4): p. 163-174.
87. Kerbellec, N., et al., *An Unprecedented Family of Lanthanide-Containing Coordination Polymers with Highly Tunable Emission Properties*. Inorganic Chemistry, 2009. **48**(7): p. 2837-2843.
88. Ang, D., et al., *Synthesis and structure of the two-dimensional coordination networks $[Ln(PDC)(N-HPDC)]_{\infty}$ ($PDC = \text{pyridine-3,4-dicarboxylate}$, $Ln = La, Ce, Pr$)*. Polyhedron, 2007. **26**(2): p. 385-391.
89. Brouca-Cabarrecq, C., et al., *Hydrothermal investigation of the lanthanide ($Ln=La, Ce, Pr, Nd, Sm$) 2,6-pyridinedicarboxylate system*. Inorganica Chimica Acta, 2002. **332**(1): p. 54-60.
90. Cheng, C.-X., et al., *catena-Poly[[[diaqua(6-carboxypyridine-2-carboxylato- κ_3O,N,O')erbium(III)]- μ -pyridine-2,6-dicarboxylato- $\kappa_4O,N,O':O$] tetrahydrate]*. Acta Crystallographica Section E, 2007. **63**(1): p. m1-m3.
91. Dong, B.-X. and J. Peng, *Poly[[pentaquatris(μ_3,μ_2 -pyridine-3,4-dicarboxylato)dilanthanum(III)] monohydrate]*. Acta Crystallographica Section E, 2007. **63**(3): p. m886-m888.
92. Liu, Y., et al., *catena-Poly[[[diaqua(6-carboxypyridine-2-carboxylato)samarium(II)]- μ -pyridine-2,6-dicarboxylato] tetrahydrate]*. Acta Crystallographica Section E, 2006. **62**(11): p. m2794-m2795.
93. Duan, L., et al., *Hydrothermal synthesis and crystal structures of two novel rare earth coordination polymers based on pyridine-2,6-dicarboxylic acid*. Journal of Molecular Structure, 2004. **689**(3): p. 269-274.

94. Escande, A., et al., *Complexation of Trivalent Lanthanides with Planar Tridentate Aromatic Ligands Tuned by Counteranions and Steric Constraints*. *Inorganic Chemistry*, 2009. **48**(3): p. 1132-1147.
95. Fernandes, A., et al., *Study of new lanthanide complexes of 2,6-pyridinedicarboxylate: synthesis, crystal structure of Ln(Hdipic)(dipic) with Ln=Eu, Gd, Tb, Dy, Ho, Er, Yb, luminescence properties of Eu(Hdipic)(dipic)*. *Polyhedron*, 2001. **20**(18): p. 2385-2391.
96. Gao, H.-L., et al., *Synthesis and Characterization of Metal–Organic Frameworks Based on 4-Hydroxypyridine-2,6-dicarboxylic Acid and Pyridine-2,6-dicarboxylic Acid Ligands*. *Inorganic Chemistry*, 2006. **45**(15): p. 5980-5988.
97. Ghosh, S.K. and P.K. Bharadwaj, *Coexistence of Water Dimer and Hexamer Clusters in 3D Metal–Organic Framework Structures of Ce(III) and Pr(III) with Pyridine-2,6-dicarboxylic Acid*. *Inorganic Chemistry*, 2003. **42**(25): p. 8250-8254.
98. Huang, Y., et al., *Syntheses, structures, and photoluminescence of three-dimensional lanthanide coordination polymers with 2,5-pyridinedicarboxylic acid*. *Journal of Solid State Chemistry*, 2008. **181**(8): p. 1731-1737.
99. Lu, Y.-L., et al., *Influence of water content on the self-assembly of metal-organic frameworks based on pyridine-3,5-dicarboxylate*. *Inorganic Chemistry*, 2006. **45**(6): p. 2430-2437.
100. Min, D. and S.W. Lee, *Terbium-oxalate-pyridinedicarboxylate coordination polymers suggesting the reductive coupling of carbon dioxide (CO₂) to oxalate (C₂O₄²⁻): [Tb₂ (3,5-PDC)₂(H₂O)₄(C₂O₄)]·2H₂O and [Tb(2,4-PDC)(H₂O)(C₂O₄)_{0.5}]*

- (PDC = pyridinedicarboxylate). *Inorganic Chemistry Communications*, 2002. **5**(11): p. 978-983.
101. Chen, L., et al., *Synthesis, crystal structures and photoluminescence of Zn–Ln heterometallic polymers based on pyridine-2,3-dicarboxylic acid*. *Inorganic Chemistry Communications*, 2009. **12**(8): p. 761-765.
102. Prasad, T.K. and M.V. Rajasekharan, *Cerium(IV)–Lanthanide(III)–Pyridine-2,6-dicarboxylic Acid System: Coordination Salts, Chains, and Rings*. *Inorganic Chemistry*, 2009. **48**(24): p. 11543-11550.
103. Shi, Q., et al., *Synthesis and crystal structure of metal-organic frameworks $[Ln_2(pydc-3,5)_3(H_2O)_9]_n \cdot 3H_2O$ ($Ln = Sm, Eu, Gd, Dy$; $pydc-3,5 =$ pyridine-3,5-dicarboxylate) along with the photoluminescent property of its europium one*. *Journal of Molecular Structure*, 2007. **837**(1–3): p. 185-189.
104. Song, Y.-S., B. Yan, and Z.-X. Chen, *Two novel lanthanide 1-D chain coordination polymers of pyridinedicarboxylic acids: hydrothermal synthesis, structure and luminescent properties*. *Journal of Molecular Structure*, 2005. **750**(1–3): p. 101-108.
105. Zhao, B., et al., *Systematic Investigation of the Hydrothermal Syntheses of Pr(III)–PDA (PDA = Pyridine-2,6-dicarboxylate Anion) Metal–Organic Frameworks*. *Inorganic Chemistry*, 2005. **44**(4): p. 911-920.
106. Liu, M.-S., et al., *One-, Two-, and Three-Dimensional Lanthanide Complexes Constructed from Pyridine-2,6-dicarboxylic Acid and Oxalic Acid Ligands*. *Crystal Growth & Design*, 2008. **8**(11): p. 4083-4091.

107. Feng, X., et al., *Hydrothermal Synthesis, Crystal Structure, and Properties of A 3D Holmium(III) Coordination Framework Based on the Pyridine 2,6-dicarboxylate and Oxalate Ligands*. *Synthesis and Reactivity in Inorganic, Metal-Organic, and Nano-Metal Chemistry*, 2010. **40**(7): p. 479-484.
108. Hu, X., *A series of water soluble RE(III) complexes: Synthesis, characterization, photophysical property and sensing activity towards Cr(III)*. *Synthetic Metals*, 2011. **161**(11–12): p. 1022-1028.
109. Dongfang, X.U., et al., *Synthesis, characterization, and biological studies of lanthanide complexes with 2,6-pyridine dicarboxylic acid and α -picolinic acid*. *Journal of Coordination Chemistry*, 2010. **63**(13): p. 2360-2369.
110. Zhang, G.-C., et al., *Thermochemistry on $K_2[M(DPA)_2] \cdot 7H_2O(s)$ ($M = Cu$ and Ni , $H_2DPA =$ pyridine-2,6-dicarboxylic acid)*. *Thermochimica Acta*, 2011. **518**(1–2): p. 66-71.
111. Zhang, M., et al., *Crystal structure and thermal properties of novel Co(II) complexes with 2,6-pyridine-dicarboxylate containing infinite one-dimensional chain: $[CoL(HO)][Co(pydc)] \cdot 2HO$ and $[Co(HO)] \times [Co(pydc)]L \cdot HO$ ($L = 1,3$ -bis(4-pyridyl)propane, $L = 3$ -amino-1H-1,2,4-triazole, $pydc = 2,6$ -pyridine-dicarboxylic acid)*. *Journal of Structural Chemistry*, 2010. **51**(6): p. 1145-1151.
112. Du, G., X. Kan, and H. Li, *Synthesis, crystal structure, and magnetic properties of two 3d–4f heterometallic coordination polymers*. *Polyhedron*, 2011. **30**(18): p. 3197-3201.
113. Tabatabaee, M., et al., *Hydrothermal Preparation, Crystal Structures, Spectroscopic and Thermal Analyses of Cadmium(II) and Cobalt(II) Coordination*

- Polymers With Pyridine-2,3-dicarboxylic Acid*. Journal of Inorganic and Organometallic Polymers and Materials, 2011. **21**(3): p. 450-457.
114. Niu, C.-Y., et al., *A one-dimensional copper(II) coordination polymer constructed by pyridyl-2,5-dicarboxylate: Helical structure and magnetic property*. Journal of Molecular Structure, 2011. **997**(1–3): p. 60-63.
115. Qu, H., et al., *Structures and photocatalytic activities of metal-organic frameworks derived from rigid aromatic dicarboxylate acids and flexible imidazole-based linkers*. Inorganic Chemistry Communications, 2011. **14**(9): p. 1347-1351.
116. Larrea, E.S., et al., *[NaCu(2,4-HPdc)(2,4-Pdc)] Mixed Metal–Organic Framework as a Heterogeneous Catalyst*. European Journal of Inorganic Chemistry, 2015. **2015**(28): p. 4699-4707.
117. Yu, Z., P. Jiang, and Y. Chen, *Crystal structure of poly[[hexaqua-1κ4O,2κ2O-bis(μ₃-pyridine-2,4-dicarboxylato-1κO2:2κ₂N,O2';1'κO4)cobalt(II)strontium(II)] dihydrate]*. Acta Crystallographica Section E, 2015. **71**(9): p. m167-m168.
118. Yang, Y., T. Li, and Y. Chen, *The first three-dimensional FeIII-SrII heterometallic coordination polymer: poly[[diaquatetrakis(μ₃-pyridine-2,3-dicarboxylato)diiron(III)strontium(II)] dihydrate]*. Acta Crystallographica Section C, 2015. **71**(10): p. 903-907.
119. Llano-Tomé, F., et al., *Cu-PDC-bpa solid coordination frameworks (PDC=2,5-pyridinedicarboxylate; bpa=1,2-DI(4-pyridil)ethane)): 2D and 3D structural flexibility producing a 3-c herringbone array next to ideal*. Journal of Solid State Chemistry, 2015. **230**: p. 191-198.

120. Wang, X.-L., et al., *Polycarboxylate-directed various Co(II) complexes based on a "V"-like bis-pyridyl-bis-amide derivative: construction, electrochemical and photocatalytic properties*. CrystEngComm, 2015. **17**(38): p. 7290-7299.
121. Chaigneau, J., J. Marrot, and D. Riou, *Diaquatetrakis(pyridine-2,6-dicarboxylato- κ_2O_2,O_6)tetrakis(μ -pyridine-3,5-dicarboxylic acid- $\kappa_2N:O$)tetracopper(II): a copper complex with tetrameric molecular units*. Acta Crystallographica Section C, 2004. **60**(3): p. m101-m103.
122. Tian, G., et al., *A chiral layered Co(II) coordination polymer with helical chains from achiral materials*. Chemical Communications, 2005(11): p. 1396-1398.
123. Biswas, S., et al., *Planar tetrameric metal cluster formation at room temperature induced by $\pi \cdots \pi$ interactions: 3D supramolecular host containing 1D channel filled with solvent methanol*. Inorganica Chimica Acta, 2011. **368**(1): p. 216-222.
124. Wang, N., et al., *Hydrothermal synthesis, crystal structure and magnetic characterization of two 4f-3d heterometallic coordination polymers*. Inorganica Chimica Acta, 2010. **363**(5): p. 1008-1012.
125. Yue, Q., et al., *Three-Dimensional 3d-4f Heterometallic Coordination Polymers: Synthesis, Structures, and Magnetic Properties*. Inorganic Chemistry, 2005. **44**(15): p. 5241-5246.
126. Mahata, P. and S. Natarajan, *A New Series of Three-Dimensional Metal-Organic Framework, $[M_2(H_2O)][C_5N_1H_3(COO)_2]_3 \cdot 2H_2O$, $M = La, Pr, \text{ and } Nd$: Synthesis, Structure, and Properties*. Inorganic Chemistry, 2007. **46**(4): p. 1250-1258.

127. Li, M., et al., *Syntheses, Structures, and Photoluminescence of Three Novel Coordination Polymers Constructed from Dimeric d^{10} Metal Units*. *Crystal Growth & Design*, 2006. **6**(9): p. 2036-2040.
128. Zhou, Y.-X., et al., *1D, 2D and 3D Coordination Polymers of Aromatic Carboxylate TbIII: Structure, Thermolysis Kinetics and Fluorescence*. *European Journal of Inorganic Chemistry*, 2008. **2008**(27): p. 4280-4289.
129. Mahata, P., et al., *A novel sheet 4f-3d mixed-metal pyridine dicarboxylate: synthesis, structure, photophysical properties and its transformation to a perovskite oxide*. *Chemical Communications*, 2005(46): p. 5787-5789.
130. Mahata, P., K.V. Ramya, and S. Natarajan, *Pillaring of $CdCl_2$ -Like Layers in Lanthanide Metal–Organic Frameworks: Synthesis, Structure, and Photophysical Properties*. *Chemistry – A European Journal*, 2008. **14**(19): p. 5839-5850.
131. Chen, W., et al., *Synthesis, Structure, and Photoelectronic Effects of a Uranium–Zinc–Organic Coordination Polymer Containing Infinite Metal Oxide Sheets*. *Journal of the American Chemical Society*, 2003. **125**(31): p. 9266-9267.
132. Ramirez, A.L., et al., *Structure and luminescence of 2-dimensional coordination polymers of lanthanide(III) ions with 2,3-pyridinedicarboxylic acid*. *Inorganica Chimica Acta*, 2012. **392**: p. 46-51.
133. Brese, N.E. and M. O'Keefe, *Bond-Valence Parameters for Solids*. *Acta Crystallographica*, 1991. **B47**: p. 192-197.
134. Brown, I.D. and D. Altermatt, *Bond-valence parameters obtained from a systematic analysis of the inorganic crystal structure database*. *Acta Crystallographica Section B*, 1985. **B41**: p. 244-247.

135. Trzesowska, A., R. Kruszynski, and T.J. Bartczak, *New bond-valence parameters for lanthanides*. Acta Crystallographica, 2004. **B60**(174-178).
136. Eddaoudi, M., et al., *Geometric requirements and examples of important structures in the assembly of square building blocks*. Proceedings of the National Academy of Sciences, 2002. **99**(8): p. 4900-4904.
137. Qin, L., et al., *Two sinusoidal wavelike 2D coordination polymers with benzophenone-4,4'-dicarboxylate*. Inorganica Chimica Acta, 2014. **409, Part B**: p. 233-237.
138. Furukawa, H., et al., *Control of Vertex Geometry, Structure Dimensionality, Functionality, and Pore Metrics in the Reticular Synthesis of Crystalline Metal–Organic Frameworks and Polyhedra*. Journal of the American Chemical Society, 2008. **130**(35): p. 11650-11661.
139. Sun, C.-Y. and L.-P. Jin, *Hydrothermal synthesis and structural studies of two new copper(II) coordination polymers with V-shape ligands*. Journal of Molecular Structure, 2006. **782**(2–3): p. 171-176.
140. Park, H.J. and M.P. Suh, *Stepwise and hysteretic sorption of N₂, O₂, CO₂, and H₂ gases in a porous metal-organic framework [Zn₂(BPnDC)₂(bpy)]*. Chemical Communications, 2010. **46**(4): p. 610-612.
141. Bon, V., et al., *In Situ Observation of Gating Phenomena in the Flexible Porous Coordination Polymer Zn₂(BPnDC)₂(bpy) (SNU-9) in a Combined Diffraction and Gas Adsorption Experiment*. Inorganic Chemistry, 2014. **53**(3): p. 1513-1520.

142. Reinsch, H., et al., *First Keto-Functionalized Microporous Al-Based Metal–Organic Framework: [Al(OH)(O₂C-C₆H₄-CO-C₆H₄-CO₂)].* Inorganic Chemistry, 2013. **52**(4): p. 1854-1859.
143. Wang, Y., et al., *Hydrothermal synthesis and structure of new lanthanide coordination polymers with dicarboxylic acid and 1,10-phenanthroline.* Journal of Molecular Structure, 2004. **692**(1–3): p. 177-186.
144. Wang, Y.-B. and L.-P. Jin, *catena-(tris(m4-Benzophenone-4,4'-dicarboxylato)-(1,10-phenanthroline)-di-lanthanum(III)).* Chinese Journal of Chemistry, 2004. **22**: p. 1272.
145. de Lill, D.T. and B.C. Chan, *Structure and luminescence of a one-dimensional uranium coordination polymer assembled through benzophenone-4,4'-dicarboxylate.* Inorganica Chimica Acta, 2013. **404**: p. 215-218.
146. Einkauf, J.D., B.C. Chan, and D.T. de Lill, *Reversible solvent-induced transformation of a one-dimensional uranyl coordination polymer using 4,4'-oxybis(benzoate).* Polyhedron, 2017. **128**: p. 149-153.
147. Wang, W., et al., *catena-Poly[[aquadioxidouranium(VI)]-μ₃-4,4'-oxydibenzoato].* Acta Crystallographica Section E, 2010. **66**(4): p. m462.
148. Dalai, S., et al., *Combination of covalent and hydrogen bonding in the formation of 3D uranyl-carboxylate networks.* Inorganica Chimica Acta, 2010. **363**(13): p. 3407-3412.
149. Aspinall, H.C., *Chemistry of the f-Block Elements.* 2001: CRC.
150. Liu, Y., et al., *Optical spectroscopy of lanthanides doped in wide band-gap semiconductor nanocrystals.* Journal of Luminescence, 2011. **131**(3): p. 415-422.

151. Faulkner, S. and S.J.A. Pope, *Lanthanide-Sensitized Lanthanide Luminescence: Terbium-Sensitized Ytterbium Luminescence in a Trinuclear Complex*. Journal of the American Chemical Society, 2003. **125**(35): p. 10526-10527.
152. Dexter, D.L., *A theory of sensitized luminescence in solids*. Journal of Chemical Physics, 1953. **21**(5): p. 836-850.
153. Horrocks, W.D.J. and D.R. Sudnick, *Lanthanide ion probes of structure in biology. Laser-induced luminescence decay constants provide a direct measure of the number of metal-coordinated water molecules*. Journal of the American Chemical Society, 1979. **101**(2): p. 334-340.
154. Choppin, G.R. and D.R. Peterman, *Applications of lanthanide luminescence spectroscopy to solution studies of coordination chemistry*. Coordination Chemistry Reviews, 1998. **174**(1): p. 283-299.
155. Einkauf, J.D., et al., *Rethinking Sensitized Luminescence in Lanthanide Coordination Polymers and MOFs: Band Sensitization and Water Enhanced Eu Luminescence in $[Ln(C_{15}H_9O_5)_3(H_2O)_3]_n$ ($Ln = Eu, Tb$)*. Inorganic Chemistry, 2016.
156. MacNeill, C.M., et al., *Synthesis, crystal structure and properties of novel isostructural two-dimensional lanthanide-based coordination polymers with 2,3,5,6-tetrafluoro-1,4-benzenedicarboxylic acid*. Inorganica Chimica Acta, 2011. **365**: p. 196-203.
157. Reineke, T.M., et al., *From Condensed Lanthanide Coordination Solids to Microporous Frameworks Having Accessible Metal Sites*. Journal of the American Chemical Society, 1999. **121**(8): p. 1651-1657.

158. Serre, C., et al., *Hydrothermal synthesis, structure characterization, and thermal behavior of new three-dimensional europium terephthalates: MIL-51LT,HT and MIL-52 or $\text{Eu}_{2n}(\text{OH})_x(\text{H}_2\text{O})_y(\text{O}_2\text{C}-\text{C}_6\text{H}_4-\text{CO}_2)_z$ ($n = \text{III, III, II}$; $x = 4, 0, 0$; $y = 2, 0, 0$; $z = 1, 1, 2$). Chemistry of Materials, 2002. **14**(5): p. 2409-2415.*
159. Fan, L.-Q. and J.-H. Wu, *Poly[diatetrakis(μ_4 -isophthalato)dilanthanum(III)]*. Acta Crystallographica Section E, 2010. **66**(2): p. m240.
160. Luo, Y., et al., *Synthesis, crystal structure and luminescent properties of new lanthanide-containing coordination polymers involving 4,4'-oxy-bis-benzoate as ligand*. CrystEngComm, 2013. **15**(4): p. 706-720.
161. Latva, M., et al., *Correlation between the lowest triplet state energy level of the ligand and lanthanide(III) luminescence quantum yield*. Journal of Luminescence, 1997. **75**: p. 149-169.
162. Liu, G.K., *Systematics of f-element crystal-field interaction*. Journal of Solid State Chemistry, 2005. **178**: p. 489-498.
163. Flage-Larsen, E., et al., *Band Gap Modulations in UiO Metal-Organic Frameworks*. Journal of Physical Chemistry C, 2013. **117**(40): p. 20610-20616.
164. Valenzano, L., et al., *Disclosing the Complex Structure of UiO-66 Metal Organic Framework: A Synergic Combination of Experiment and Theory*. Chemistry of Materials, 2011. **23**(7): p. 1700-1718.
165. Kuc, A., A. Enyashin, and G. Seifert, *Metal-Organic Frameworks: Structural, Energetic, Electronic, and Mechanical Properties*. Journal of Physical Chemistry B, 2007. **111**(28): p. 8179-8186.

166. Dieke, G.H., *Spectra and energy levels of rare earth ions in crystals*, ed. H.M. Crosswhite and H. Crosswhite. 1968, New York: John Wiley & Sons, Inc.
167. Heimel, G., *The Optical Signature of Charges in Conjugated Polymers*. ACS Central Science, 2016. **2**(5): p. 309-315.
168. Salaneck, W.R., R.H. Friend, and J.L. Brédas, *Electronic structure of conjugated polymers: consequences of electron–lattice coupling*. Physics Reports, 1999. **319**(6): p. 231-251.
169. Bassler, H. and A. Kohler, *Charge transport in organic semiconductors*. Topics in Current Chemistry, 2012. **312**: p. 1-65.
170. Hummer, K. and C. Ambrosch-Draxl, *Electronic properties of oligoacenes from first principles*. Physical Chemistry Reviews B, 2005. **72**(20): p. 205205.
171. Seo, D.-K. and R. Hoffmann, *Direct and indirect band gap types in one-dimensional conjugated or stacked organic materials*. Theoretical Chemistry Accounts, 1999. **102**(1): p. 23-32.
172. Horst, J.-W.V.D., *The electronic and optical properties of conjugated polymers: predictions from first-principles solid-state methods*. 2001, Technische Universiteit Eindhoven: Eindhoven, Neth. .
173. Bünzli, J.-C.G., *On the design of highly luminescent lanthanide complexes*. Coordination Chemistry Reviews, 2015. **293–294**: p. 19-47.
174. Sobieray, M., et al., *Bright luminescence in lanthanide coordination polymers with tetrafluoroterephthalate as a bridging ligand*. Journal of the Chemical Society, Dalton Transactions, 2015. **44**: p. 6249-6259.

175. Zhu, J., et al., *Luminescence and nonlinear optics of 1D N,N'-bis(salicylidene)-1,2-cyclohexanediamine lanthanide coordination polymers*. Synthetic Metals, 2014. **192**: p. 29-36.
176. de Jesus, R.A., et al., *Dual emission tunable in the near-infrared (NIR) and visible (VIS) spectral range by mix-LnMOF*. Dalton Transactions, 2015. **44**(39): p. 17318-17325.
177. Zhang, F., et al., *Towards full-color-tunable emission of two component Eu(iii)-doped Gd(III) coordination frameworks by the variation of excitation light*. Dalton Transactions, 2014. **43**(33): p. 12574-12581.
178. Singha, D.K., et al., *Visible detection of explosive nitroaromatics facilitated by a large stokes shift of luminescence using europium and terbium doped yttrium based MOFs*. RSC Advances, 2015. **5**(123): p. 102076-102084.
179. Zhou, J., et al., *A Bimetallic Lanthanide Metal–Organic Material as a Self-Calibrating Color-Gradient Luminescent Sensor*. Advanced Materials, 2015. **27**(44): p. 7072-7077.
180. Zhao, D., et al., *Syntheses, structures and tunable luminescence of lanthanide metal-organic frameworks based onazole-containing carboxylic acid ligand*. Journal of Solid State Chemistry, 2015. **230**: p. 287-292.
181. Zhai, L., et al., *Observation of divergent La³⁺ ion dilute effect in two series of 3-D fluorescent lanthanide-MOFs-based molecular alloys RE_xLa_{1-x}-EBTC (RE₃₊=Eu₃₊ or Tb₃₊; EBTC⁴⁻=1,1'-ethynebenzene-3,3',5,5'-etracarboxylate)*. Journal of Solid State Chemistry, 2015. **230**: p. 14-18.

182. Shen, L. et al., *Construction of a series of lanthanide metal-organic frameworks: synthesis, structure, luminescence and white light emission*. CrystEngComm, 2015. **17**(48): p. 9363-9369.
183. Jia, J., et al., *Lanthanide coordination polymers constructed from 5-(1H-tetrazol-5-yl)isophthalic acid ligand: white light emission and color tuning*. CrystEngComm, 2015. **17**(31): p. 6030-6036.
184. Fang, M., et al., *Novel lanthanide coordination polymers with Eu-compound exhibits warm white light emission: Synthesis, structure, and magnetic properties*. Inorganic Chemistry Communications, 2016. **70**: p. 51-55.
185. Thangavelu, S.G., et al., *Synthesis, Structures, and Luminescent Properties of Uranyl Terpyridine Aromatic Carboxylate Coordination Polymers*. Inorganic Chemistry, 2013. **52**(4): p. 2060-2069.
186. Knope, K.E. and C.L. Cahill, *Homometallic Uranium(VI) Phosphonoacetates Containing Interlayer Dipyridines*. Inorganic Chemistry, 2009. **48**(14): p. 6845-6851.
187. McCarthy, B.D., et al., *Charge Transfer or J-Coupling? Assignment of an Unexpected Red-Shifted Absorption Band in a Naphthalenediimide-Based Metal–Organic Framework*. Journal of Physical Chemistry Letters, 2013. **4**(3): p. 453-458.
188. Rajagopal, S.K., P.S. Salini, and M. Hariharan, *S \cdots π , π – π , and C–H \cdots π Contacts Regulate Solid State Fluorescence in Regioisomeric Bisthiazolylpyrenes*. Crystal Growth and Design, 2016. **16**(8): p. 4567-4576.

189. Andraud, C. and O. Maury, *Lanthanide Complexes for Nonlinear Optics: From Fundamental Aspects to Applications*. European Journal of Inorganic Chemistry, 2009. **2009**(29-30): p. 4357-4371.
190. Freeman, A.J. and R.E. Watson, *Theoretical Investigation of Some Magnetic and Spectroscopic Properties of Rare-Earth Ions*. Physics Reviews, 1962. **127**(6): p. 2058-2075.
191. Abdi, M.M., et al., *Optical band gap and conductivity measurements of polypyrrole-chitosan composite thin films*. Chinese Journal of Polymer Science, 2012. **30**(1): p. 93-100.
192. Reda, S.M. and S.M. Al-Ghannam, *Synthesis and electrical properties of polyaniline composite with silver nanoparticles*. Advanced Materials in Physics and Chemistry, 2012. **2**: p. 75-81.
193. Freslon, S., et al., *Influence of Photoinduced Electron Transfer on Lanthanide-Based Coordination Polymer Luminescence: A Comparison between Two Pseudoisorecticular Molecular Networks*. Inorganic Chemistry, 2014. **53**(2): p. 1217-1228.
194. de Lill, D.T., A. de Bettencourt Dias, and C.L. Cahill, *Exploring lanthanide luminescence in metal-organic frameworks: Synthesis, structure, and guest-sensitized luminescence of a mixed europium/terbium-adipate framework and a terbium-adipate framework*. Inorganic Chemistry, 2007. **46**(10): p. 3960-3965.
195. Ananias, D., et al., *Molecule-Like Eu₃₊-Dimers Embedded in an Extended System Exhibit Unique Photoluminescence Properties*. Journal of the American Chemical Society, 2009. **131**(24): p. 8620-8626.

196. de Lill, D.T., A. de Bettencourt-Dias, and C.L. Cahill, *Exploring Lanthanide Luminescence in Metal-Organic Frameworks: Synthesis, Structure, and Guest-Sensitized Luminescence of a Mixed Europium/Terbium-Adipate Framework and a Terbium-Adipate Framework*. *Inorganic Chemistry*, 2007. **46**(10): p. 3960-3965.
197. Zhong, Q., et al., *Novel stoichiometrically erbium-ytterbium cocrystalline complex exhibiting enhanced near-infrared luminescence*. *Inorganic Chemistry*, 2006. **45**: p. 4537-4543.
198. Li, Q., T. Li, and J. Wu, *Luminescence of Europium(III) and Terbium(III) Complexes Incorporated in Poly(Vinyl Pyrrolidone) Matrix*. *Journal of Physical Chemistry B*, 2001. **105**(49): p. 12293-12296.
199. Souri, N., et al., *Upconverted Photosensitization of Tb Visible Emission by NIR Yb Excitation in Discrete Supramolecular Heteropolynuclear Complexes*. *Journal of the American Chemical Society*, 2017. **139**(4): p. 1456-1459.
200. Zeng, H.-H., et al., *A luminescent lanthanide coordination polymer based on energy transfer from metal to metal for hydrogen peroxide detection*. *Biosensors and Bioelectronics*, 2017. **89, Part 2**: p. 721-727.
201. Harbuzaru, B.V., et al., *Metal–Organic Nanoporous Structures with Anisotropic Photoluminescence and Magnetic Properties and Their Use as Sensors*. *Angewandte Chemie International Edition*, 2008. **47**(6): p. 1080-1083.
202. Cui, Y., et al., *A Luminescent Mixed-Lanthanide Metal–Organic Framework Thermometer*. *Journal of the American Chemical Society*, 2012. **134**(9): p. 3979-3982.

203. Yan, L., Q. Guodong, and W. Zhiyu, *Temperature-dependent luminescent properties of Eu-Tb complexes synthesized in situ in gel glass*. Applied Physics Letters, 2005. **86**(7): p. 071907-071907.
204. Freslon, S., et al., *Brightness and Color Tuning in a Series of Lanthanide-Based Coordination Polymers with Benzene-1,2,4,5-tetracarboxylic Acid as a Ligand*. Inorganic Chemistry, 2016. **55**(2): p. 794-802.
205. Shi, Z.-Q., Z.-J. Guo, and H.-G. Zheng, *Two luminescent Zn(II) metal-organic frameworks for exceptionally selective detection of picric acid explosives*. Chemical Communications, 2015. **51**(39): p. 8300-8303.
206. Wang, X.-P., et al., *Microporous Cd(II) metal-organic framework as fluorescent sensor for nitroaromatic explosives at the sub-ppm level*. Journal of Molecular Structure, 2016. **1107**: p. 1-6.
207. Hu, Z., B.J. Deibert, and J. Li, *Luminescent metal-organic frameworks for chemical sensing and explosive detection*. Chemical Society Reviews, 2014. **43**(16): p. 5815-5840.
208. Lu, W., et al., *Colorimetric sensor arrays based on pattern recognition for the detection of nitroaromatic molecules*. Journal of Hazardous Materials, 2017. **326**: p. 130-137.
209. Zhang, S.-R., et al., *A Fluorescent Sensor for Highly Selective Detection of Nitroaromatic Explosives Based on a 2D, Extremely Stable, Metal–Organic Framework*. Chemistry – A European Journal, 2014. **20**(13): p. 3589-3594.

210. Thomas, S.W., G.D. Joly, and T.M. Swager, *Chemical Sensors Based on Amplifying Fluorescent Conjugated Polymers*. Chemical Reviews, 2007. **107**(4): p. 1339-1386.
211. Salinas, Y., et al., *Optical chemosensors and reagents to detect explosives*. Chemical Society Reviews, 2012. **41**(3): p. 1261-1296.
212. Haryono, M., et al., *One dimensional assembly of Mn6 single molecule magnets linked by oligothiophene bridges*. Dalton Transactions, 2010. **39**(20): p. 4751-4756.
213. Chisholm, M.H., et al., *Preparations and Photophysical Properties of Fused and Nonfused Thienyl Bridged MM (M = Mo or W) Quadruply Bonded Complexes*. Inorganic Chemistry, 2008. **47**(8): p. 3415-3425.
214. Zhao, J., et al., *Zinc and cadmium coordination polymers assembled with 2,2'-bipyridine and bithiophenedicarboxylic acid: Effect of metal ions on the conformation of ligand*. Inorganica Chimica Acta, 2012. **383**: p. 185-189.
215. Zhao, J., et al., *Synthesis, Structure, and Photoluminescent Properties of Metal–Organic Coordination Polymers Assembled with Bithiophenedicarboxylic Acid*. Inorganic Chemistry, 2011. **50**(8): p. 3198-3205.
216. Yoon, M. and D. Moon, *New Zr (IV) based metal-organic framework comprising a sulfur-containing ligand: Enhancement of CO₂ and H₂ storage capacity*. Microporous and Mesoporous Materials, 2015. **215**: p. 116-122.
217. Zhao, Y., et al., *Easily-soluble heteroacene bis(benzothieno)silole derivatives for sensing of nitro explosives*. New Journal of Chemistry, 2014. **38**(12): p. 5754-5760.

218. Verbitskiy, E.V., et al., *Microwave-assisted synthesis of 4-(2,2'-bithiophen-5-yl)-5-phenylpyrimidine derivatives as sensors for detection of nitroaromatic explosives*. Chemistry of Heterocyclic Compounds, 2016. **52**(11): p. 904-909.
219. Rella, R., et al., *Gas sensing measurements and analysis of the optical properties of poly[3-(butylthio)thiophene] Langmuir–Blodgett films*. Sensors and Actuators B: Chemical, 2000. **68**(1–3): p. 203-209.
220. Rella, R., et al., *Poly[3-(butylthio)thiophene] Langmuir–Blodgett films as selective solid state chemiresistors for nitrogen dioxide*. Colloids and Surfaces A: Physicochemical and Engineering Aspects, 2002. **198–200**: p. 829-833.
221. Wang, X., et al., *Thiophene functionalized silicon-containing aggregation-induced emission enhancement materials: applications as fluorescent probes for the detection of nitroaromatic explosives in aqueous-based solutions*. Physical Chemistry Chemical Physics, 2015. **17**(48): p. 32472-32478.
222. Yang, J., et al., *Copper-based coordination polymers from thiophene and furan dicarboxylates with high isosteric heats of hydrogen adsorption*. CrystEngComm, 2014. **16**(23): p. 5121-5127.
223. Ibarra, I.A., et al., *Highly porous and robust scandium-based metal-organic frameworks for hydrogen storage*. Chemical Communications, 2011. **47**(29): p. 8304-8306.
224. Huang, W., et al., *Luminescent and Magnetic Properties of Lanthanide-Thiophene-2,5-dicarboxylate Hybrid Materials*. Crystal Growth & Design, 2009. **9**(3): p. 1361-1369.

225. MacNeill, C.M., et al., *Solvothermal and Reflux Syntheses, Crystal Structure and Properties of Lanthanide-Thiophenedicarboxylate-Based Metal-Organic Frameworks*. Journal of Chemical Crystallography, 2009. **40**(3): p. 222-230.
226. Van, P.C., et al., *Lithiation reaction of 2,5-dibromothiophene. Carbon-13 NMR spectra of 3-substituted derivatives*. Journal of Organic Chemistry, 1984. **49**(26): p. 5250-5253.
227. This is achieved by integrating a variety of reflectance spectra (R). For example, the R of PMMA at 313 nm is 54.3% and appears in the emission spectrum at around 313 nm. Next, the R of the standard and unknown are taken and integrated. The percentages of these R values are calculated against the known R for PMMA.
228. Einkauf, J.D., L. Mathivathanan, and D.T. de Lill, *Structural, spectroscopic, and computational studies of [2,2'-bithiophene]-5-carboxylic acid*. Journal of Molecular Structure, 2016. **1104**: p. 33-39.
229. Shustova, N.B., A.F. Cozzolino, and M. Dincă, *Conformational Locking by Design: Relating Strain Energy with Luminescence and Stability in Rigid Metal–Organic Frameworks*. Journal of the American Chemical Society, 2012. **134**(48): p. 19596-19599.
230. Bagheri, M., M.Y. Masoomi, and A. Morsali, *Highly sensitive and selective ratiometric fluorescent metal–organic framework sensor to nitroaniline in presence of nitroaromatic compounds and VOCs*. Sensors and Actuators B: Chemical, 2017. **243**: p. 353-360.

231. Li, B.-H., et al., *A Luminescent Zinc(II) Metal–Organic Framework for Selective Detection of Nitroaromatics, Fe₃₊ and CrO₄²⁻: A Versatile Threefold Fluorescent Sensor*. *ChemPlusChem*, 2016. **81**(8): p. 885-892.
232. Nagarkar, S.S., et al., *Highly Selective Detection of Nitro Explosives by a Luminescent Metal–Organic Framework*. *Angewandte Chemie International Edition*, 2013. **52**(10): p. 2881-2885.
233. Frisch, M.J., et al., *Gaussian 09*. 2009, Gaussian, Inc.: Wallingford, CT, USA.
234. Ockwig, N.W., et al., *Reticular Chemistry: Occurrence and Taxonomy of Nets and Grammar for the Design of Frameworks*. *Accounts of Chemical Research*, 2005. **38**(3): p. 176-182.
235. He, H., et al., *Reticular Synthesis of a Series of HKUST-like MOFs with Carbon Dioxide Capture and Separation*. *Inorganic Chemistry*, 2016. **55**(17): p. 9071-9076.
236. Li, X.-H., S.-Z. Yang, and H.-P. Xiao, *Synthesis and Crystal Structure of Two Interpenetrated Open Frameworks with Different Structural Motifs*. *Crystal Growth & Design*, 2006. **6**(10): p. 2392-2397.
237. Daiguebonne, C., et al., *Synthesis, Crystal Structure, and Porosity Estimation of Hydrated Erbium Terephthalate Coordination Polymers*. *Inorganic Chemistry*, 2006. **45**(14): p. 5399-5406.
238. Reineke, T.M., et al., *A microporous lanthanide-organic framework*. *Angew. Chem. Int. Ed.*, 1999. **38**(17): p. 2590-2594.

239. Serre, C., et al., *Synthesis and Characterization of a New Three-Dimensional Lanthanide Carboxyphosphate: $Ln_4(H_2O)_7[O_2C-C_5H_{10}N-CH_2-PO_3]_4(H_2O)_5$* . *Inorganic Chemistry*, 2004. **43**(10): p. 3159-3163.
240. Wan, Y., et al., *High-Dimensional Architectures from the Self-Assembly of Lanthanide Ions with Benzenedicarboxylates and 1,10-Phenanthroline*. *Inorganic Chemistry*, 2003. **42**(16): p. 4985-4994.
241. McKinstry, C., et al., *Effect of Synthesis Conditions on Formation Pathways of Metal Organic Framework (MOF-5) Crystals*. *Crystal Growth & Design*, 2013. **13**(12): p. 5481-5486.
242. Biemmi, E., et al., *High-throughput screening of synthesis parameters in the formation of the metal-organic frameworks MOF-5 and HKUST-1*. *Microporous and Mesoporous Materials*, 2009. **117**(1–2): p. 111-117.
243. Burrows, A.D., et al., *Solvent hydrolysis and templating effects in the synthesis of metal-organic frameworks*. *CrystEngComm*, 2005. **7**: p. 548-550.
244. Hermes, S., et al., *Trapping Metal-Organic Framework Nanocrystals: An in-Situ Time-Resolved Light Scattering Study on the Crystal Growth of MOF-5 in Solution*. *Journal of the American Chemical Society*, 2007. **129**(17): p. 5324-5325.
245. Zehnder, R.A., et al., *Network dimensionality and ligand flexibility in lanthanide terephthalate hydrates*. *Journal of Molecular Structure*, 2011. **985**(1): p. 109-119.